UNIVERSITY OF ROCHESTER
LABORATORY FOR LASER ENERGETICS

Volume 167
April–June 2021
DOE/NA/3856-1664

LLE Review

Quarterly Report

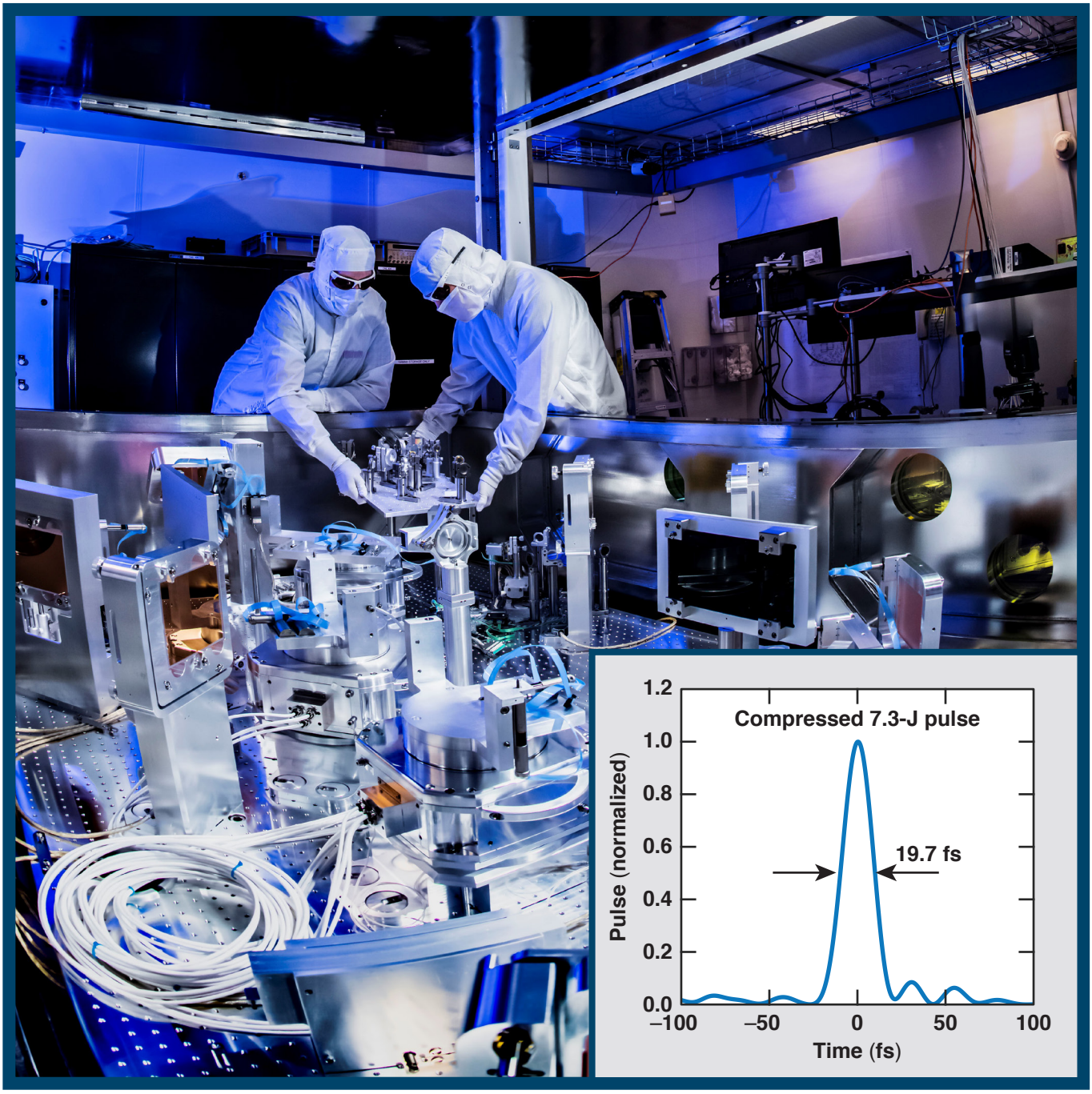

About the Cover:

The cover photo shows M. Spilatro and B. Webb installing a vacuum-compatible SPIDER diagnostic into the MTW-OPAL (Multi-Terawatt optical parametric amplifier line) grating compressor chamber for temporal pulse measurements at full power. MTW-OPAL is a mid-scale femtosecond laser built using optical parametric chirped-pulse amplification; the MTW laser pumps the final parametric amplifier. Just as MTW was a technology development and demonstration platform for the front end of OMEGA EP, MTW-OPAL is intended as a development and proof-of-concept laser for the future EP-OPAL (OMEGA EP-pumped optical parametric amplifier line—a femtosecond-kilojoule laser at LLE's Omega Laser Facility. The inset shows the time-domain reconstruction of the amplified and compressed pulse as measured by the SPIDER diagnostic. First Light Campaign results demonstrated >7-J pulse energies with pulse durations <20 fs.

Large-aperture (>few-cm) noncollinear optical parametric amplifiers (NOPA's) are being developed using deuterated potassium dihydrogen phosphate (DKDP) crystals due to the large bandwidth supported by these crystals and potential for scaling to several tens of centimeters in aperture size. NOPA5, the final amplifier on MTW-OPAL, produces a 45 × 45-mm^2 profile with 11-J pulse energy and >150-nm bandwidth (full width at 10%). The image to the right shows the near-field profile measured after NOPA5, with a peak-to-mean ratio of 1.4:1. The cutout is from a sampling mask used to extract a small portion of the beam for measurement with the SPIDER diagnostic.

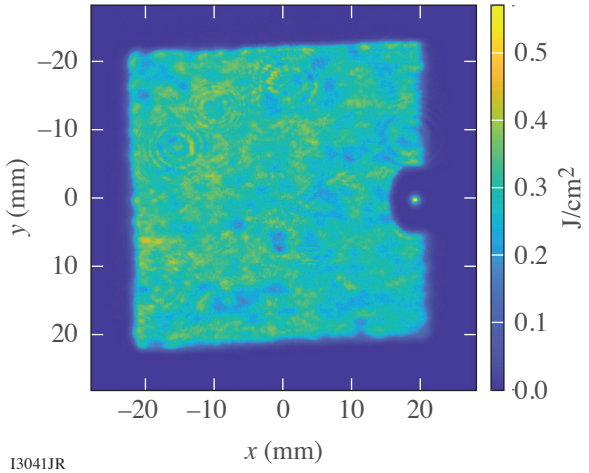

I3041JR

Ultra-broadband transport optics, compressor gratings, and diagnostic tools compatible with EP-OPAL are an active area of development currently being explored using MTW-OPAL. The MTW-OPAL First Light Campaign concluded with a successful demonstration of 0.35-PW peak power. Next steps include developing hardware and techniques for *f*/2 focusing with a deformable mirror and double plasma mirror system to achieve ultrahigh-contrast focused intensities >5 × 10^{21} W/cm^2.

The work described in this volume includes current research at the Laboratory for Laser Energetics, which is supported by New York State Energy Research and Development Authority, the University of Rochester, the U.S. Department of Energy Office of Inertial Confinement Fusion under Cooperative Agreement No. DE-NA0003856, and other agencies.

Printed in the United States of America
Available from
National Technical Information Services
U.S. Department of Commerce
5285 Port Royal Road
Springfield, VA 22161
www.ntis.gov

For questions or comments, contact Erik Power, Editor, Laboratory for Laser Energetics, 250 East River Road, Rochester, NY 14623-1299, (585) 275-0548.

www.lle.rochester.edu

UNIVERSITY OF ROCHESTER
LABORATORY FOR LASER ENERGETICS

Volume 167
April–June 2021
DOE/NA/3856-1664

LLE Review

Quarterly Report

Contents

In Brief

This volume of LLE Review 167 covers the period from April–June 2021. Articles appearing in this volume are the principal summarized results for long-form research articles. Readers seeking a more-detailed account of research activities are invited to seek out the primary materials appearing in print, detailed in the publications and presentations section at the end of this volume.

Highlights of research presented in this volume include:

- T. J. B. Collins *et al*. use 2-D radiation-hydrodynamic modeling of two cryogenic implosions on the OMEGA Laser System to infer the degree of fuel–shell mixing near stagnation (p. 123).
- P. T. Campbell *et al*. use data from two OMEGA EP campaigns to validate extended-magnetohydrodynamic models that include both nonlocal suppression of Biermann battery field generation and radiation transport (p. 127).
- P. V. Heuer *et al*. adapt the magnetized liner inertial fusion platform on OMEGA to observe suppression of self-generated magnetic fields in a cylindrical implosion geometry (p. 131).
- A. Colaïtis *et al*. compare the new fluid-scale laser model *IFRIIT* to direct-drive implosion experiments on OMEGA, showing excellent agreement with neutron data in the presence of various sources of 3-D effects (cross-beam energy transfer, beam imbalance, target misalignment, etc.) (p. 134).
- A. Lees *et al*. experimentally infer scaling laws for fusion yields on OMEGA by examining 177 shots and find that optimal yield is obtained for shots with adiabat >4.5 and low in-flight aspect ratio (p. 137).
- A. Shvydky *et al*. examine shock release in radiation-hydrodynamic models and compare to laser-driven CH shells on OMEGA EP (p. 141). Modeling shows the shock released from the back surface of the foil is strongly dependent on conditions immediately preceding shock breakout.
- A. Tentori *et al*. use a planar target experiment on OMEGA EP to characterize the hot-electron source and shock dynamics relevant to the shock-ignition inertial confinement fusion scheme, and find that the presence of hot electrons increases shock pressure by 25 Mbar up to a peak of 150 Mbar (p. 144).
- A. M. Saunders *et al*. create intersecting laser-driven tin microjets on OMEGA EP and observe no interaction for jets driven by 11.7-GPa shock pressures, while jets driven by 116-GPa shock pressures show collisions between jet particles resulting in velocity reduction, angular spread, and cloud formation (p. 147).
- P. Franke *et al*. propose a scheme to use laser pulses with shaped space–time and transverse intensity profiles (flying focus) to drive optical shocks for self-photon acceleration while avoiding group velocity walkoff and dispersion, resulting in dramatic self-steepening and spectral broadening into a multi-octave spectrum supporting pulses with duration <400 as (p. 150).
- D. Ramsey *et al*. describe nonlinear Thomson scattering with ponderomotive control—an adaptation of flying focus that shapes a single laser pulse to have a backward-propagating intensity peak at focus, driving electron acceleration counter to the phase velocity of the incoming laser pulse (p. 153).
- Y. Zhang *et al*. simulate kinetics of a magnetized collisionless shock formation using realizable parameters from the magneto-inertial fusion electrical discharge system (MIFEDS) on OMEGA EP and show shocks are collisionless and formed by a modified two-stream instability (p. 155).

- H. G. Rinderknecht *et al.* derive analytical scaling laws for the radiative properties of magnetic filaments, compare with 3-D particle-in-cell simulations, and describe initial experiments using the Texas Petawatt Laser System. Magnetic filaments are observed on two of eight laser shots, in line with the statistical likelihood of observation (p. 159).
- D. N. Polsin performs simultaneous x-ray diffraction and reflectivity measurements on ramp-compressed sodium using the OMEGA EP laser and observes the *hP4* phase at 480 GPa and ~3000 K, implying electride formation is possible on nanosecond time scales and at higher temperatures (p. 162).
- V. V. Karasiev *et al.* report on large-scale *ab initio* molecular-dynamics simulations elucidating the subcritical character of the insulator–metal transition in warm dense liquid hydrogen (p. 166).
- S. F. Nwabunwanne and W. R. Donaldson report on a new generation of fast UV photodiodes using $Al_xGa_{1-x}N$ substrates. Measurements show a bias-voltage–independent external quantum efficiency of 1198% at 19.5 V and mobility suitable for 1.31-ps response time (p. 170).
- J. Zhang, W. R. Donaldson, and G. P. Agrawal develop a frequency-domain transfer-matrix approach to solving temporal reflection and refraction at a temporal boundary with finite rise time and find that total internal reflection can occur even for shallow boundaries (p. 173).
- J. Zhang, W. R. Donaldson, and G. P. Agrawal calculate that a temporal analog of a Fabry–Perot resonator can be formed using two moving temporal boundaries inside a dispersive medium (p. 175).
- J. Bromage *et al.* report first light on the MTW-OPAL (Multi-Terawatt optical parametric amplifier line) Laser System, demonstrating 7.3-J, 19.7-fs pulses with 30%±1.4% pump-to-signal efficiency in the final amplifier (p. 177).
- G. W. Jenkins, C. Feng, and J. Bromage derive an analytical model for angular alignment tolerance in divided-pulse nonlinear compression and match with experiment (p. 180).
- S. Rai *et al.* perform a length-scale analysis on oceanographic satellite data and find that wind kills mesoscale eddies at an average rate of 50 GW (p. 182).
- J. Frenje *et al.* report on the 12th Omega Laser Facility Users Group Workshop, held virtually from 27–30 April 2021 (p. 184).
- J. Puth *et al.* summarize operations of the Omega Laser Facility during the third quarter of FY21 (p. 187).

Erik Power
Editor

Direct Evidence of Fuel–Ablator Mix from Monochromatic Time-Gated Radiography in OMEGA Cryogenic Implosions

T. J. B. Collins, C. Stoeckl, R. Epstein, W. A. Bittle, C. J. Forrest, V. Yu. Glebov, V. N. Goncharov, D. R. Harding, S. X. Hu, D. W. Jacobs-Perkins, T. Z. Kosc, J. A. Marozas, C. Mileham, F. J. Marshall, S. F. B. Morse, P. B. Radha, S. P. Regan, B. Rice, T. C. Sangster, M. J. Shoup III, W. T. Shmayda, C. Sorce, W. Theobald, and M. D. Wittman

Laboratory for Laser Energetics, University of Rochester

In direct-drive inertial confinement fusion,[1] a shell is imploded via direct laser-light illumination. The shell is composed of an inner layer of fuel (typically equimolar deuterium and tritium, which maximizes yield) and a thinner outer "ablator" layer of non-fuel material (e.g., a CH polymer). The implosion of a two-layer shell filled with gaseous fuel is used to briefly assemble a "hot spot" of sufficiently high temperature (4 or more keV) and density for D–T fusion reactions to occur. The fusion neutron yield depends on the hot-spot conditions and the confinement time, the latter depending on the areal density of the shell and ablator at stagnation. Various phenomena can reduce the shell areal density, such as heating of the shell by suprathermal electrons generated in the corona surrounding the imploding target; shock dynamics, which must be carefully engineered due to the increase in entropy generated by mistimed shocks; absorption of coronal radiation by the shell, which places an additional constraint on the choice of ablator material; and mixing of the ablator and shell fuel material due to hydrodynamic instabilities, particularly the Rayleigh–Taylor instability (RTI).

In this summary we infer the degree of fuel–shell mixing using 2-D radiation-hydrodynamic modeling of two OMEGA cryogenic implosions. The properties of the two implosions in question are shown in Table I (with 1-D simulated data calculated using the radiation hydrocode *LILAC*[2]). Direct evidence that this is due to Rayleigh–Taylor fuel–ablator mixing in these two implosions was previously obtained using a Si He_α backlighter driven by an ~20-ps short pulse generated by OMEGA EP.[3] The shadow cast by the shell shortly before stagnation, as diagnosed using backlit radiographs, shows a softening near the limb, which is evidence of an ablator–fuel mix region for a low-adiabat implosion ($\alpha \sim 1.9$, in-flight aspect ratio IFAR = 14) but not for a moderate adiabat implosion ($\alpha \sim 2.5$, IFAR = 10). We consider various possible causes of fuel–shell mix, using the radiation-hydrodynamic code *DRACO*, and find good agreement between experimental and simulated radiographs when imprint is modeled and for a particular ablator thickness that lies within the range of possible thicknesses as determined by pre-shot target metrology. Modeling with *DRACO*[4] includes multigroup radiative transport, nonlocal electron heat transport, scattering due to cross-beam energy transfer,[5] and first-principles[6] equation of state and opacity models, and is post-processed with *Spect3D*[7] to generate synthetic x-ray images for direct comparison

Table I: Simulated and experimental properties of the moderate- and low-adiabat shots 81590 and 82717, respectively. The ratio of the pressure to the Fermi pressure at zero temperature is given by α; IFAR is the in-flight aspect ratio, the ratio of the initial shell radius to the thickness at a convergence of 1.5; T_i is the neutron-weighted ion temperature; ρR is the neutron-weighted areal density of the shell; ρR/clean is the ratio of measured to 1-D simulated areal density; and YOC is the ratio of experimental to 1-D yield.

LILAC (1-D)							Experiment		
Shot	α	IFAR	v_{imp} (km/s)	ρR (mg/cm^2)	$T_{i,LILAC}$ (keV)	Y_{LILAC} (10^{13})	ρR/clean	$T_{i,exp}$ (keV)	YOC
81590	2.5	10	240	250	2.2	1.4	78%	2.7	19%
82717	1.9	14	280	246	2.4	2.6	41%	2.4	8%

with experimental framing-camera images. Furthermore, because lineouts from synthetic radiographs of 1-D and 2-D simulations show good agreement for the moderate adiabat shot 81590 (see Fig. 1), we focus below on the lower-adiabat shot 82717. In the possible sources of mix described below, we begin with those found to be the less significant, concluding with the most significant, imprint.

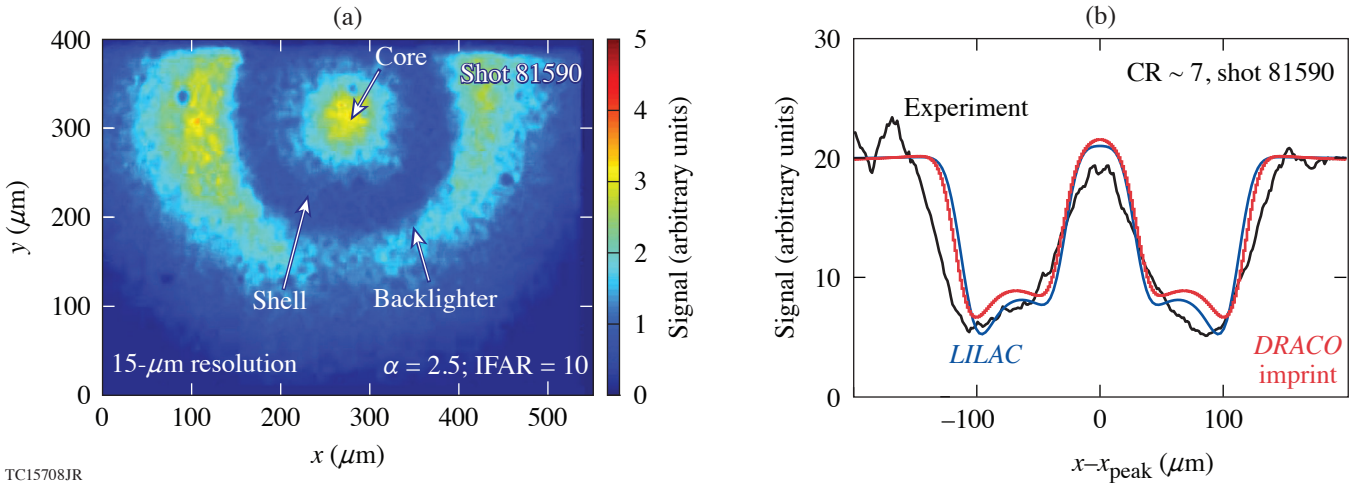

Figure 1
The (a) experimental radiograph for shot 81590 and (b) radiographic lineouts for the experiment (black curve), *LILAC* (blue curve), and *DRACO* (red curve), plotted as functions of the horizontal coordinate measured relative to the position of the peak core emission (x_{peak}). CR: convergence ratio.

Long-Wavelength Modes

The imploding shell is unstable to Rayleigh–Taylor and Richtmyer–Meshkov instabilities, which can be seeded by target and laser nonuniformities and imperfections. We modeled the effects of long-wavelength laser drive nonuniformities, including beam-to-beam power imbalance, and beam pointing error. Long-wavelength mode growth can also be seeded by nonuniformity in the inner edge of the DT ice, the greatest amplitudes of which occur for Legendre modes with modal index less than 10. The impact of these was found to be negligible in the fuel–ablator mix used for both shots, although perturbations with Legendre-mode indices 1 and 2 have a visible effect on the shape of the core emission and may be responsible for the slight elongation of the hot spot [Fig. 2(a)].

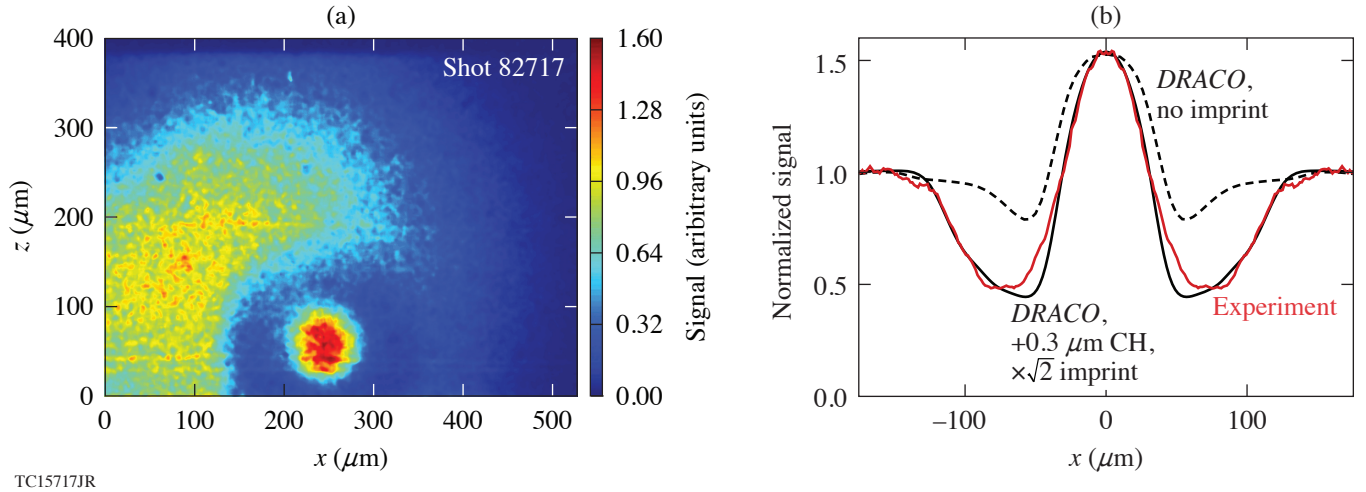

Figure 2
(a) The experimental radiograph for shot 82717 shows a hot central core (red) surrounded by a dark ring of shell absorption, further surrounded by the off-center backlighter emission. (b) Radiographic lineouts of shot 82717 for the experiment (red curve), symmetrized about $x = 0$, where x is the horizontal position in the image plane; a simulation without imprint (dashed black curve); and a *DRACO* simulation with imprint and an additional 0.3 μm of initial ablator thickness.

Kinetic Effects and Concentration Diffusion

Another mechanism investigated as a means of transporting carbon deep into the imploding shell is concentration diffusion. One of many kinetic effects that have received attention in recent years,[8] concentration diffusion is expected to occur wherever a concentration gradient exists in a multispecies plasma.[9] The flux in this case is given by Fick's law and is proportional to the concentration gradient. A second-order accurate ion concentration diffusion model was implemented in *DRACO* to investigate this effect. At the fuel–shell interface the concentration gradient scale length is small, being comparable to the mean-free path for the cold shell material. Due to the low temperatures and high densities, the concentration flux remains small throughout the implosion, increasing only upon complete ablation of the CH ablator, which occurs late in time. Once the CH is ablated, the temperature quickly rises and the density drops, causing the diffusion coefficient to rise; however, the region where the concentration gradient is large has also ablated. Therefore, concentration diffusion is able to flux material within the corona but not within the shell.

Classical Instability Growth at the Fuel–Ablator Interface

One natural source of mix to consider is perturbation growth at the fuel–ablator interface seeded by perturbations on that surface. Unlike at the ablation surface, growth of modes here due to the RTI is not diminished by ablation, so no high-mode ablative cutoff exists. Beta decay from tritium decay in permeation-filled–target cases causes localized damage at the inner shell surface, potentially seeding the perturbation growth. This may play a role in the known relationship between target age and performance.[10] In addition, the surface roughness of the polystyrene ablator shell may seed perturbation growth. A simulation of shot 82717 was performed with a piecewise power-law function approximating the measured polystyrene power spectrum and was repeated with the spectrum multiplied by various multiples. For the nominal case, the effects of the perturbation are small and have a negligible impact on the shell mass density. For the enhanced simulation, the impact is more significant on the shell mass density, but there is still minimal material mixing due to perturbation growth.

Laser Imprint

For the lower-adiabat shot, 82717, the radiograph lineout from a 1-D simulation fails to match either the radial extent (width) or depth of the shadow cast by the shell. *DRACO* simulations were performed with the expected level of laser imprint, as well as for enhanced levels in which the imprint spectrum was multiplied by factors of $\sqrt{2}$ and 2. These simulations were able to reproduce the depth of the shell shadow but not the width, the closest agreement in the shell depth being found for the $\sqrt{2}$ simulation. Because 3-D perturbations are known to grow more quickly than 2-D perturbations, the need for an enhanced imprint spectrum in a 2-D simulation is expected.[11]

The discrepancy in the depth of the shell shadow has a ready explanation in the markedly greater bound–free absorption of the CH compared to the free–free absorption of the DT fuel. A survey of simulations with the same shell mass but different initial ablator thickness shows that an ablator thickness of 0.3 μm has a marked impact on the thickness of the shell shadow. A radiographic lineout from a simulation using an ablator thickness of 11.5 μm and incorporating enhanced imprint shows a close agreement with the experimental data (Fig. 2). It should be noted that the impact of ablator thickness on the shadow width and imprint on the shadow depth are independent; increasing the degree of imprint fails to increase the thickness of the shadow, and increasing the ablator thickness alone cannot reproduce the depth of the shadow without making it far too wide. The important result of this study is that the experimental radiograph is only reproduced by enhanced imprint (not unexpected) combined with an ablator that lies within the measured range of 10.9 μm to 11.5 μm but lies at the upper limit of the range of uncertainty of the measurement. The latter observation allows two possible inferences: (a) The actual ablator thickness was within the measurement error, or (b) the ablator thickness was actually smaller but the simulated ablation rate exceeded the experimental rate, a possibility suggested by previous warm-target implosions.[12] This suggests value in developing and investing in higher-precision target metrology.

In conclusion, two OMEGA cryogenic implosions were backlit by OMEGA EP, obtaining radiographs of the hot-spot and stagnation fuel–shell assembly close to peak convergence. The implosions were designed to lie on either side of the stability threshold, and both simulations and experimental data bear this out. Modeling of the moderate-adiabat implosion agrees well with experiment, as expected. Modeling of the low-adiabat implosion agrees when an enhanced level of imprint is modeled, and only when a sufficiently thick ablator (within measurement error) is assumed.

This material is based upon work supported by the Department of Energy National Nuclear Security Administration under Award Number DE-NA0003856, the University of Rochester, and the New York State Energy Research and Development Authority.

1. R. S. Craxton *et al.*, Phys. Plasmas **22**, 110501 (2015).
2. J. Delettrez *et al.*, Phys. Rev. A **36**, 3926 (1987).
3. R. Epstein *et al.*, High Energy Density Phys. **23**, 167 (2017); C. Stoeckl *et al.*, Phys. Plasmas **24**, 056304 (2017).
4. P. B. Radha *et al.*, Phys. Plasmas **23**, 056305 (2016); I. V. Igumenshchev *et al.*, Phys. Plasmas **17**, 122708 (2010).
5. C. J. Randall, J. J. Thomson, and K. G. Estabrook, Phys. Rev. Lett. **43**, 924 (1979).
6. J. J. MacFarlane *et al.*, High Energy Density Phys. **3**, 181 (2007).
7. S. X. Hu *et al.*, Phys. Rev. B **84**, 224109 (2011); S. X. Hu *et al.*, Phys. Rev. E **92**, 043104 (2015); S. X. Hu *et al.*, Phys. Rev. E **90**, 033111 (2014); S. X. Hu *et al.*, Phys. Plasmas **25**, 056306 (2018).
8. P. Amendt *et al.*, Phys. Plasmas **18**, 056308 (2011).
9. R. B. Bird, W. E. Stewart, and E. N. Lightfoot, *Transport Phenomena*, Revised 2nd ed. (John Wiley & Sons, Inc., New York, 2007).
10. E. M. Campbell *et al.*, Phil. Trans. R. Soc. A **379**, 20200011 (2020); A. Lees *et al.*, Phys. Rev. Lett. **127**, 105001 (2021).
11. M. M. Marinak *et al.*, Phys. Rev. Lett. **80**, 4426 (1998); R. Yan *et al.*, Phys. Plasmas **23**, 022701 (2016).
12. D. T. Michel *et al.*, High Power Laser Sci. Eng. **3**, e19 (2015).

Measuring Magnetic-Flux Suppression in High-Power Laser–Plasma Interactions

P. T. Campbell,[1] C. A. Walsh,[2] B. K. Russell,[1] J. P. Chittenden,[3] A. Crilly,[3] G. Fiksel,[1] L. Gao,[4] I. V. Igumenshchev,[5] P. M. Nilson,[5] A. G. R. Thomas,[1] K. Krushelnick,[1] and L. Willingale[1]

[1]Gérard Mourou Center for Ultrafast Optical Science, University of Michigan
[2]Lawrence Livermore National Laboratory
[3]Blackett Laboratory, Imperial College, London
[4]Princeton Plasma Physics Laboratory
[5]Laboratory for Laser Energetics, University of Rochester

In high-power-laser–produced plasmas, strong magnetic fields can be spontaneously generated by a number of mechanisms, although the primary source is the Biermann battery effect caused by nonparallel temperature and density gradients $\left(\partial B/\partial t \propto \nabla T_e \times \nabla n_e\right)$. A detailed understanding of self-generated magnetic fields is critical to laser-fusion research because strong fields can influence thermal energy transport and potentially impact the evolution of hydrodynamic instabilities. Laser-driven magnetic fields also enable laboratory investigations of magnetized astrophysical phenomena, especially magnetic reconnection.

The extended-magnetohydrodynamics (extended-MHD) framework has been developed to describe transport of energy and magnetic fields in high-energy-density (HED) plasmas.[1] Predictive modeling used in concert with experimental observations is often essential for developing and interpreting both laser-fusion and laboratory astrophysics experiments. Although relatively simple in the broader context of HED experiments, a single laser spot interacting with a foil target can provide a powerful platform for validating extended-MHD modeling.

Using proton deflectometry to make high spatial and temporal resolution measurements of magnetic-field generation driven by moderate laser intensities ($I_L = 10^{14}$ to 10^{15} W/cm^2), recent experiments demonstrated that simulations of laser–foil interactions must incorporate key physical processes such as Biermann battery field generation and Nernst advection.[2,3] By varying the target material the influence of atomic or radiation physics on transport and field dynamics can be explored. Incorporating radiation transport into extended-MHD simulations reproduced recent experimental observations of two distinct regions of magnetic-field generation around radiation-driven double ablation fronts in mid-Z targets.[4]

In that work, however, it was found that extended-MHD simulations overestimated the generated magnetic flux. It is anticipated that nonlocal effects not captured by the extended-MHD framework can suppress the rate of Biermann battery field generation in regions where the electron mean free path (λ_{ei}) approaches (or exceeds) the local temperature-gradient length scale $\left(l_T = \left|T_e/\nabla T_e\right|\right)$. Using empirical fits to kinetic simulations, Sherlock and Bissell[5] developed a scaling for the suppression of classical Biermann battery generation rates as a function of the ratio λ_{ei}/l_T.

In this summary, experimental observations of magnetic flux are used to help validate extended-MHD simulations that include the new scaling for nonlocal suppression of Biermann battery field generation, as well as radiation transport. Experimental data are drawn from two campaigns performed with the OMEGA EP laser. Magnetic-field generation was driven by either one[4] ($I_L = 2.2 \times 10^{14}$ W/cm^2) or two overlapped[3] ($I_L = 4.4 \times 10^{14}$ W/cm^2) UV laser pulses interacting with thin foil targets. The foil material was varied between 50-μm-thick plastic (CH), 25-μm copper, 25-μm aluminum, or 50-μm aluminum coated with either 1 μm of copper (Cu + Al) or gold (Au + Al). Self-generated magnetic fields were imaged by protons in a point-projection geometry.

In both experiments a high-intensity laser pulse was used to produce a proton probe via the target normal sheath acceleration mechanism. A 1-D polar-coordinates field reconstruction technique was developed to extract quantitative path-integrated magnetic-field information from radial lineouts through the proton images.[4,6]

Experimental measurements were compared to extended-MHD simulations performed using the Gorgon code,[1] which was updated with the option to include the new scaling for suppression of magnetic-field generation due to kinetic effects (referred to throughout as "Biermann suppression"). The results for CH foil targets are summarized in Fig. 1. Proton images show the evolution of magnetic-field structures using the higher laser intensity ($2I_0$, overlapped pulses) in Fig. 1(a). Corresponding reconstructed magnetic-field profiles are plotted in Fig. 1(b). Figure 1(c) compares the evolution of the azimuthal magnetic flux from the experiment and extended-MHD simulations for both laser intensities. Simulations without Biermann suppression greatly overestimate the magnetic flux (>5×). Agreement is significantly improved by including Biermann suppression, indicating that this effect is likely influencing the field dynamics. In the simulations, the suppression results in a 3× to 4× reduction in the predicted magnetic flux.

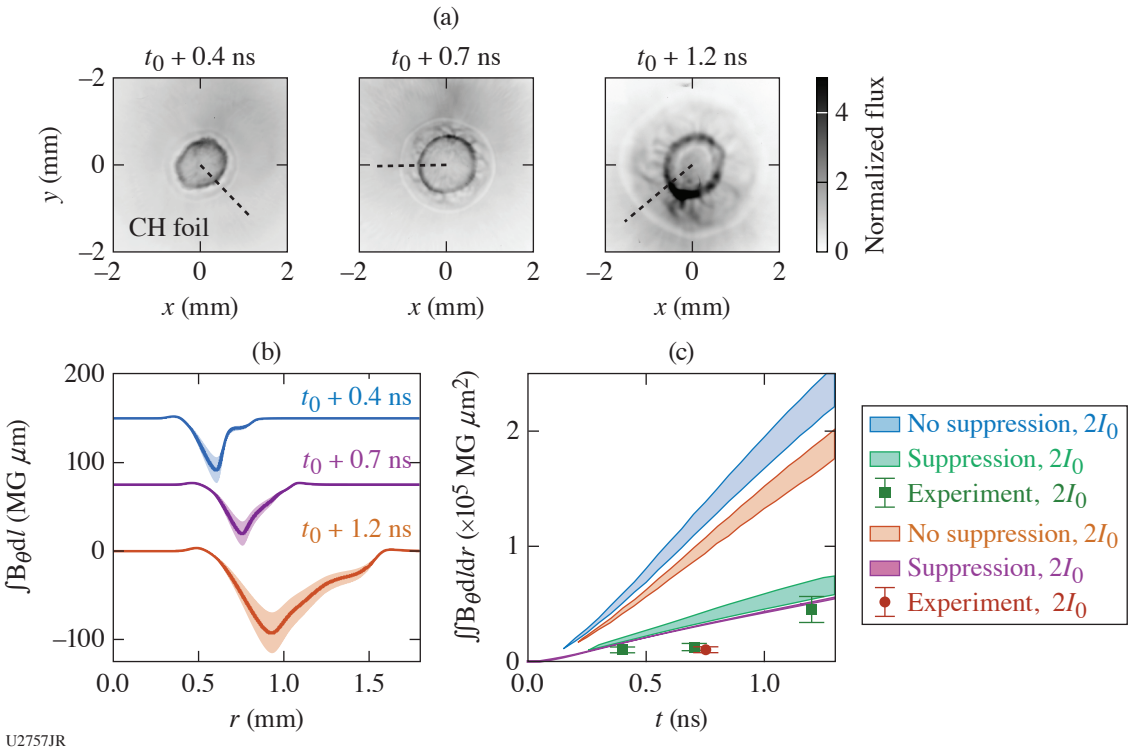

Figure 1
Comparison of experimental and simulation results for CH foils. (a) Proton images of fields driven by the higher, overlapped laser intensity ($2I_0$) taken at 0.4 ns, 0.7 ns, and 1.2 ns. Radial lineout locations are indicated by dashed lines. (b) Reconstructed magnetic-field profiles (offset vertically for clarity). (c) Magnetic-flux predictions from simulations both without and with Biermann suppression for each laser intensity are compared to experimental measurements. Upper and lower bounds on the simulation results are produced by tuning the laser energy to approximate the influence of energy-coupling efficiency (corresponding to ~90% and ~70% coupling, respectively).

Figure 2 summarizes the results for Cu foil targets with the lower laser intensity. As with CH targets, the simulations without suppression overestimate the flux, although the discrepancy is not as large. For Cu targets, however, the Biermann suppression model reduces the predicted flux below experimental observations. Overall, the simulation and experimental results suggest that nonlocal suppression effects are more significant for low-Z targets. Without Biermann suppression, simulations with Cu targets predict lower magnetic flux than the CH results, likely due to additional radiative losses at higher Z, reducing temperature gradients. In contrast, the experimental measurement of the magnetic flux increases when the target changes from CH to Cu. The same

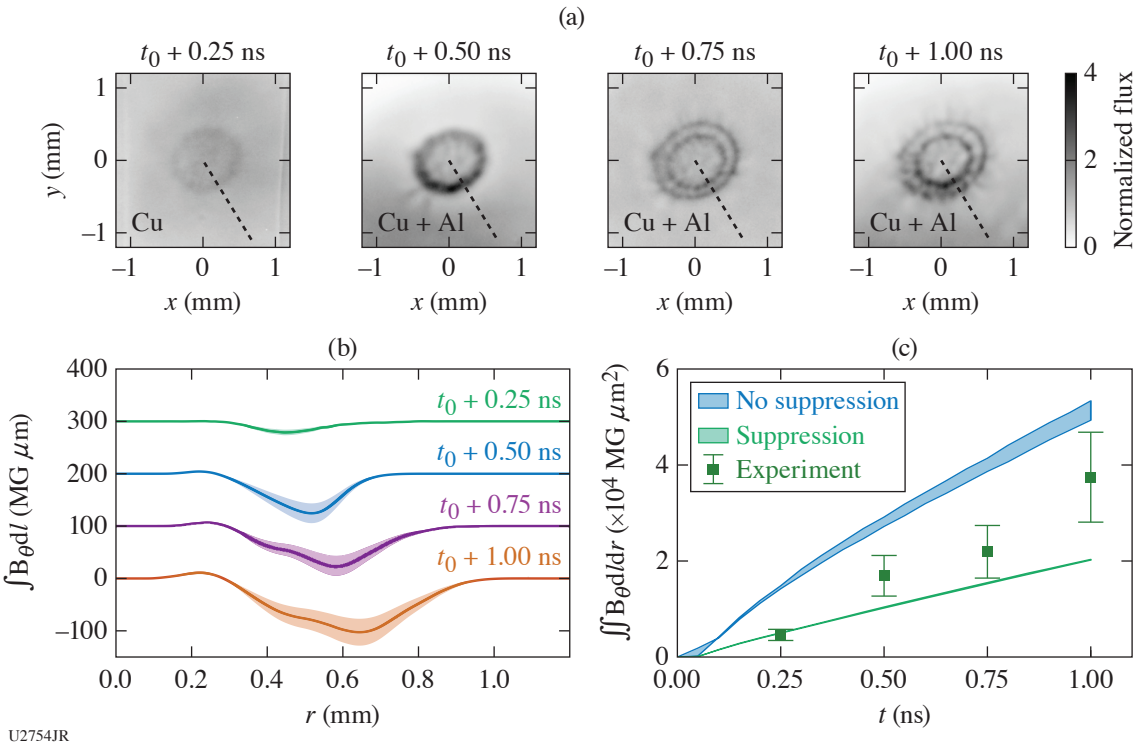

Figure 2
Comparison of experimental and simulation results for Cu foils. (a) Proton images at 0.25 ns, 0.5 ns, 0.75 ns, and 1.0 ns. Lineout locations are indicated by dashed lines. The target for t_0 + 0.25 ns was a 25-μm-thick Cu foil, and the other probing times use a Cu + Al layered target. (b) Reconstructed magnetic-field profiles. (c) Magnetic-flux predictions from simulations both without and with Biermann suppression are compared.

qualitative trend is also seen in the simulations including Biermann suppression, where the copper targets are less kinetic, due to both lower temperature gradients from radiative losses and shorter mean free paths for higher-Z plasmas.

In conclusion, quantitative measurements of magnetic flux enable detailed comparisons between experiments and extended-MHD simulations, demonstrating the need to account for suppression of Biermann battery generation due to nonlocal effects. Even with the Biermann suppression, the simulations with CH targets overestimate magnetic-flux generation. For Cu, however, while some suppression is necessary, the implementation of the suppression scaling decreases the predicted flux below experimental observations. The effects of radiation-hydrodynamics and the equation of state likely influence the details of simulations but are beyond the scope of this work. In future experiments, additional diagnostics, such as Thomson scattering and interferometry, can help constrain plasma parameters to further validate and improve extended-MHD models. Combined with the magnetic-field analysis presented in this work, measurements of the temperature and density profiles can elucidate the dynamic interplay between energy transport and field generation in HED plasmas.

This material is based upon work supported by the Department of Energy, National Nuclear Security Administration under Award Numbers DE-NA0003606, DE-NA0003764, and DE-AC52-07NA27344. P. T. Campbell is supported by the U.S. Department of Energy Fusion Energy Sciences Postdoctoral Research Program administered by the Oak Ridge Institute for Science and Education (ORISE) for DOE. ORISE is managed by Oak Ridge Associated Universities (ORAU) under DOE contract number DE-SC0014664. B. K. Russell acknowledges support from National Science Foundation Award Number 1751462.

1. C. A. Walsh *et al.*, Phys. Plasmas **27**, 022103 (2020).
2. L. Willingale *et al.*, Phys. Rev. Lett. **105**, 095001 (2010).

3. L. Gao *et al.*, Phys. Rev. Lett. **109**, 115001 (2012).
4. P. T. Campbell *et al.*, Phys. Rev. Lett. **125**, 145001 (2020).
5. M. Sherlock and J. J. Bissell, Phys. Rev. Lett. **124**, 055001 (2020).
6. P. T. Campbell *et al.*, "Measuring Magnetic Flux Suppression in High-Power Laser-Plasma Interactions," Physics Archive, https://arxiv.org/abs/2107.12864 (2021).

Observed Suppression of Self-Generated Magnetic Fields in a Laser-Driven Cylindrical Implosion

P. V. Heuer,[1] L. S. Leal,[1] J. R. Davies,[1] E. C. Hansen,[1] D. H. Barnak,[1] J. L. Peebles,[1] and A. Birkel[2]

[1]Laboratory for Laser Energetics, University of Rochester
[2]Plasma Science and Fusion Center, Massachusetts Institute of Technology

The spontaneous generation of magnetic fields in plasmas is responsible for the creation of astrophysical magnetic fields from the primordial universe to stellar environments. Self-generated magnetic fields are also key features of many laboratory experiments on subjects ranging from laboratory astrophysics to inertial confinement fusion. Once generated, these fields can substantially alter particle and energy transport in the plasma, fundamentally modifying the plasma dynamics. Accurate computational modeling of magnetic-field self-generation is therefore crucial to correctly simulating these systems.

Many systems of interest require large simulation volumes and/or resolutions that are only computationally tractable using magnetohydrodynamics (MHD). However, recent theoretical articles[1,2] comparing MHD and Vlasov–Fokker–Planck (VFP) kinetic simulations have predicted that kinetic (nonlocal) effects neglected in MHD could lead to a substantial overestimate of self-generated magnetic fields in MHD simulations. This discrepancy could result in substantial errors in MHD simulations that include regions of low collisionality (where kinetic effects are non-negligible). This is particularly (but not exclusively) significant for laboratory experiments with laser-produced plasmas, which self-generate magnetic fields within the relatively low-density ablated plasma.

Results from a cylindrical implosion experiment on the OMEGA Laser System recently provided the first experimental evidence directly demonstrating the suppression of self-generated magnetic fields relative to MHD simulations in an inertial confinement fusion experiment. This measurement is made using oblique proton radiography, which allows axially resolved measurements of self-generated azimuthal magnetic fields that are undetectable at normal incidence. Comparisons to synthetic radiographs generated using simulated fields show that the observed field is a factor of ~0.4× smaller than predicted by MHD. Simulation results also indicate that nonlocal effects are likely responsible for this discrepancy.

The experiment utilizes a platform[3] initially developed for studying laser-driven magnetized liner inertial fusion (MagLIF)[4] on the OMEGA Laser System. The target is a gas-filled (11 atm D_2) parylene-N cylinder (CH, 20 μm thick, outer diameter of 580 μm) imploded using 40 beams (1.5-ns square pulse length, 16-kJ total energy) with an overlapped intensity of 10^{14} W/cm^2. Prior to compression, an axial beam (180 J) blows down a thin window on the end of the cylinder and preheats the D_2 gas. A set of external coils driven by MIFEDS (magneto-inertial fusion electrical discharge system)[5] provides an axial magnetic field (B_z = 9 T) for one shot but is inactive for a second unmagnetized shot. Proton radiography[6] is used to diagnose the self-generated magnetic fields.

The multiphysics radiation-hydrodynamics code *HYDRA*[7] is used to perform two 3-D simulations of the unmagnetized experiment with different flux limiters (f = 0.15 and f = 0.05) and one simulation of the magnetized experiment (f = 0.15). Varying the flux limiter tests the extent to which it affects the Biermann battery mechanism by modifying the electron temperature gradients.[2] The unmagnetized simulation results (Fig. 1) show a coronal plasma expanding away from the axis as the cylinder implodes. Steep density and temperature gradients are present within the ablated plasma and the cylinder. The dominant electromagnetic field components are a radial electric field $E_r \sim 10^7$ V/m and an azimuthal magnetic field $B_\varphi \sim 50$ T. The orientation of this mag-

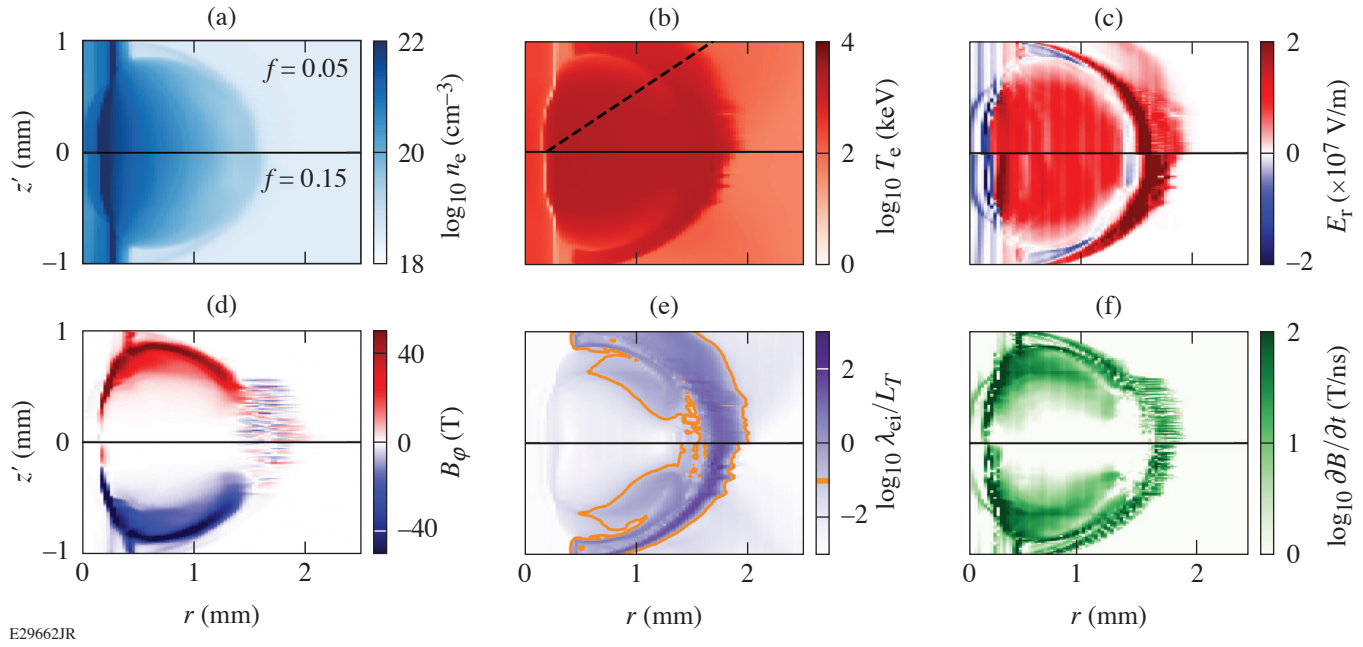

Figure 1
HYDRA outputs of the (a) electron density, (b) electron temperature, (c) radial electric field, (d) azimuthal magnetic field, (e) nonlocality parameter λ_{ei}/L_T, and (f) MHD Biermann battery source term at $t = 0.9$ ns. The top and bottom halves of each plot show the $f = 0.05$ and $f = 0.15$ unmagnetized simulations, respectively. An orange contour in (e) marks the region $\lambda_{ei}/L_T > 0.1$, where nonlocal effects are expected to be significant.

netic field is consistent with it being generated by the Biermann battery mechanism due to nonparallel temperature and pressure gradients in the coronal plasma. The magnetized simulation is comparable, but it also includes a compressed axial magnetic field at the center of the cylinder. The self-generated magnetic field is found to be insensitive to the choice of flux limiter.

To determine the possible impact of nonlocal effect on thermal transport, the nonlocality parameter λ_{ei}/L_T is calculated from the *HYDRA* results, where $L_T = T_e/\nabla T_e$ is the gradient length scale of the electron temperature T_e and λ_{ei} is the electron ion mean free path; and $16\pi\varepsilon_0^2 T_e^2/Zn_e e^4 \log\Lambda$, and where ε_0 is the permittivity of free space, n_e is the electron density, and e is the fundamental charge. The mean ion charge is $Z = 4$ and the Coulomb logarithm is $\log\Lambda = 8$. Significant nonlocal effects are expected when $\lambda_{ei}/L_T > 0.1$ (Ref. 8). The MHD Biermann battery source term, $\partial B/\partial t = \nabla T_e \times \nabla n_e/en_e$ is also calculated. Comparing these quantities [Figs. 1(e) and 1(f)] shows that substantial Biermann growth is predicted within the region of the ablated plasma where nonlocal effects are expected to be significant.

The primary feature observed in the experimental proton radiographs is a bell-shaped region of depleted proton flux [Fig. 2(a)], from which 15-MeV protons have been deflected in z by at least 0.1 rad (since a corresponding peak is not visible on the radiograph). This deflection is in the nonlinear regime,[6,9] so a linear inversion to recover the integrated field is not possible. However, as an order-of-magnitude estimate and assuming a length scale of ~1 mm, an electric field of $E \sim 10^9$ V/m or magnetic field of $B \sim 50$ T is required to reproduce the observed deflection. Comparing these values to those predicted by the MHD simulation ($E_r \sim 10^7$ V/m, $B_\varphi \sim 50$ T) indicates that the azimuthal magnetic field must be responsible.

To directly compare *HYDRA* simulations to experimental results, synthetic proton radiographs are generated using an open-source particle-tracing algorithm that was developed for the PlasmaPy project as part of this work.[10] Direct comparisons show that the synthetic radiographs reproduce the bell feature observed in the experimental radiographs [Fig. (2a)]. To make a quantitative comparison, a horizontal lineout is taken through the center of the bell region [averaging in z over the shaded region in Fig. 2(a)]. The normalized intensity lineout comparisons in Fig. 2(b) show that the bell-shaped depression in the synthetic radiographs is

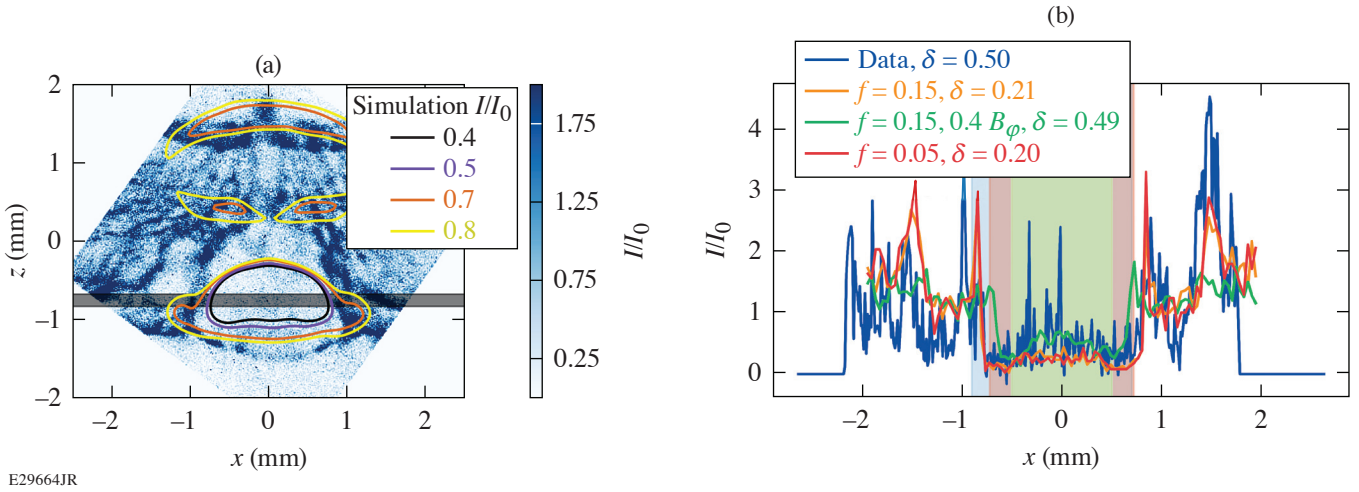

Figure 2
(a) A synthetic radiograph created using the fields from the unmagnetized $f = 0.15$ simulation (contours) qualitatively reproduces the bell-shaped depression observed in the 15-MeV proton radiograph from the unmagnetized experiment (image). (b) Lineouts through the gray-shaded region in (a), normalized to their mean. The $f = 0.05$ and $f = 0.15$ simulations are identical, but both overpredict the measured depletion [δ = mean (I/I_0) averaged over the shaded region in (b)] by a factor of ~2. Reducing the simulated B_φ by a factor of ~0.4 reproduces the depletion of the experimental radiograph.

twice as deep as measured in the unmagnetized experiment. This result implies that the azimuthal magnetic field measured in the experiments is significantly weaker than predicted by the MHD simulation. Similar comparisons with different flux limiters as well as the magnetized shot support the same conclusion.

We hypothesize that this discrepancy is the direct effect of a non-Maxwellian distribution on the Biermann battery source term. The measured reduction in the self-generated magnetic field is consistent with previously published work comparing Biermann battery growth in MHD and VFP simulations.[1] This measurement constitutes experimental evidence for the previous theoretical prediction that nonlocal effects result in the overprediction of self-generated fields in MHD simulations.

This material is based upon work supported by the Department of Energy, National Nuclear Security Administration under Award Number DE-NA0003856, the University of Rochester, and the New York State Energy Research and Development Authority.

1. M. Sherlock and J. J. Bissell, Phys. Rev. Lett. **124**, 055001 (2020).
2. C. P. Ridgers *et al.*, Phil. Trans. R. Soc. A **379**, 20200017 (2021).
3. J. R. Davies *et al.*, Phys. Plasmas **24**, 062701 (2017).
4. S. A. Slutz *et al.*, Phys. Plasmas **17**, 056303 (2010).
5. G. Fiksel *et al.*, Rev. Sci. Instrum. **86**, 016105 (2015).
6. N. L. Kugland *et al.*, Rev. Sci. Instrum. **83**, 101301 (2012).
7. M. M. Marinak *et al.*, Phys. Plasmas **8**, 2275 (2001).
8. A. R. Bell, R. G. Evans, and D. J. Nicholas, Phys. Rev. Lett. **46**, 243 (1981).
9. A. F. A. Bott *et al.*, J. Plasma Phys. **83**, 905830614 (2017).
10. PlasmaPy Community *et al.*, PlasmaPy (Version 0.6.0), Zenodo, Accessed 14 March 2021, http://doi.org/10.5281/zenodo.4602818.

Inverse Ray Tracing on Icosahedral Tetrahedron Grids for Nonlinear Laser–Plasma Interactions Coupled to 3-D Radiation Hydrodynamics

A. Colaïtis,[1] I. V. Igumenshchev,[2] J. Mathiaud,[1] and V. N. Goncharov[2]

[1]Université de Bordeaux, Centre Lasers Intenses et Applications, France
[2]Laboratory for Laser Energetics, University of Rochester

Three major avenues to inertial confinement fusion (ICF) are currently being explored worldwide:[1] laser direct drive (LDD), laser (x-ray) indirect drive (LID), and magnetic drive using pulsed power. These approaches have in common the use of laser beams and face challenges related to laser–plasma instabilities (LPI's). LPI's are nonlinear microscopic processes that couple plasma eigenmodes (electron or ion plasma waves) to the laser beams or scattered light or each other.[2] In the case of LDD and LID, the main LPI's at play are cross-beam energy transfer (CBET), stimulated Raman scattering (SRS), stimulated Brillouin scattering (SBS), and two-plasmon decay (TPD). Their consequences for large-scale plasma hydrodynamics are often important, leading to significant loss of laser/target coupling, introducing asymmetries in target compression, and generating suprathermal-electron populations.[3]

While LPI's have a paramount influence in ICF, they are also difficult to model in radiation-hydrodynamic (RH) codes that describe the plasma motion at fluid scales. This relates to an incompatibility of dimensions between the typical plasma size (~mm) and driver duration (~ns) compared to the scales required to resolve the kinetic processes at play in LPI's (~nm and ~fs). These six-orders-of-magnitude differences in time and space prevent direct numerical calculations of LPI's in 3-D geometries at fluid scales. As such, they are often computed at reduced scales, for short periods of time, in a reduced number of dimensions, and/or for a limited number of laser beams. For these reasons, models for laser propagation in hydrodynamic codes have long been limited to the linear process of collisional absorption. This is usually modeled in the geometrical optics (GO) framework for computing laser trajectories,[4] which offers adequate performance at fluid scales, even in 3-D geometries.

Given the importance of LPI's in ICF, significant efforts have been made in the last 10 to 15 years to include reduced LPI models in fluid codes, mainly based on GO models for numerical efficiency. These reduced models must address two main questions: (1) how to compute laser intensities or fields in the GO framework, key properties for LPI's, and (2) how to account for the microscopic processes. The first issue stems from the infinitely thin property of GO rays, which prevents a straightforward definition of ray intensity. The GO framework also breaks down at laser caustics, which are prominent in LDD. The second issue relates to the formulation of theoretical models that reproduce microscopic physics from macroscopic quantities. Such models have been notably proposed for CBET by considering the laser wave as locally plane and homogeneous[5] and are used across a variety of codes. Significant technical difficulties arise, however, in coupling these models with the intensity calculation methods of GO. Usually, such details are handled with the introduction of free numerical parameters in CBET models, thereby allowing one to tune results of calculations to match experimental data. In this summary, we aim to propose a fluid-scale laser model, *IFRIIT*, which consistently follows the GO framework to compute laser fields and eliminates such free parameters. In addition, we present the coupling of *IFRIIT* to the *ASTER*[6] RH code for the specific spherical geometries of LDD. Calculations presented here were conducted in the framework of the OMEGA Laser System configuration and diagnostics.[7]

Our algorithm differs significantly from other methods implemented in RH codes on several key points: First, we make use of inverse ray tracing (IRT) to compute the laser propagation, as opposed to the method of forward ray tracing (FRT), which is usually employed. This is the first time an IRT method has been used for laser calculations coupled to plasma hydrodynamics in

RH fusion codes. Second, we decouple the laser grid from the hydrodynamics grid. This allows us to tailor a grid that is optimized for the resolution of the ray equations, leading to a better load balance for parallel computations. In addition, the laser grid itself is split into two grids: one for calculating ray electric fields and one for calculating ray trajectories. Furthermore, we employ a geodesic laser grid structure, contrary to the standard polar grids employed in 3-D RH codes. It is the first time that such a three-grid scheme has been employed for laser calculations. Third, we make use of the Etalon Integral method to compute laser fields in places where the GO framework breaks down.[8] This is also a new technique for RH codes, which is enabled by the use of IRT and allows us to remove the free parameters used in standard codes to set caustic fields. Fourth, the fields reconstructed from GO using IRT are at a higher order in space than conventional grid binning methods used to compute absorption and fields. While it is possible to achieve a higher order in space for fields using FRT through interpolation or local derivative estimation, the IRT method natively obtains this higher order. This is an important point in 3-D ICF implosions, where noise issues stemming from low convergence in the number of rays per cell for some FRT schemes, or low-order field estimation methods, will often be detrimental. Fifth, the laser code and the RH codes are also decoupled in time, allowing both codes to iterate asynchronously. Indeed, laser computations are often more costly than hydrodynamic ones (when including LPI's) but do not need updating as often. This is also the first time a RH code implements a desynchronized laser scheme. Finally, the use of IRT has additional advantages: e.g., it allows a native separation of the laser field between the various reflected components (so-called "sheets") that, for example, enable one to precisely account for self-interaction of the incident and reflected fields of beams through CBET. It also considerably speeds up pump-depletion iterations in CBET algorithms by allowing us to update only part of the ray equations.

Applications to direct-drive implosions for ICF have been considered for which a geodesic icosahedron grid is implemented in *IFRIIT*. The performances of the *ASTER*/*IFRIIT* coupling have been demonstrated by conducting simulations of cryogenic implosions performed on the OMEGA Laser System, in the presence of various sources of 3-D effects: laser port geometry, cross-beam energy transfer, beam imbalance, and target misalignment [see Fig. 1, (p. 136)]. The code was found to have sufficiently low numerical noise to accurately model the high-convergence ICF implosions without introducing spurious modes. A comparison with neutron data for a cryogenic implosion experiment has also shown excellent agreement for the laser–plasma coupling (notably the measured bang time). More-recent developments (to be published in an upcoming paper) include the modeling of the polarized CBET interaction. In the latter case, simulations with the full post-shot data allow the magnitude of the measured DT flow to be reproduced, as well as approaching the measured direction of the flow.

This material is based upon work supported by the Department of Energy National Nuclear Security Administration under Award Number DE-NA0003856, the University of Rochester, and the New York State Energy Research and Development Authority. This work was granted access to the HPC resources of TGCC computer cluster (Ref. 9) under the allocation 2020-A0070506129 and 2021-A0090506129 made by GENCI.

1. R. Betti and O. A. Hurricane, Nat. Phys. **12**, 435 (2016).
2. W. L. Kruer, *The Physics of Laser Plasma Interactions*, 1st ed. (CRC Press, Boca Raton, FL, 2003).
3. D. Batani *et al.*, Nucl. Fusion **54**, 054009 (2014).
4. T. B. Kaiser, Phys. Rev. E **61**, 895 (2000).
5. P. Michel *et al.*, Phys. Plasmas **16**, 042702 (2009).
6. I. V. Igumenshchev *et al.*, Phys. Plasmas **23**, 052702 (2016).
7. T. R. Boehly *et al.*, Opt. Commun. **133**, 495 (1997).
8. A. Colaïtis *et al.*, Phys. Plasmas **26**, 032301 (2019).
9. Très Grand Centre de calcul du CEA (TGCC), Accessed 6 October 2021, http://www-hpc.cea.fr/en/complexe/tgcc.htm.

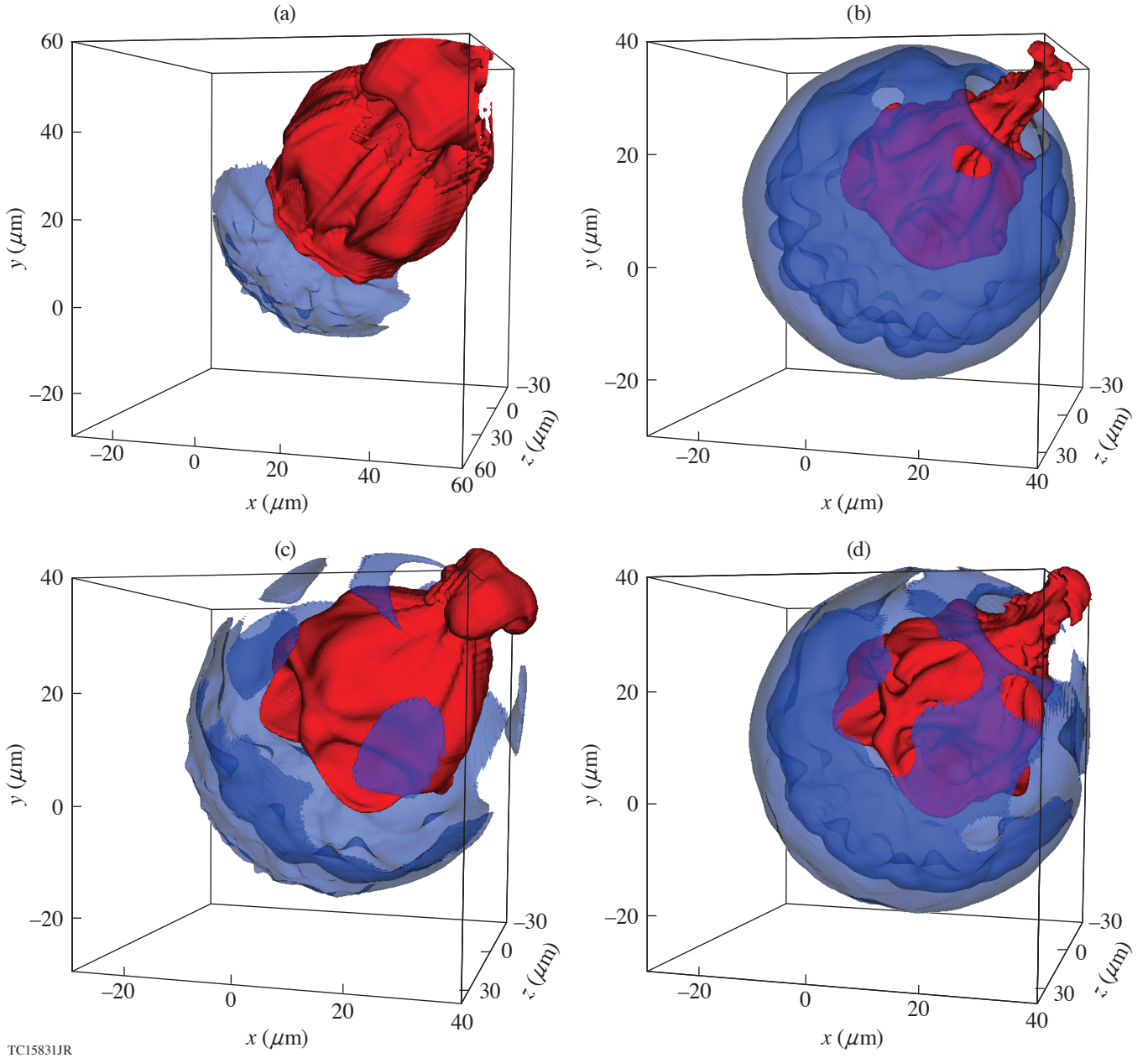

Figure 1
Academic test case of the effect of large offset and beam imbalance on cryogenic targets, illustrating how CBET can mitigate such effects. [(a),(b)] The target at stagnation in the presence of a 40-μm positioning offset in the $\theta = 65$, $\varphi = 45$ direction, and [(c),(d)] a 5% beam imbalance imposing a mode 1 in the same direction as the target offset. Run results without [(a),(c)] and with [(b),(d)] CBET enabled. In all figures, the 100-g/cm^3 density isocontour is shown in blue, the 50/50 DT ice/gas fractional volume isocontour is shown in red, and the axis ticks are in units of microns. The simulation setup is that of shot 94712.

Experimentally Inferred Fusion-Yield Dependencies of OMEGA Inertial Confinement Fusion Implosions

A. Lees,[1,2] R. Betti,[1,2,3] J. P. Knauer,[1] V. Gopalaswamy,[1,2] D. Patel,[1,2] K. M. Woo,[1] K. S. Anderson,[1] E. M. Campbell,[1] D. Cao,[1] J. Carroll-Nellenback,[1] R. Epstein,[1] C. J. Forrest,[1] V. N. Goncharov,[1] D. R. Harding,[1] S. X. Hu,[1] I. V. Igumenshchev,[1] R. T. Janezic,[1] O. M. Mannion,[1,3] P. B. Radha,[1] S. P. Regan,[1] A. Shvydky,[1] R. C. Shah,[1] W. T. Shmayda,[1] C. Stoeckl,[1] W. Theobald,[1] and C. A. Thomas[1]

[1]Laboratory for Laser Energetics, University of Rochester
[2]Department of Mechanical Engineering, University of Rochester
[3]Department of Physics and Astronomy, University of Rochester

Inertial confinement fusion[1] implosions are complex nonlinear processes that are highly sensitive to many input parameters. The lack of an accurate simulation capability, the low shot rate of laser implosion facilities, and the effects of shot-to-shot variations make it difficult to extract single parameter dependencies, thereby preventing guided improvements in implosion performance. In this summary, the different dependencies of the fusion yield are extracted from the OMEGA[2] experimental database of 177 implosions. The importance of these results is twofold: First, they identify the degradation mechanisms; second, they enable predictions of how the yield improves if each degradation is mitigated. When applied to OMEGA implosions the results indicate that the highest yield achievable on OMEGA should exceed 2×10^{14} neutrons with only minor adjustment to the laser pointing and by reducing the fill age. Yields close to 3×10^{14} are predicted if the degradation from R_b/R_t is mitigated.

Generalizing the conclusions of Ref. 3 to include the effects of variable systematic nonuniformity seeds and experimental input parameters that are not included in 1-D simulations, a physics-based statistical mapping model [see Eq. (1)] is derived for the measured fusion yield Y^{exp}. The yield is assumed to be dominated by the implosion velocity, which is typically well simulated by the 1-D code *LILAC*,[4] as indicated by shell trajectory measurements;[5] therefore, the yield is expected to depend on the simulated 1-D yield $Y_{1\text{-D}}^{sim}$. The statistical model is written in terms of the yield-over-clean (YOC), leading to the following intuitive formulation of the fusion yield:

$$Y^{exp} = \mathrm{YOC}^{exp} Y_{1\text{-D}}^{sim}$$
$$\mathrm{YOC}^{exp} \approx \mathrm{YOC}_h \mathrm{YOC}_f \mathrm{YOC}_b \mathrm{YOC}_{\ell=1} \mathrm{YOC}_{res}, \tag{1}$$

where the degradation due to hydrodynamic instabilities from systematic nonuniformities is denoted as YOC_h; YOC_f is the degradation due to DT fill age, tritium damage, and ^{3}He accumulation; YOC_b is the degradation from finite laser beam size; and $\mathrm{YOC}_{\ell=1}$ is the degradation from the $\ell = 1$ mode. YOC_{res} denotes a weak (≤15% over the entire database) residual size scaling not captured by 1-D hydrocodes[6,7] and is approximately constant for high-performance OMEGA implosions. Each YOC term is analyzed and extracted by mapping onto the experimental database.

The yield degradation from $\ell = 1$ can be approximated as a power law of the temperature ratio between the maximum and minimum apparent ion temperature $R_T = T_l^{max} / T_l^{min}$ (Ref. 8). Since the T_i measurement error is about 10%, only implosions with R_T greater than a minimum threshold $R_T^{min} \approx 1.1$ are expected to exhibit detectable degradation. Therefore, the degradation from the $\ell = 1$ mode is approximated as

$$\mathrm{YOC}_{\ell=1} \sim \hat{R}_T^{\mu}, \hat{R}_T \equiv \max\left[1, \frac{R_T}{R_T^{\min}}\right]. \tag{2}$$

Here the values of μ and $R_T^{\min}$ are obtained through the global mapping onto the data.

$\mathrm{YOC_f}$ depends on the time between the DT fill and the shot time (fill age) as well as the tritium and deuterium concentrations (θ_T and θ_D, respectively). Instead of the fill age, one can use the 1-D–simulated yield degradation $\xi\mathrm{He} = Y^{\mathrm{sim}}_{\text{1-D,He}}/Y^{\mathrm{sim}}_{\text{1-D}}$, where $Y^{\mathrm{sim}}_{\text{1-D,He}}$ includes the ^{3}He produced over the course of the fill age, all of which is assumed to be accumulated in the vapor region. Power-law dependencies are assumed, leading to

$$\mathrm{YOC_f} \sim \theta_\mathrm{T}^{\delta}\theta_\mathrm{D}^{\nu}\xi_{\mathrm{He}}^{\phi}. \tag{3}$$

The degradation from finite laser spot size $\mathrm{YOC_b}$ can be approximated through a power of laser beam to target radius $R_\mathrm{b}/R_\mathrm{t}$:

$$\mathrm{YOC_b} \sim \left(R_\mathrm{b}/R_\mathrm{t}\right)^{\gamma} \tag{4}$$

with $\gamma \approx 2.4$ in 3-D simulations.[9] Here, as for all the other degradations, the exponent γ is determined by the mapping to the data.

A functional relation of simulated 1-D parameters that best maps the degradation from hydrodynamic instabilities, $\mathrm{YOC_h}$ is constructed by combining in-flight aspect ratio (IFAR) and the shell adiabat $\alpha_\mathrm{F} = P_\mathrm{a}/P_\mathrm{F}$ (ratio of the ablation pressure to the Fermi degenerate pressure), into a single parameter $I_\alpha \equiv \left(\alpha_\mathrm{F}/3\right)^{1.1}/(\mathrm{IFAR}/20)$ as indicated in Refs. 10 and 11. The convergence ratio (CR) is added to better account for the degradation from low- and mid-mode asymmetries. To account for inaccuracies in modeling shock transit, the shell thickness is included through the dimensionless parameter $\hat{D} \equiv R_\mathrm{out}/R_\mathrm{in}$ representing the ratio between the outer and inner shell radii. Therefore $\mathrm{YOC_h}$ is approximated as $\mathrm{YOC_h} \sim I_\alpha^{\eta}\mathrm{CR}^{\hat{\omega}}D^{\varepsilon}$. At sufficiently large adiabats and low IFAR's, implosions become stable to short-wavelength modes and the benefits of higher adiabat and low IFAR are expected to decrease.[10] Therefore, a piecewise value of η is used above and below a critical value (I_c) of I_α. The final form of the hydrodynamic degradation is then written as

$$\mathrm{YOC_h} \sim \hat{I}_\alpha^{\eta} C_R^{\omega} D^{\varepsilon}, \tag{5}$$

where $\hat{I}_\alpha = I_\alpha/I_\mathrm{c}$ and $\eta = \eta_< \Theta\left(1 - \hat{I}_\alpha\right) + \eta_> \Theta\left(\hat{I}_\alpha - 1\right)$ with $\Theta(x)$ representing the Heaviside step function.

The power indices in Eqs. (2)–(5) are determined by χ^2 minimization over the entire OMEGA implosion database and the two threshold parameters $R_T^{\min}$, I_c were chosen to minimize the cross-validation error. The results are summarized in Table I including the 95% confidence level for each exponent. Each dependence can be visualized by isolating the corresponding YOC and comparing with the power-law approximation:

$$\mathrm{YOC}_j^{\mathrm{exp}} \equiv \frac{\mathrm{YOC}^{\mathrm{exp}}}{\Pi_{i \neq j}\mathrm{YOC}_i} \rightarrow \mathrm{YOC}_j. \tag{6}$$

The plots in Fig. 1 show the comparison in Eq. (6) for the dependencies in Eq. (1).

General conclusions can be readily extracted from this analysis. First, the degradation from the $\ell = 1$ is as predicted by the 3-D simulations with a power index $\mu \approx -1.44$ and a threshold factor $R_T^{\min} = 1.14$ from the T_i measurement error. Such a good agreement with the simulations confirms the accuracy of the mapping technique to extract the correct trends from the data. Reasonable agreement with 1-D–simulated degradation due to ^{3}He accumulation is indicated by $\varphi \approx 1.39$ close to unity. Furthermore, the degradation in two extremely long fill age targets (45 and 90 days) is well predicted as shown by the two points farthest to the left on Fig. 1(b), adding confidence that the model is correctly accounting for the effect of ^{3}He accumulation. As a result of this

Table I: Power indices and confidence intervals for all the degradation terms as a result of fitting the model in Eq. (1) to the OMEGA database.

Parameter	Power index	95% confidence interval
$\hat{R}_T^{\mu}$	$\mu = -1.44$ $R_{\rm T}^{\rm min} = 1.14$	$\mu = -1.61$ to -1.28
$\xi_{\rm He}^{\phi}$	$\phi = 1.39$	$\phi = 1.25$ to 1.54
$\theta_{\rm T}^{\delta}$	$\delta = 1.97$	$\delta = 1.00$ to 2.90
$\theta_{\rm D}^{\nu}$	$\nu = 1.16$	$\nu = 0.54$ to 1.79
$(R_{\rm b}/R_{\rm t})^{\gamma}$	$\gamma = 2.97$	$\gamma = 2.72$ to 3.24
$\hat{I}_{\alpha}^{\eta}$	$\eta_{<} = 1.06$ $\eta_{>} = 0.45$ $I_{\rm c} = 0.8$	$\eta_{<} = 0.91$ to 1.21 $\eta_{>} = 0.40$ to 0.49
C_R^{ω}	$\omega = -0.97$	$\omega = -1.05$ to -0.89
$\hat{D}^{\varepsilon}$	$\varepsilon = -3.35$	$\varepsilon = -4.11$ to -2.58

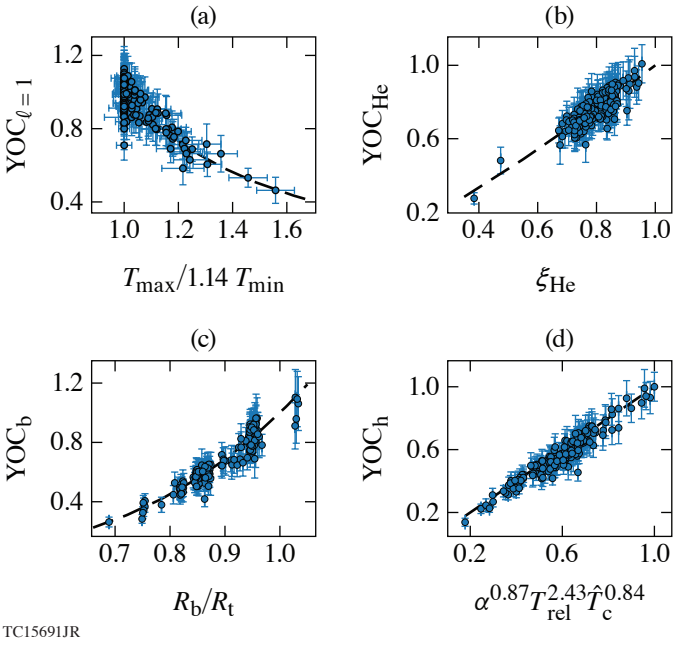

Figure 1
The individual degradations due to (a) $\ell = 1$ mode, (b) ^{3}He accumulation in the vapor, (c) finite beam size, and (d) hydrodynamic instabilities extracted from the OMEGA database according to Eq. (6). The dashed lines indicate the power laws from the model; the power indices are given in Table I.

analysis, OMEGA shot 96806 was designed with the shortest-ever fill age of 3 days, achieving the highest performance on OMEGA at the time with a neutron yield of 1.53×10^{14} and an areal density of 157±15 mg/cm^2 at a laser energy of 27.3 kJ.

Shot 96806 was subsequently repeated with a fill age of 8 days (shot 96808) resulting in a 14% reduction in fusion yield, as predicted by the statistical model (13%). Another conclusion can be drawn about the isotopic composition of the DT ice layer since maximizing the term $\theta_{\rm T}^{1.97}\,(1-\theta_{\rm T})^{1.16}$ gives the optimal tritium concentration at $\theta_{\rm T} \approx 0.6$. The mapping to data reveals a strong $R_{\rm b}/R_{\rm t}$ correlation with a power index of $\gamma = 2.97$, which is stronger than indicated by 3-D simulations of the beam mode in Ref. 9. Furthermore, the highest-performing implosions with $R_{\rm b}/R_{\rm t} \approx 0.87$ show a significant (35%) degradation from this mechanism,

whereas post-shot 3-D simulations show negligible degradation due to the beam mode. This indicates that new physics is at play, which is an active area of research, and it can include new sources of nonuniformities from the laser beam geometry as well as 1-D physics model deficiencies most likely related to the reduction of cross-beam energy transfer, when $R_b < R_t$. Lastly, the mapping model indicates strong degradation due to hydrodynamic effects (YOC_h) at low adiabat, high convergence, and high IFAR [Fig. 1(d)]. The results indicate that the highest yields can be achieved only at high adiabat and low IFAR with the maximum yield occurring at adiabats >4.5.

This material is based upon work supported by the Department of Energy National Nuclear Security Administration under Award Number DE-NA0003856, the University of Rochester, and the New York State Energy Research and Development Authority.

1. J. Nuckolls *et al.*, Nature **239**, 139 (1972).
2. T. R. Boehly *et al.*, Opt. Commun. **133**, 495 (1997).
3. V. Gopalaswamy *et al.*, Nature **565**, 581 (2019).
4. J. Delettrez *et al.*, Phys. Rev. A **36**, 3926 (1987).
5. D. T. Michel *et al.*, Phys. Rev. Lett. **114**, 155002 (2015).
6. W. Theobald *et al.*, "OMEGA Subscale Cryogenic Implosions in Symmetric and Polar-Direct-Drive Beam Geometry," presented at the 62nd Annual Meeting of the American Physical Society Division of Plasmas Physics, Memphis, TN, 9–13 November 2020.
7. C. A. Thomas *et al.*, "Quantifying the Effects of Scale and Illumination Geometry in Laser Direct Drive," presented at the 62nd Annual American Physical Society Division of Plasma Physics, Memphis, TN, 9–13 November 2020.
8. K. M. Woo *et al.*, Phys. Plasmas **27**, 062702 (2020).
9. V. Gopalaswamy *et al.*, "Using Statistics to Predict, Design, and Understand Fusion Experiments," submitted to Physics of Plasmas.
10. V. N. Goncharov *et al.*, Phys. Plasmas **21**, 056315 (2014).
11. H. Zhang *et al.*, Phys. Plasmas **27**, 122701 (2020).

Density Evolution After Shock Release from Laser-Driven Polystyrene Targets in Inertial Confinement Fusion

A. Shvydky,[1] D. Haberberger,[1] A. V. Maximov,[1] R. Boni,[1] D. Cao,[1] J. Carroll-Nellenback,[1] D. H. Froula,[1] V. N. Goncharov,[1] S. X. Hu,[1] I. V. Igumenshchev,[1] S. T. Ivancic,[1] V. V. Karasiev,[1] J. P. Knauer,[1] P. M. Nilson,[1] P. B. Radha,[1] S. P. Regan,[1] J. R. Rygg,[1] T. C. Sangster,[1] M. D. Rosen,[2] and V. A. Smalyuk[2]

[1]Laboratory for Laser Energetics, University of Rochester
[2]Lawrence Livermore National Laboratory

In laser-driven inertial confinement fusion (ICF), a cryogenically cooled spherical shell of deuterium–tritium (DT) fuel is imploded and compressed by material ablation to form a high-areal-density confinement around a central spot where conditions for ignition are created.[1,2] At the beginning of the implosion, multiple shocks are launched into the ablator and DT-ice shell. After the shocks break out of the shell into the gas, the shell starts to accelerate inward. The density gradient at the inner part of the shell, formed by the shock release, controls the dynamics of shell deceleration and limits the final hot-spot convergence ratio and peak fuel areal density.

To have predictive capability for ICF implosions it is important that radiation-hydrodynamic codes are able to accurately simulate the density profile of the material release ahead of the high-density shell under conditions relevant to ICF implosions (zero to a few-times solid-state density, a few to tens of eV temperature, and a few to tens of megabars of pressure). It is very difficult to probe the density profile in the material released from the inner side of the DT shell because of the low opacity of DT and various complications due to geometry. While techniques are being developed for direct density measurements during a cryogenic implosion, several key questions relevant to material release can be studied using planar foils. In recent experiments[3] release plasma profiles in planar foils were measured for the first time using optical interferometry. Results indicate that material release is enhanced in experiments compared to that predicted by radiation-hydrodynamics simulation and that the low-density part of the plasma profile in the release strongly depends on conditions at the back (opposite to the laser drive) surface right before the shock breakout. A density gradient at the back surface enhances the expansion compared to that in a classical release from a sharp foil–vacuum interface. It was hypothesized[4,5] that the formation of a density gradient at the back surface prior to shock arrival is the result of an early expansion caused by coronal x-ray preheating.

In this study, the underlying mechanisms for the enhanced release observed in experiments are examined through a systematic comparison of the experiments to radiation-hydrodynamic simulation using various thermal- and radiation-transport models and opacity and equation-of-state (EOS) tables. We find that the rarefaction-wave expansion is highly sensitive to the radiation-transport model used in the simulations. When radiation transport was treated using the S_n radiation-transport method[6] the release experiments[5] were consistently explained within the framework of radiation hydrodynamics.

The shock-release experiment carried out on the OMEGA EP Laser System used a 37-μm-thick, 4-mm-diam hemispherical CH shell (to prevent parallax in line-integrated diagnostics) and was irradiated from its inner side (front side for the laser) by two ultraviolet (UV) laser beams with a wavelength of 351 nm [see Fig. 1(a)]. With a combined laser energy of 6 kJ in a 5-ns square pulse, an overlapped intensity of 3×10^{14} W/cm^2 was obtained in a 750-μm-diam eighth-order super-Gaussian spot created using distributed phase plates. The two laser beams heated the front surface of the foil, creating ~30-Mbar ablative pressure that drove an ~65-km/s shock through the foil. At about 670 ps from the start of the laser pulse, the shock broke out from the back side of the foil and formed a rarefaction wave that expanded into the vacuum. The foil started to accelerate at about 1.3 ns, the time at

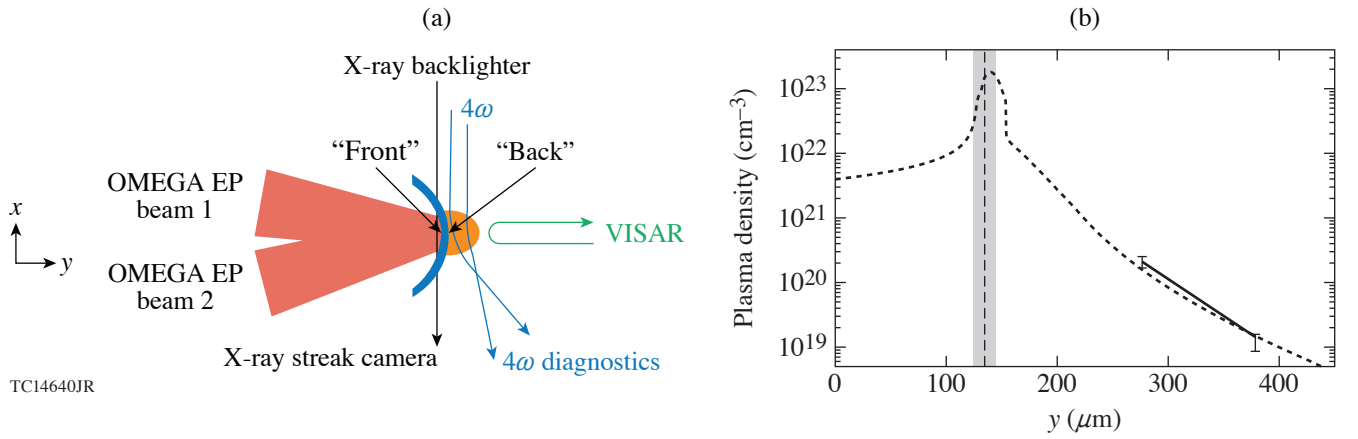

Figure 1
(a) The experimental setup used two 5-ns beams to drive a hemispherical CH shell; x-ray streaked radiography was used to measure the in-flight shell position; 4ω laser interferometry to measure the low-density profile in the rarefaction wave; and the velocity interferometry system for any reflector (VISAR) to measure the motion of the back surface of the shell. (b) The measured (solid line) and simulated (dotted curve) plasma density profiles at 2 ns. The vertical dashed line represents the peak shell positions as measured by the streak camera (with error bars shown by the shaded regions).

which the head of the rarefaction wave reached the front of the foil. The 4ω (263-nm-wavelength) interferometer[7] captured the rarefaction wave's plasma-density profile at 1, 2, 3, and 4 ns. Due to noise limitations this profile is accurate only in the low-density region measured by the 4ω probe from ~10^{19} cm^{-3} to ~10^{20} cm^{-3}; the measured density profile is further limited by the collection angle of the 4ω probe lens. As an example, Fig. 1(b) (solid line) shows the lineout of the plasma density inferred from the 2-ns interferogram taken along the middle of the drive ($x = 0$). For convenience in comparing the time evolution of the low-density part of the rarefaction wave to simulations, we extract the positions of the 10^{19}-cm^{-3} and 10^{20}-cm^{-3} plasma density locations along the middle of the drive and plot them versus time as shown in Fig. 2.

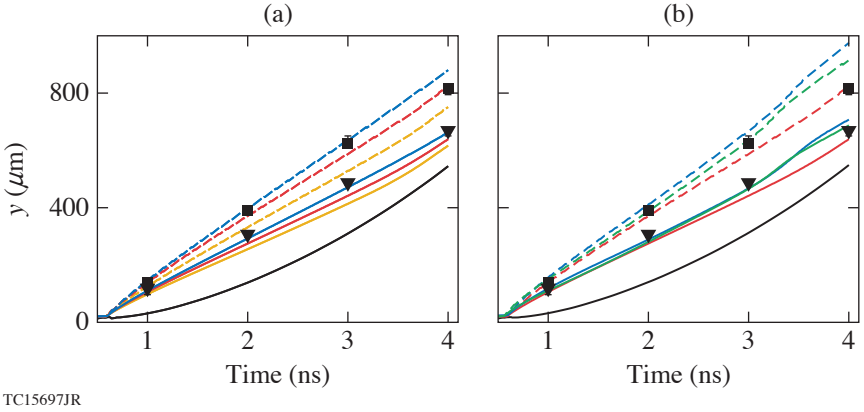

Figure 2
(a) Positions of 10^{19}-cm^{-3}-(dashed curves) and 10^{20}-cm^{-3} (solid curves) plasma density versus time from simulations performed with S_n and AOT (red), S_n and CRE (blue), and MGD and AOT (yellow); all with *SESAME* EOS. (b) Positions of 10^{19}-cm^{-3} (dashed curves) and 10^{20}-cm^{-3} (solid curves) plasma density versus time are from simulations performed with *SESAME* (red), QEOS (blue), and the ideal-gas (green) EOS; all with S_n and AOT. In (a) and (b), black squares (triangles) mark 10^{19}-cm^{-3} (10^{20}-cm^{-3}) plasma density positions and the solid black curve marks the shell trajectory.

Simulations were performed with the 1-D Lagrangian radiation-hydrodynamic code *LILAC*. The laser drive was adjusted to account for transverse thermal losses, which are not modeled in 1-D simulations, and to match the foil trajectory, which was experimentally measured and accurately simulated with the 2-D radiation-hydrodynamic code *DRACO*. An example of the simu-

lated plasma density profile taken at 2 ns is shown in Fig. 1(b) (dotted curve). The density peak ($\sim 1.8 \times 10^{23}$ cm^{-3} at $y = 140$ μm) corresponds to the shell, the rising part of the density profile on the left of the shell corresponds to the corona, and the decaying part of the density profile on the right of the shell corresponds to the rarefaction wave. The simulated scale length and extent of the density profiles at all four times are in good agreement with the measurements and show a weak dependence on the opacity and EOS tables as illustrated in Fig. 2. This insensitivity indicates that radiation-hydrodynamic simulations capture essential physics in the evolution of the low-density part of the plasma profiles in the release from a CH foil into vacuum. The simulations in Fig. 2 use astrophysical opacity tables (AOT's), collisional-radiative-equilibrium (CRE) opacity tables, *SESAME* (table 7593), quotidian equation of state (QEOS), and the ideal-gas EOS models. Simulations in previous studies reported in Ref. 3, which showed much shorter expansion and scale length of the electron density profile in the release [see yellow curves in Fig. 2(a)], used a flux-limited multigroup diffusion (MGD) method[8] to model the radiation transport. MGD is the standard method for modeling radiation transport in ICF radiation-hydrodynamic codes because of its computational efficiency. The simulations shown in red, blue, and green in Fig. 2 use a more-accurate, albeit more computationally expensive, multigroup S_n radiation-transport method (method of ordinates).[6]

In summary, we have presented a consistent interpretation of the experimental results (the shock breakout time, shell trajectory, and rarefaction-wave plasma density profile) within the framework of radiation hydrodynamics: (1) The simulations showed that the low-density part of the plasma profile in the rarefaction wave formed when a shock is released from the back surface of a CH foil strongly depends on conditions at the back surface right before the shock breakout. A density gradient at the back surface enhances the expansion of the rarefaction wave compared to that in a classical release from a sharp foil–vacuum interface. When the shock travels over the low-density part of the gradient, it heats the material to higher temperatures than when the shock travels over the bulk of the shell. The higher temperature increases the sound speed of the shocked material, resulting in an enhanced release. (2) Simulations predict an early expansion (during the shock transit time) of the back surface of the foil caused by preheat by coronal x rays. Experiments using the VISAR diagnostic measured movement of the back surface of the foil during the shock transit time. The essential role of coronal x-ray preheat in the release was verified by experiments with a buried Au layer that showed a significantly reduced rarefaction-wave expansion in comparison with the baseline experiments. (3) To predict the low-density profile in the rarefaction wave, radiation-hydrodynamic simulations must accurately model preheat of the back surface of the foil by coronal x rays and the early back-surface expansion. This requires the S_n radiation transport model to accurately describe the passage of the coronal radiation through CH material under the drive conditions.

This material is based upon work supported by the Department of Energy National Nuclear Security Administration under Award Number DE-NA0003856, the University of Rochester, and the New York State Energy Research and Development Authority.

1. R. S. Craxton *et al.*, Phys. Plasmas **22**, 110501 (2015).
2. E. M. Campbell *et al.*, Matter Radiat. Extremes **2**, 37 (2017).
3. D. Haberberger *et al.*, Phys. Rev. Lett. **123**, 235001 (2019).
4. A. Shvydky *et al.*, Bull. Am. Phys. Soc. **64**, BAPS.2019.DPP.NO5.8 (2019).
5. M. D. Rosen, Bull. Am. Phys. Soc. **65**, BAPS.2020.DPP.CP17.3 (2020).
6. S. Chandrasekhar, *Radiative Transfer* (Dover Publications, New York, 1960).
7. A. Howard *et al.*, Rev. Sci. Instrum. **89**, 10B107 (2018).
8. D. Mihalas and B. Weibel-Mihalas, *Foundations of Radiation Hydrodynamics* (Oxford University Press, New York, 1984).

Experimental Characterization of Hot-Electron Emission and Shock Dynamics in the Context of the Shock-Ignition Approach to Inertial Confinement Fusion

A. Tentori,[1] A. Colaïtis,[1] W. Theobald,[2,3] A. Casner,[1] D. Raffestin,[1] A. Ruocco,[1,4] J. Trela,[1] E. Le Bel,[1] K. S. Anderson,[2] M. S. Wei,[2] B. J. Henderson,[2] J. L. Peebles,[2] R. Scott,[4] S. Baton,[5] S. A. Pikuz,[6] R. Betti,[2,3,7] M. Khan,[8] N. Woolsey,[8] and D. Batani[1]

[1]Centre Lasers Intenses et Applications, CELIA, Université Bordeaux, France
[2]Laboratory for Laser Energetics, University of Rochester
[3]Department of Mechanical Engineering, University of Rochester
[4]Central Laser Facility, STFC Rutherford Appleton Laboratory, United Kingdom
[5]Laboratoire pour l'Utilisation des Lasers Intenses, CNRS-Ecole Polytechnique-CEA-Sorbonne Universités, France
[6]Joint Institute for High Temperatures of Russian Academy of Sciences, Russia
[7]Department of Physics and Astronomy, University of Rochester
[8]York Plasma Institute, Department of Physics, University of York, United Kingdom

Shock ignition (SI) is an alternative approach to direct-drive inertial confinement fusion based on the separation of the compression and the ignition phases.[1,2] The high laser intensity required in the ignition phase exceeds the thresholds for the generation of laser–plasma instabilities,[3] generating a large amount of suprathermal electrons. Depending on their characteristics these electrons could preheat the hot spot with detrimental effects for the SI scheme, or assist in generating a strong shock.[4]

Here we report on a planar target experiment conducted on the OMEGA EP Laser System aimed at characterizing the hot-electron source and the shock dynamics using laser parameters relevant for SI. A UV ($\lambda = 351$-nm) laser beam was tightly focused on planar multilayer targets, providing a nominal vacuum laser intensity of $\sim 10^{16}$ W/cm^2 with a pulse duration of ~1 ns. The laser energy delivered was ~1250 J. The planar targets consisted of 500-μm-diam disks with two layers (175 or 250 μm of CH, or 20 or 10 μm of Cu). These were mounted on a 50-μm-thick CH slab intended to inhibit hot-electron recirculation. The UV interaction laser impinged on the front of the CH ablator, generating a strong shock and large amounts of hot electrons. The shock propagation was monitored using x-ray time-resolved radiographs; the x-ray source was created by focusing a second laser beam (4×10^{14} W/cm^2, 3-ns pulse duration) on a V foil. This scheme allows production of copious amounts of V K_α x rays that pass through the target; the x rays are then detected by a four-strip x-ray framing camera (XRFC).[5] The camera was equipped with a 4×4 array of 20-μm-diam pinholes, capturing 16, 2-D images of the shock front at different times with 6× magnification (Fig. 1).

Hot electrons were characterized using separate x-ray spectrometers. The hot-electron–produced bremsstrahlung radiation was diagnosed by two time-integrating hard x-ray spectrometers (BMXS's).[6] The instruments are composed of a stack of 15 imaging plates alternated by filters of different metals. The total yield of Cu K_α was measured by an absolutely calibrated zinc von Hamos x-ray spectrometer (ZnVH).[7]

The post-processing of the spectrometers relies on cold Monte Carlo methods [Geant4 (Ref. 8)] in which the electron transport and the x-ray generation on the diagnostics are simulated. In particular, electrons are assumed to be energetically described by a 2-D Maxwellian function:

$$f_e(E) = \frac{N_e}{T_h} e^{-E/T_h}.$$

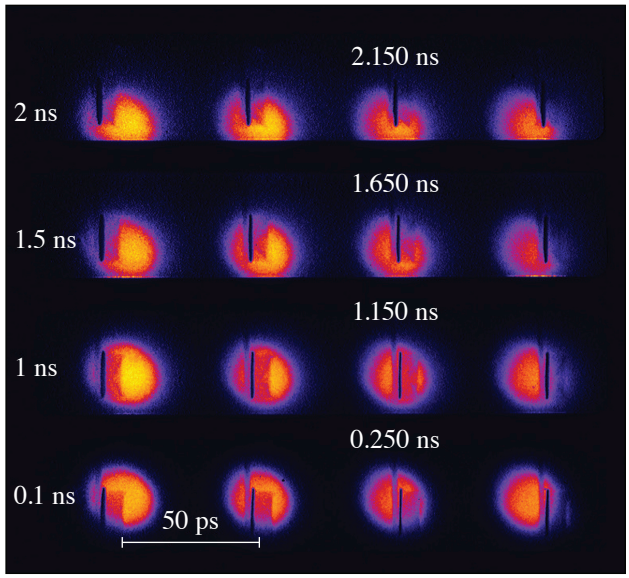

Figure 1
Array of 2-D radiographs captured at various times by the XRFC for shot 28407. Line spacing between each image is 50 ps.

The parameters N_e and T_h that reproduce both the experimental bremsstahlung spectrum and the K_α signal detected by the BMXS's and the ZnVH are calculated. A large uncertainty on the values of N_e and T_h arises because of the disagreement among the results from different shots and because of the systematic disagreement between the two diagnostics. A disagreement of ~25% is also noted in the simulations of the K_α signal using two different libraries of Geant4.[9,10] As such, T_h ranges from 20 keV up to 50 keV and N_e from 4×10^{16} down to 5×10^{15}. It is therefore necessary to consider the hydrodynamic evolution of the target to reduce these large ambiguities. In particular, we considered three representative hot-electron distribution functions to use as input in the hydrodynamic simulations to determine which *combination* of laser to hot-electron energy conversion efficiency η and average temperature T_h better reproduces the experimental behavior observed in the radiographs. The three representative $f_e(E)$ are reported in Table I.

Table I: Parameters of Maxwellian functions $f_e(E)$ obtained from post-processing the BMXS and ZnVH diagnostic data for shot 28407, used as input in *CHIC*.

$f_e(E)$			
	T_h (keV)	N_e (10^{16})	η (%)
$f_{e1}(E)$	26	3.4	11
$f_{e2}(E)$	35	1.4	6
$f_{e3}(E)$	45	0.5	3

The radiation-hydrodynamic simulations were performed with the code *CHIC*,[11] in which a model of hot-electron transport is included.[12] The shock position and the copper plate expansion are the figures of merit used to characterize the hot-electron source. Different intensities and kinetic energies of the hot-electron beam will strongly affect the variation in time of these two quantities. The simulations showed that an electron beam described by $f_{e1}(E)$ and $f_{e2}(E)$ allows reproduction of the experimental behavior.

According to the simulations hot electrons with these characteristic values of η and T_h increase the shock pressure up to 150 Mbar, 25 Mbar more than the value predicted by simulations without the hot-electron beam included. The effects of such an electron distribution function on a typical SI imploded target[13] were evaluated using a simple ideal-gas equation-of-state model. An increase of the shell adiabat was calculated using the high conversion efficiency found in the experiment, which could represent an issue for the SI scheme.

This material is based upon work supported by the Department of Energy National Nuclear Security Administration under Award Number DE-NA0003856, the University of Rochester, and the New York State Energy Research and Development Authority.

1. V. A. Shcherbakov, Sov. J. Plasma Phys. **9**, 240 (1983).
2. R. Betti *et al*., Phys. Rev. Lett. **98**, 155001 (2007).
3. W. L. Kruer, *The Physics of Laser Plasma Interactions*, edited by D. Pines, 1st ed. (CRC Press, Boca Raton, FL, 2003).
4. S. Gus'kov *et al*., Phys. Rev. Lett. **109**, 255004 (2012).
5. D. K. Bradley *et al*., Rev. Sci. Instrum. **63**, 4813 (1992).
6. C. D. Chen *et al*., Rev. Sci. Instrum. **79**, 10E305 (2008).
7. L. C. Jarrott *et al*., Rev. Sci. Instrum. **88**, 043110 (2017).
8. S. Agostinelli *et al*., Nucl. Instrum. Methods Phys. Res. A **506**, 250 (2003).
9. F. Salvat, *PENELOPE 2018: A Code System for Monte Carlo Simulation of Electron and Photon Transport*, Nuclear Energy Agency (OECD Publishing, Paris, France, 2019).
10. S. T. Perkins *et al*., Lawrence Livermore National Laboratory, Livermore, CA, Report UCRL-50400 (1991).
11. J. Breil, S. Galera, and P.-H. Maire, Comput. Fluids **46**, 161 (2011).
12. A. Colaïtis *et al*., Phys. Rev. E **92**, 041101(R) (2015).
13. A. Colaïtis *et al*., Phys. Plasmas **23**, 072703 (2016).

Experimental Observations of Laser-Driven Tin Ejecta Microjet Interactions

A. M. Saunders,[1] C. V. Stan,[1] K. K. Mackay,[1] B. Morgan,[1] J. A. K. Horwitz,[1] S. J. Ali,[1] H. G. Rinderknecht,[2] T. Haxhimali,[1] Y. Ping,[1] F. Najjar,[1] J. Eggert,[1] and H.-S. Park[1]

[1]Lawrence Livermore National Laboratory
[2]Laboratory for Laser Energetics, University of Rochester

The study of metal ejecta microjet interactions has broad applicability to fields ranging from planetary formation[1] to cloud interaction dynamics.[2] An ejecta microjet forms when a strong shock travels through a metal sample and, upon reaching the opposite side, interacts with a micron-scale surface perturbation, such as a dent or a groove. The surface perturbation then inverts to form a jet of micron-scale material traveling at a high velocity, often exceeding 1 km/s (~2200 mi/h) (Ref. 3). The jet is comprised of particles with average diameters of ~1 μm (Ref. 4). While extensive work has been performed to understand microjet formation and evolution, collisions of interacting microjets have been neglected. We present the first measurements of interaction behavior between two high-velocity tin ejecta microjets as captured through sequences of x-ray radiography images from experiments on the OMEGA EP laser.

Figure 1(a) shows a schematic of the ejecta platform. The targets consist of two tin foils with an angle of 130° between target normals. The foils have grooves carved into their interior surfaces, which traverse the entire foils and are 45 μm deep with 60° opening angles. Figure 1(b) shows a photo of the assembled targets. The tin foils are 100 μm thick with 30-μm-thick plastic ablators on their front surfaces to increase laser drive efficiency. They are irradiated with two 8-ns square laser pulses with tunable energy, driving shock waves into the tin. Figure 1(c) shows pressure profiles from radiation-hydrodynamic simulations performed using Ares[5] at three different times for the sample case of a 11.7-GPa shock. After a delay, a 500-J, 100-ps short-pulse laser heats a 20-μm titanium microwire as a bright x-ray point source to image along the axis perpendicular to the flow of both planar microjets with a resolution of 20 μm. Figures 1(d) and 1(e) show analyzed radiographs of interacting jets from targets with laser drives of 70 J and 1200 J, producing shock pressures of 11.7 GPa and 116 GPa, respectively. We observe densities up to 30 and 150 mg/cm^3 for the two cases. The density relates linearly to the packing density (or "volume fraction") of particles within the jetting material. From our analysis, the volume fractions in the microjets reach up to 0.3% for the lower-pressure drive and 1.5% for the higher-pressure drive. Analysis of the lower-pressure jets shows that the jets pass through each other unattenuated, maintaining the same velocity and density distributions. In comparison, the higher-pressure jets generate a cloud of material upon interaction, suggesting a higher probability of particle collisions.

Simulations of the jetting tin identified three different regimes: a low-energy regime where material strength inhibits jet formation, a moderate-energy regime where the tin is a mixed solid–liquid material, and a high-energy regime where the tin is expected to be fully melted.[6] The 11.7-GPa and 116-GPa cases are in the moderate- and high-energy regimes, respectively. Simulations of two interacting microjets for a 11.7-GPa shock exhibit the same unattenuated behavior that is observed in the experiments. Figure 2 shows simulated jet interactions from 116-GPa shocks. We characterize the spread of the interaction cloud for both the simulations and the data in the *R*- and the *S*-directions indicated in Fig. 2(a). The spread along *R* [Fig. 2(b)] corresponds with the extent of the cloud from the center of the interaction point in the direction of jet propagation and assesses how much the jet slows in its original direction of propagation. The spread in the *S* direction [Fig. 2(c)] quantifies the vertical extent of the projection onto the center axis of symmetry. Both are defined as the widths between a volume fraction cutoff of 0.1%. The hypothetical linear extents for unattenuated jets are depicted with dashed orange lines. The simulation captures the observed slowing from

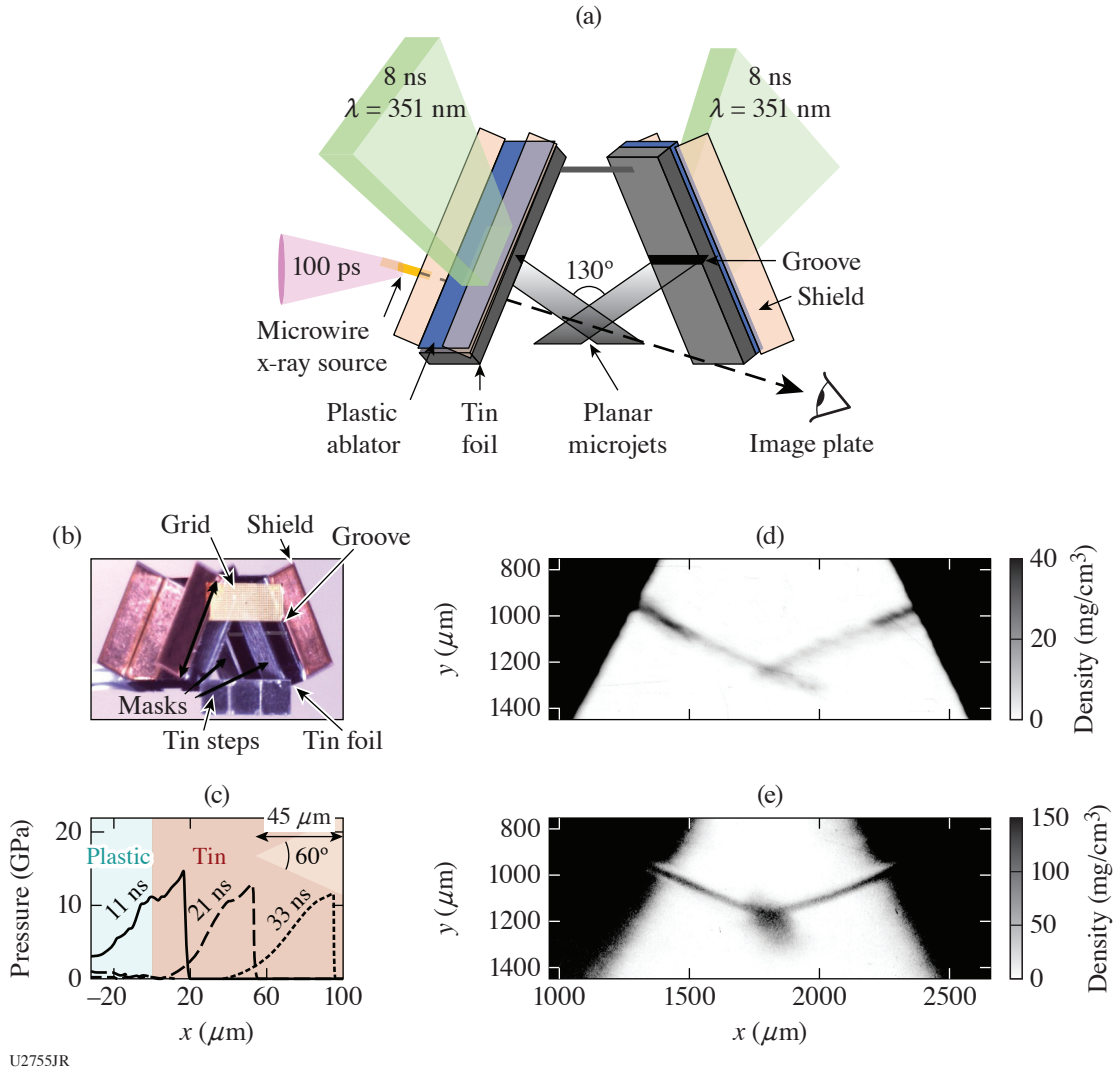

Figure 1

(a) Schematic of the tin microjet interaction platform. Two long-pulse lasers drive shocks into tin foils with grooves carved into their rear surfaces. A short-pulse laser on a microwire generates x rays for radiography. (b) Photo of the target indicating key elements and dimensions. Tin steps of known thicknesses are used for density calibration in radiographs. Masks limit the jet region that propagates to the interaction point. (c) Simulated spatial variations of pressure at three times. Groove schematic is overlaid on simulation results. [(d),(e)] Two analyzed radiographs from drive pressures of 11.7 and 116.0 GPa, respectively. The higher-pressure drive results in densities that are 5× higher than the lower-pressure case.

6.5 km/s to 4.5 km/s after interaction in Fig. 2(b); the collisions between particles result in altered mass-velocity distributions of the particles such that the particles travel in many directions, generating a cloud. Figure 2(c), however, shows that the observed vertical extent of the cloud exceeds the predicted value. Lineouts of the spread in both the *R* and *S* directions for the data and simulations show similar qualitative characteristics, with higher-density regions at the center of interaction followed by densities tapering with increased distance from the center. However, the simulations show up-to 30% higher density at the center point of interaction, again suggesting that the simulations do not capture the full spread behavior.

More experiments are needed to understand both the collision model deficiencies and the onset of interaction behavior as a function of shock pressure, but these experiments provide the first data on interacting ejecta microjet behavior and a novel methodology to observe the interactions of high-velocity, particle-laden flows, which opens many more avenues for detailed study.

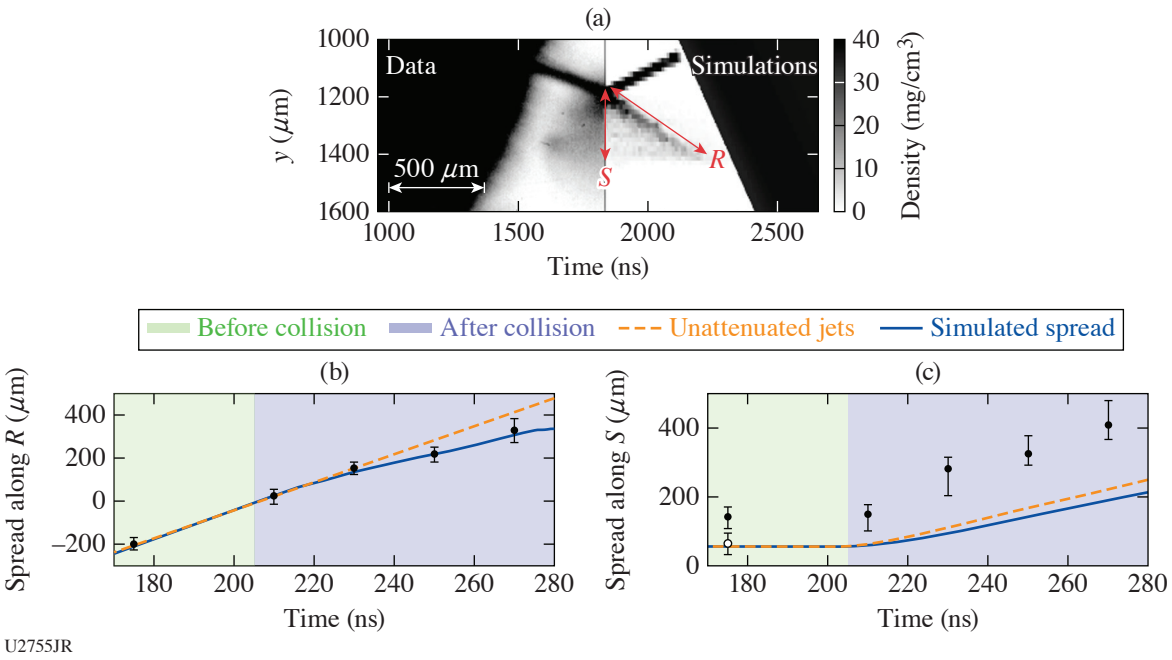

Figure 2
High-pressure shock data and simulations for particle spread. (a) Density maps for the data (left) and simulations (right). Spread as measured along the *R* and *S* directions is indicated. (b) The spread of the microjet cloud in the direction of jet propagation as measured from the center point of the interaction (*R* direction): simulations (blue line), experiments (black points). (c) The projection of jet extent onto the axis of symmetry (*S* direction). The points before collision indicate the vertical extent of a single jet: the bulk of the jet (white) and the small bulbous region near the front of the jet (black). The orange lines indicate the hypothetical linear extent of unattenuated jets.

This material is based upon work supported by the Department of Energy National Nuclear Security Administration under Award Number DE-NA0003856, the University of Rochester, and the New York State Energy Research and Development Authority.

1. M. Lambrechts and A. Johansen, Astron. Astrophys. **544**, A32 (2012).
2. Z. Warhaft, Fluid Dyn. Res. **41**, 011201 (2008).
3. K. O. Mikaelian, Phys. Rev. Lett. **80**, 508 (1998).
4. D. S. Sorenson *et al.*, J. Appl. Phys. **92**, 5830 (2002).
5. R. M. Darlington, T. L. McAbee, and G. Rodrigue, Comp. Phys. Commun. **135**, 58 (2001).
6. K. K. Mackay *et al.*, J. Appl. Phys. **128**, 215904 (2020).

Optical Shock-Enhanced Self-Photon Acceleration

P. Franke,[1,2] D. Ramsey,[1,2] T. T. Simpson,[1,2] D. Turnbull,[1] D. H. Froula,[1,2] and J. P. Palastro[1,3,4]

[1]Laboratory for Laser Energetics, University of Rochester
[2]Department of Physics and Astronomy, University of Rochester
[3]Department of Mechanical Engineering, University of Rochester
[4]Institute of Optics, University of Rochester

Photon accelerators can spectrally broaden laser pulses with high efficiency in moving electron density gradients driven in a rapidly ionizing plasma. When driven by a conventional laser pulse, the group-velocity walk-off experienced by the accelerated photons and deterioration of the gradient from diffraction and plasma-refraction limit the extent of spectral broadening. Here we show that a laser pulse with a shaped space–time and transverse intensity profile overcomes these limitations by creating a guiding density profile at a tunable velocity. Self-photon acceleration in this profile leads to dramatic spectral broadening and intensity steepening, forming an optical shock that further enhances the rate of spectral broadening. In this new regime, multi-octave spectra extending from 400-nm to 60-nm wavelengths, which support near-transform-limited <400-as pulses, are generated over <100 μm of interaction length.

Broadband sources of coherent radiation find utility across diverse scientific disciplines as experimental drivers and diagnostic tools. State-of-the-art supercontinuum sources, which primarily achieve spectral broadening through Kerr-induced self-phase modulation of ultrashort laser pulses in either gas-filled fibers[1] or self-guided filaments,[2] routinely generate multi-octave spectra in the infrared (IR) to ultraviolet (UV) wavelength range (15 μm to 100 nm).[3–7] Such sources have thus far been limited to wavelengths >100 nm, due to a lack of dispersion control and strong absorption in the extreme ultraviolet (XUV) (λ = 10 nm to 100 nm). Extending coherent broadband sources into the extreme ultraviolet would open new wavelength regimes for spectroscopy and increase the achievable spatial and temporal resolution for applications including single-shot spectral interferometry,[8] transient spectroscopy,[9] and coherence tomography.[10]

Photon accelerators can spectrally broaden laser pulses with high efficiency in moving electron density gradients.[11,12] When driven by a conventional laser pulse, the group velocity walk-off experienced by the accelerated photons and deterioration of the gradient from diffraction and refraction limit the extent of spectral broadening [Figs. 1(a) and 2(f)],[13–16] Here we introduce a scheme [Fig. 1(b)] that largely eliminates the adverse effects of diffraction, refraction, and dephasing by combining spatiotemporal[17–20] and transverse intensity profile shaping of the laser pulse.[21–23] This structured flying-focus (SFF) pulse drives a guiding plasma density profile that moves at a tunable focal velocity v_f. When a properly designed SFF pulse propagates in a homogeneous, partially ionized plasma, it undergoes extreme self-steepening and spectral broadening, culminating in the formation and collapse of an optical shock.

From 2-D finite-difference time-domain simulations, we discover that this novel self-shocked photon acceleration can produce multi-octave spectra extending well into the XUV (400 nm to 60 nm) over <100 μm of interaction length. The incident pulse had a central wavelength of 400 nm, a total energy of 53 μJ, and a total duration of 12 fs, values compatible with a tabletop Ti:Sa laser system. The intensity peak produced by the spatiotemporal shaping had a duration of 3.3 fs. The incident pulse was compressed considerably during the interaction, such that an isolated 700-as pulse was obtained at the accelerator output (90-μm interaction length). A simple short-pass filter can isolate even shorter 1.3× transform limited, highly focusable, coherent, high-intensity

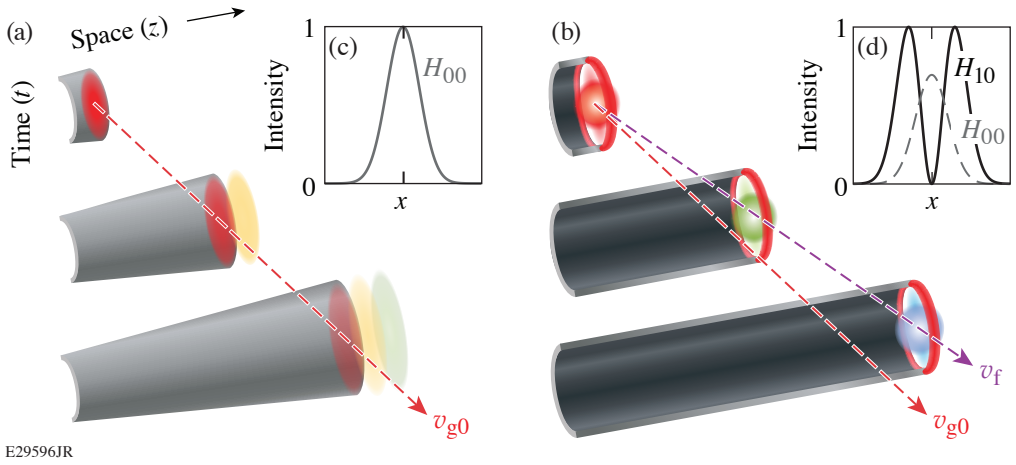

Figure 1
(a) A Gaussian beam drives a (gray) radially convex ionization front at the group velocity of light over approximately a Rayleigh length. Photons diverge from the optical axis due to diffraction and plasma refraction. Frequency upshifted photons dephase from the ionization front due to group velocity walk-off, limiting the system to relatively small frequency shifts. (b) A SFF pulse drives a concave ionization front at a tunable focal velocity $v_f \gtrsim v_{g0}$ over a distance much greater than a Rayleigh length. Photons are concentrated near the optical axis and stay in phase with the ionization front, resulting in many photons undergoing a large frequency shift. Transverse intensity profiles of a typical (c) Gaussian pulse and (d) SFF pulse used in 2-D simulations. Spatiotemporal shaping causes the intensity peak of the SFF to propagate at a tunable velocity in the far field. The guiding-transverse profile is achieved by combining orthogonally polarized Laguerre-Gaussian spatial modes.

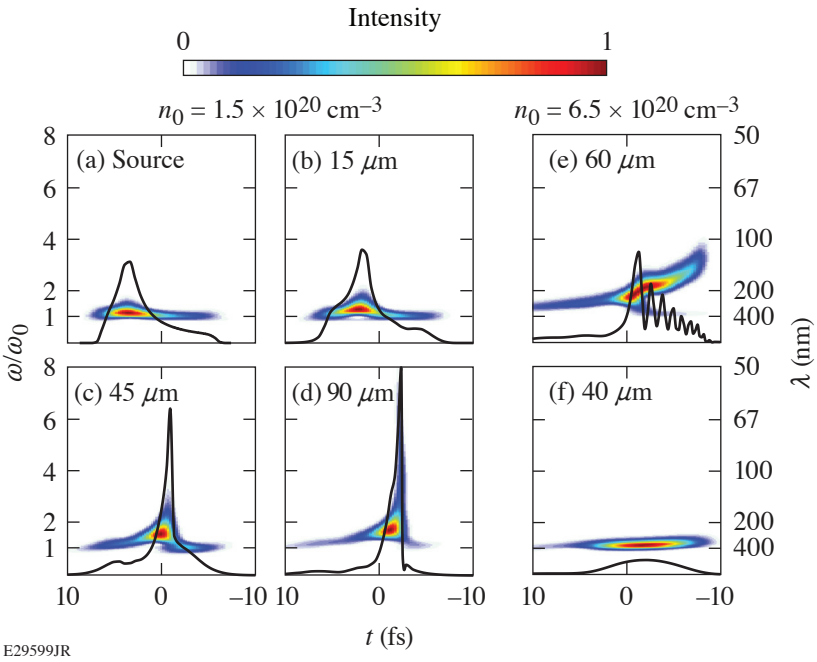

Figure 2
Spectrograms obtained by wavelet transform of the electric field on the optical axis for a SFF pulse at (a) the source input plane, (b) 15 μm, (c) 45 μm, and (d) 90 μm, with $v_f = 1.015\ v_{g0} = 0.9817\ c$, and an initial neutral density $n_0 = 1.5 \times 10^{20}$ cm^{-3}. For comparison, the spectrograms at higher density ($n_0 = 6.5 \times 10^{20}$ cm^{-3}) are shown for (e) a SFF pulse with $v_f = 1.030\ v_{g0} = 0.8740\ c$, and (f) a standard Gaussian pulse focused at $z = 10$ μm. The color scale in each plot is normalized to the peak intensity. On-axis intensity profiles (black) are normalized to 10^{17} W/cm^2.

(>10^{15}-W/cm^2), subfemtosecond pulses (350 as, 9× temporal compression) from the accelerator output without the need for post compression. Spectral filtering could be achieved by allowing the output pulse to naturally diffract out of the end of the accelerator, collimating it with an appropriate curved reflector,[24] and then allowing it to pass through a 200-nm-thick magnesium foil.[25] The filtered pulse could then be refocused on target using another curved reflector.

Spatiotemporal shaping produces a focal region much longer than a Rayleigh length and allows the peak laser intensity to move through the accelerator at a velocity $v_{g0} < v_f < c$, where v_{g0} is the initial group velocity of the pulse. Under these condi-

tions, the intensity peak moves forward within the pulse's temporal envelope, such that self-accelerated photons at the back of the pulse catch up to and remain in phase with the intensity peak formed by the unshifted photons as they come into focus. The transverse intensity profile of the pulse has higher off-axis intensity. The resulting optical field ionization creates a guiding, radial electron density gradient that dynamically forms just ahead of the central axial density gradient responsible for the photon acceleration. Accelerated photons, thus confined near the optical axis, overlap temporally and spatially with other photons of varying frequency. This local increase in bandwidth and photon density leads to dramatic self-steepening and elevated amplitude of the main intensity peak. The resulting sharpened axial gradient causes faster frequency shifting and more sharpening, which in turn causes even faster frequency shifting [Figs. 2(a)–2(d)]. Eventually, optical wave breaking terminates the self-steepening and limits the maximum extent of spectral broadening. Increasing the initial density of the target increases the group-velocity dispersion, leading to shorter wave-breaking distances and smaller maximum frequency shifts [Fig. 2(e)].

The unique combination of compact size, short wavelength, broad bandwidth, and high coherence distinguishes this approach from other currently available sources. An experimental realization would provide a novel tabletop source of coherent broadband radiation and attosecond pulses in the XUV that could eventually scale to a tabletop source of coherent soft x rays. Democratizing access to extreme light through the development of radiation sources, such as that described here, could lead to an increased rate of scientific progress across fields that have far-reaching and positive impacts in fields such as material science, biology, and clean energy.

This material is based upon work supported by the Office of Fusion Energy Sciences under Award Number DE-SC0019135, the Department of Energy National Nuclear Security Administration under Award Number DE-NA0003856, the University of Rochester, and the New York State Energy Research and Development Authority.

1. J. M. Dudley, G. Genty, and S. Coen, Rev. Mod. Phys. **78**, 1135 (2006).
2. A. Couairon and A. Mysyrowicz, Phys. Rep. **441**, 47 (2007).
3. K. Jiao *et al.*, Opt. Lett. **44**, 5545 (2019).
4. F. Belli *et al.*, Optica **2**, 292 (2015).
5. A. Ermolov *et al.*, Phys. Rev. A **92**, 033821 (2015).
6. J. C. Travers *et al.*, Nat. Photon. **13**, 547 (2019).
7. N. Aközbek *et al.*, New J. Phys. **8**, 177 (2006).
8. H. Mashiko *et al.*, Opt. Express **28**, 21025 (2020).
9. K. Ramasesha, S. R. Leone, and D. M. Neumark, Annu. Rev. Phys. Chem. **67**, 41 (2016).
10. F. Wiesner *et al.*, Optica **8**, 230 (2021).
11. S. C. Wilks *et al.*, Phys. Rev. Lett. **62**, 2600 (1989).
12. J. T. Mendonça, *Theory of Photon Acceleration*, Series in Plasma Physics (Institute of Physics Publishing, Bristol, England, 2001).
13. J. M. Dias *et al.*, Phys. Rev. E **66**, 056406 (2002).
14. N. C. Lopes *et al.*, Europhys. Lett. **66**, 371 (2004).
15. J. M. Dias *et al.*, Phys. Rev. Lett. **78**, 4773 (1997).
16. A. Howard *et al.*, Phys. Rev. Lett. **123**, 124801 (2019).
17. D. H. Froula *et al.*, Nat. Photonics **12**, 262 (2018).
18. A. Sainte-Marie, O. Gobert, and F. Quéré, Optica **4**, 1298 (2017).
19. J. P. Palastro *et al.*, Phys. Rev. Lett. **124**, 134802 (2020).
20. T. T. Simpson *et al.*, Opt. Express **28**, 38516 (2020).
21. M. W. Beijersbergen *et al.*, Opt. Commun. **112**, 321 (1994).
22. Y. Shen *et al.*, Light Sci. Appl. **8**, 90 (2019).
23. A. Longman *et al.*, Opt. Lett. **45**, 2187 (2020).
24. C. Bourassin-Bouchet *et al.*, Opt. Express **21**, 2506 (2013).
25. G. D. Tsakiris *et al.*, New J. Phys. **8**, 19 (2006).

Nonlinear Thomson Scattering of Spatiotemporally Shaped Laser Pulses

D. Ramsey,[1] B. Malaca,[2] A. Di Piazza,[3] M. Formanek,[3] P. Franke,[1] D. H. Froula,[1] M. Pardal,[2] T. T. Simpson,[1] J. Vieira,[2] K. Weichman,[1] and J. P. Palastro[1]

[1]Laboratory for Laser Energetics, University of Rochester
[2]Instituto de Plasmas e Fusão Nuclear-Laboratório Associado, Portugal
[3]Max-Planck-Institut für Kernphysik, Germany

Bright sources of high-energy photons lead to advancements in a range of disciplines including ultrafast biology and material science, nonlinear quantum electrodynamics, nuclear spectroscopy, and radiotherapy. The brightest sources currently reside at large accelerator facilities in the form of x-ray free-electron lasers or synchrotrons. While laser-driven sources promise a smaller-scale, widely accessible alternative, challenges in achieving the required photon number, energy, and coherence have held these sources back. Of the potential candidate laser-driven schemes, nonlinear Thomson scattering (NLTS) can produce extremely high energy, collimated radiation in a relatively controlled setting. NLTS, however, has inherent constraints that currently impede its realization as a practical light source.

In NLTS a relativistic electron collides with a laser pulse traveling in the opposite direction [Fig. 1(a)]. The electron rapidly oscillates in the fields of the pulse, reflecting and reradiating the incident photons. The properties of the radiation depend on the laser intensities and frequency of the pulse and the initial electron energy. Maximizing the radiated power requires large laser intensities. In these strong fields, the ponderomotive force of the pulse appreciably decelerates the electron and increases the amplitude of its oscillations along the direction of its initial motion. This red shifts the emitted frequencies and widens the emission angle.[1] The trade-off between the power, spectrum, and emission angle constrains the utility of NLTS.

Spatiotemporal pulse shaping provides control over the ponderomotive force, which can compensate for the ponderomotive deceleration in NLTS. As an example, the chromatic aberration from a diffractive optic and a chirp can be used to control the location and time at which each temporal slice within a pulse comes to its focus, respectively. By adjusting the chirp the resulting intensity peak, and therefore the ponderomotive force, can travel at any velocity with respect to the phase fronts (forward or backward) over distances much longer than a Rayleigh range.[2] Aside from extending the interaction length, a ponderomotive force that counter-propagates with respect to the phase fronts can *accelerate* an electron in NLTS.[3]

Here we describe novel regimes of nonlinear Thomson scattering that exploit the ponderomotive control afforded by spatiotemporal pulse shaping to substantially enhance the scaling of power, emission angle, and frequency with laser intensity. For high-intensity pulses, these regimes exhibit orders-of-magnitude-higher radiated powers and smaller emission angles than conventional NLTS. Further, the improved scaling with laser intensity allows for lower electron energies, relaxing the requirements on the electron accelerator.

Figure 1 contrasts backscattering configurations for conventional NLTS and NLTS with ponderomotive control (NPC). Conventional NLTS employs a standard laser pulse with an intensity peak and phase that counter-propagate at the vacuum speed of light with respect to a relativistic electron. NPC employs a spatiotemporally shaped pulse with an intensity peak that counter-propagates with respect to its phase fronts and co-propagates with respect to the electron. In both cases, as the electron enters the leading edge of the intensity peak, it begins oscillating in the polarization (transverse) and propagation (longitudinal) directions.

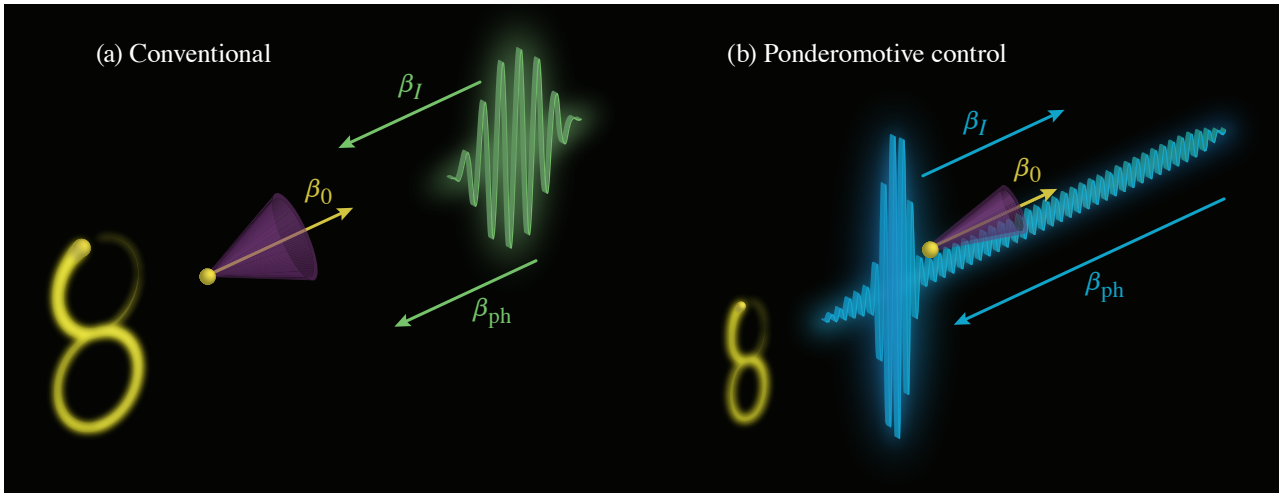

TC15637JR

Figure 1
(a) A conventional NLTS configuration in which the intensity peak and phase fronts of a laser pulse travel in the opposite direction of the electron. At the rising edge of the intensity peak, the ponderomotive force decelerates the electron, red shifting the emitted frequencies and widening their emission angle (purple cone). (b) NLTS with ponderomotive control aligns the velocities of the intensity peak and the electron. Here the ponderomotive force of the intensity peak increases or maintains the electron velocity, allowing for higher-frequency emission into a smaller angle. The electron trajectory in its average rest frame (figure-eight motion) is depicted to the left of each case.

In NPC as the co-propagating intensity peak begins to overtake the initially slower moving electron, the electron is ponderomotively *accelerated* by the co-traveling intensity peak of the pulse—in the direction opposite to the phase velocity. The electron momentum increases as the electron enters regions of higher intensity. The acceleration enhances the overall radiation properties: emitted frequencies are now blue shifted and the radiation cone narrows. Ultimately, NPC switches the burden of accelerating electrons from an external source to the laser pulse itself—a situation ideal for existing and emerging high-energy, high-power laser facilities. Nonlinear Thomson scattering with ponderomotive control can produce extremely high energy photons with a spectrum that can be tuned through the initial electron energy, the laser amplitude, and, now, the ponderomotive velocity. The added flexibility enabled by ponderomotive control eliminates the tradeoffs inherent to conventional NLTS.

This material is based upon work supported by the Office of Fusion Energy Sciences under Award Number DE-SC0019135 and DE-SC00215057, the Department of Energy National Nuclear Security Administration under Award Number DE-NA0003856, the University of Rochester, and the New York State Energy Research and Development Authority.

1. E. Esarey, S. K. Ride, and P. Sprangle, Phys. Rev. E **48**, 3003 (1993).
2. D. H. Froula *et al.*, Nat. Photonics **12**, 262 (2018).
3. D. Ramsey *et al.*, Phys. Rev. E **102**, 043207 (2020).

Kinetic Simulation Study of Magnetized Collisionless Shock Formation on a Terawatt Laser System

Y. Zhang,[1,2] J. R. Davies,[1,2] P. V. Heuer,[1] and C. Ren[1,2,3]

[1]Laboratory for Laser Energetics, University of Rochester
[2]Department of Mechanical Engineering, University of Rochester
[3]Department of Physics and Astronomy, University of Rochester

In the cosmos, magnetized collisionless shocks such as termination shocks and bow shocks are ubiquitous. These shocks are usually magnetized by astronomical objects and are believed to be an important source of nonthermal particles in the universe. High-power laser systems are capable of reproducing these conditions in the laboratory and enable the systematic study of the underlying physics. It is well known that collisionality is very low due to low plasma density in space; collisions therefore cannot provide efficient dissipation for the shock. A modified two-stream instability (MTSI) has been proposed as the main dissipation mechanism for (quasi-) perpendicular collisionless shocks.[1,2] Previous kinetic particle-in-cell (PIC) simulations used reduced ion–electron mass ratio, an unrealistic high magnetic field, or reduced speed of light to save computational resources; these concessions may alter the relative importance of different physical processes. In this summary our simulations use realistic and experimentally accessible parameters to capture true physics and provide a direct reference for experiments.

In the experimental setup shown in Fig. 1(a), a laser-driven solid-density piston is launched to drive a collisionless shock in a premagnetized ambient hydrogen or neon plasma. The external magnetic field is applied by MIFEDS (magneto-inertial fusion electrical discharge system).[3] In the simulations, as seen in Fig. 1(b), the piston is idealized by a fixed reflecting wall on the right boundary. The ambient plasma drifts toward the wall, which leads to a clear shock downstream free of the influence from the piston. This drifing velocity V_d in the simulation frame is identical to the piston velocity V_p in the lab frame.

To create a collisionless shock the ion collisional mean free path between piston ions and ambient ions must be much larger than the shock width L, and the piston velocity must be supermagnetosonic. These two conditions constrain the ambient plasma density,

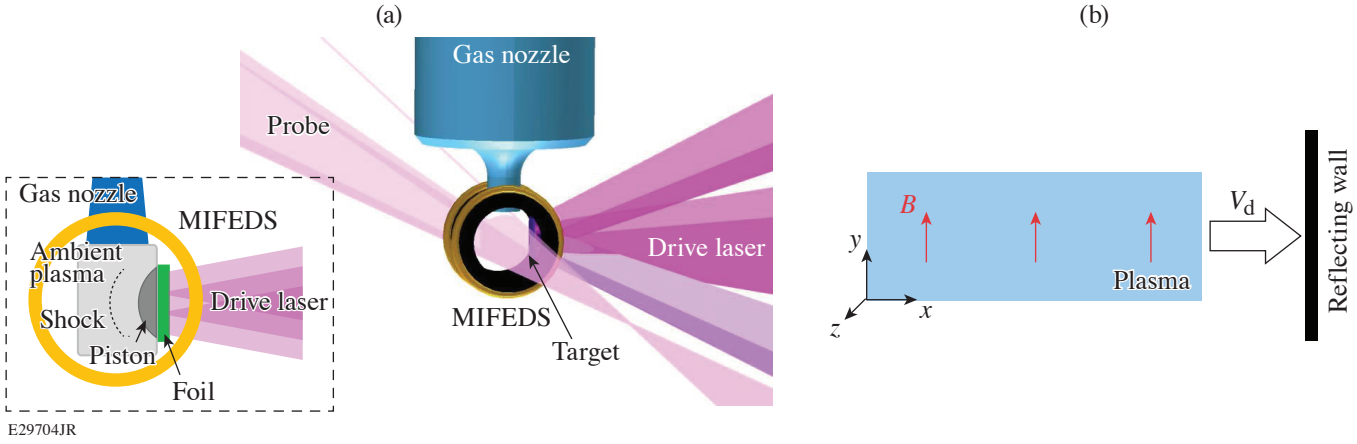

Figure 1
(a) Experimental setup and top-down schematic; (b) reflecting wall simulation setup.

$$\frac{27Z_{\mathrm{i}}\left(\dfrac{B_{\mathrm{l}}^{T}}{50}\right)^{2}}{56\dfrac{m_{\mathrm{i}}}{m_{\mathrm{H}}}\left(\dfrac{V_{\mathrm{p}}^{\mathrm{km/s}}}{500}\right)^{2}-Z_{\mathrm{i}}\dfrac{T_{\mathrm{e1}}^{\mathrm{eV}}}{50}-\dfrac{T_{\mathrm{i1}}^{\mathrm{eV}}}{50}}<n_{\mathrm{e1}}^{10^{19}\,\mathrm{cm}^{-3}}\ll\frac{131}{\ln\Lambda}\left(\frac{m_{\mathrm{i}}}{m_{\mathrm{H}}}\right)^{2}\frac{1}{Z_{\mathrm{i}}^{3}}\left(\frac{L^{\mu\mathrm{m}}}{100}\right)^{-1}\left(\frac{V_{\mathrm{p}}^{\mathrm{km/s}}}{500}\right)^{4}, \tag{1}$$

where m, n, Z are the particle mass, density, charge number, respectively; B is the magnetic field; V_{p} is the piston velocity; subscripts i, H, and e denote ion, proton, and electron, respectively; 1 (2) represents the upstream (downstream) direction; and the superscripts indicate the units of the parameters.

The growth of MTSI has been used to find suitable parameter space for OMEGA EP[4] experiments. The dispersion relation of MTSI is written as[5]

$$1+\frac{\omega_{\mathrm{pe}}^{2}}{k^{2}v_{\mathrm{the}}^{2}}\left[1-\exp\left(-\lambda_{\mathrm{e}}\right)\sum_{m=-\infty}^{\infty}I_{\mathrm{m}}\left(\lambda_{\mathrm{e}}\right)\frac{\omega}{\omega+m\Omega_{\mathrm{ce}}}\right]-\sum_{s=\mathrm{in,re}}\frac{\omega_{\mathrm{ps}}^{2}}{2k^{2}v_{\mathrm{the}}^{2}}Z'\left(\xi_{\mathrm{s}}\right)=0, \tag{2}$$

where ω_{ps} is the plasma frequency for species s (e for electrons, in for incoming ions, and re for reflected ions), $v_{\mathrm{ths}}=(T_{\mathrm{s}}/m_{\mathrm{s}})^{1/2}$ is the thermal velocity, Ω_{cs} is the gyrofrequency, k is the mode number, $\lambda_{\mathrm{e}}=k^{2}v_{\mathrm{the}}^{2}/\Omega_{\mathrm{ce}}^{2}$, I_{m} is the modified Bessel function of the first kind, Z is the plasma dispersion function, and $\xi_{\mathrm{s}}=(\omega-kV_{\mathrm{xs}})/\sqrt{2}kv_{\mathrm{ths}}$, where v_{xs} is the bulk velocity of the two ion species. Equation (2) can be solved numerically for $\omega=\omega_{\mathrm{r}}+i\omega_{\mathrm{i}}$, from which the maximum growth rate $\gamma_{\mathrm{MTSI}}=[\omega_{\mathrm{i}}]_{\mathrm{max}}$, and the corresponding, most-unstable mode k_{MTSI}, and wavelength $\lambda_{\mathrm{MTSI}}\equiv 2\pi/k_{\mathrm{MTSI}}$ can be found. Under zero-current condition and the assumptions $n_{\mathrm{in}}/n_{\mathrm{re}}=3$, $V_{\mathrm{in}}=V_{\mathrm{d}}/4$, $V_{\mathrm{re}}=3V_{\mathrm{d}}/4$, it is found that the maximum growth rate of MTSI is much larger than the ion gyrofrequency when $M_{\mathrm{sl}}\geq 4$ for hydrogen and $M_{\mathrm{sl}}\geq 2$ for neon, indicating a shock can be readily formed within a few tenths of an ion gyration period. Alternately, with an achievable applied magnetic field of only tens of tesla, it is possible to create a shock within a few tenths of a nanosecond. Typical parameter ranges achievable on the OMEGA EP/MIFEDS platform are given in Table I. Based on the conditions discussed in this section we chose upstream parameters listed in Table I for our PIC simulations to study shock formation in more detail. The MTSI, collisionality parameters, and some dimensionless quantities are also shown in Table I.

Hydrogen and neon shocks both form within $\sim\gamma_{\mathrm{MTSI}}^{-1}$. Figure 2 shows the hydrogen shock as an example. At $t=0.126$ ns ($\approx 0.10\ T_{\mathrm{ci1}}\approx 1.1/\gamma_{\mathrm{MTSI}}$), a shock with a compression ratio of $r\approx 2.35$ [Fig. 2(a)] is formed by the $M_{\mathrm{sp}}=3.5$ ideal piston. The presence of reflected ions [the density hump in the upstream region in Fig. 2(a) and the lower prong of the tuning fork structure in Fig. 2(b)] indicates the supercriticality of the formed shock. MTSI is induced by the interaction between the incoming ion and shock-reflected ion in the background magnetic field. Nonzero modes in the Fourier spectrum of E_x [modes 1 and 2 in Fig. 2(c)] further confirm MTSI is the operating instability, in good agreement with the solutions of the dispersion relation.

The reflected ions are accelerated in both shock normal and tangential directions by the electrostatic field and the motional electric field, respectively, to 6.6 to 9.7 keV (average ~8 keV) in the lab frame. These ions accumulate in the upstream and participate in shock-front reformation (on the time scale of a few $\Omega_{\mathrm{ci}}^{-1}$) in later times. Our results using realistic parameters substantially separate the shock-formation time from $\Omega_{\mathrm{ci}}^{-1}$ versus previous simulations using reduced $m_{\mathrm{i}}/m_{\mathrm{e}}$, showing that these shocks are formed via MTSI. Electrons are heated isotropically to $T_{\mathrm{e2}}\approx 200$ eV. Additional 1-D simulations further confirm that the shock is indeed collisionless and the reflecting wall is a good approximation of a realistic piston. The formed shocks are also well described by Rankine–Hugoniot jump conditions.

This material is based upon work supported by the Department of Energy National Nuclear Security Administration under Award No. DE-NA0003856, Department of Energy Award No. DE-SC0020431, and the resources of the National Energy Research Scientific Computing Center (NERSC), a U.S. Department of Energy Office of Science User Facility located at Lawrence Berkeley National Laboratory. The authors thank the UCLA-IST OSIRIS consortium for the use of OSIRIS.

Table I: Parameters for the OMEGA EP/MIFEDS platform and the hydrogen/neon simulations, with corresponding MTSI growth rate/mode number of the most-unstable mode and some key dimensionless quantities. The plasma beta is $\beta = 2\mu_0(n_i T_i + n_e T_e)/B^2$, $\tau = \omega_{pe}^2/\Omega_{ce}^2$ is the magnetization parameter. The piston velocity range is from *HYDRA*[6] simulations of the proposed experimental setup.

		OMEGA EP/MIFEDS	Hydrogen	Neon (Ne^{8+})
Upstream				
Density	n_{e1}	10^{18} to 10^{20} cm^{-3}	10^{19} cm^{-3}	6×10^{18} cm^{-3}
Temperature	T_1	40 to 400 eV	50 eV	160 eV
B field	B_1	≤50 T	50 T	50 T
Piston velocity	V_p	≤500 km/s	442 km/s	375 km/s
Ion gyroradius	ρ_{i1}		92.3 μm	195.7 μm
Ion gyroperiod	T_{ci1}		1.3 ns	3.3 ns
MTSI				
Maximum growth rate	γ_{MTSI}		8.8 ns^{-1}	6.7 ns^{-1}
Most-unstable mode	λ_{MTSI}		10.7 μm	14.2 μm
Dimensionless				
Piston sonic Mach number	M_{sp}		3.50	3.50
Alfvénic Mach number	M_{Ap}		1.28	1.33
Magnetosonic Mach number	M_{msp}		1.20	1.25
Ion mean free path	$\lambda_{ii}/\lambda_{MTSI}$		74	40
MTSI growth rate	$\gamma_{MTSI}/\Omega_{ci1}$		11.5	21.9
Plasma beta	β_1		0.16	0.17
Magnetization	τ_1		421	247

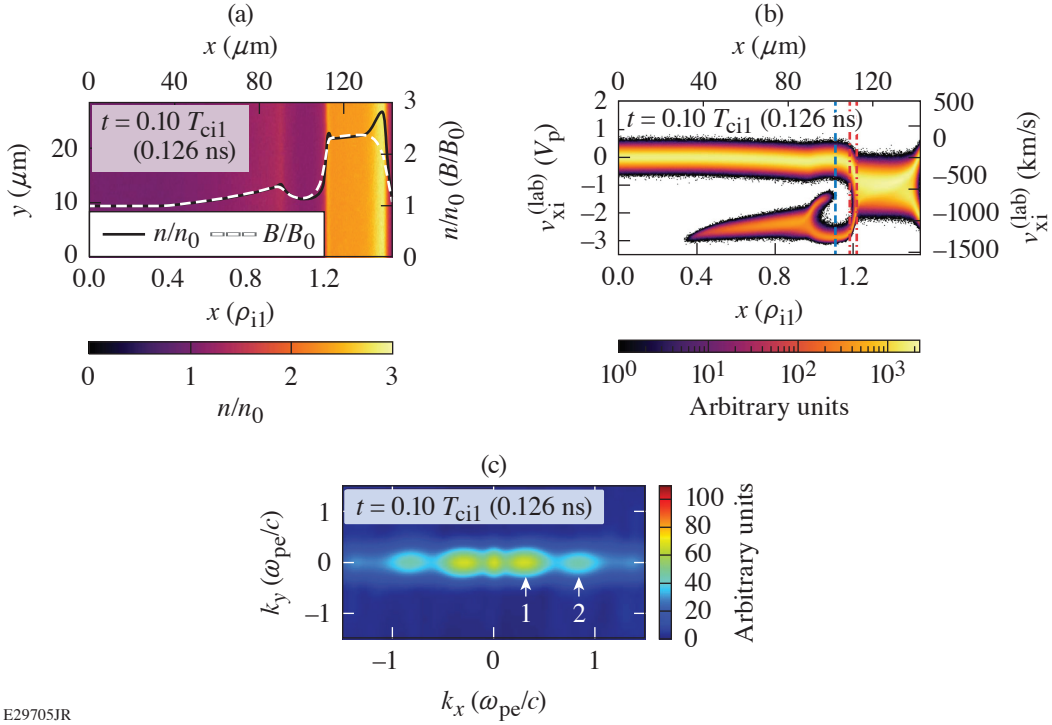

Figure 2
(a) Hydrogen ion density (2-D and y averaged) and magnetic field (y averaged) at $t = 0.10\ T_{ci1}$; (b) Ion v_{xi}–x phase space in the lab frame; (c) Fourier spectrum of E_x. The modes labeled with 1 and 2 are $k_x \approx 0.33$ and $0.86\ \omega_{pe}/c$, respectively.

1. J. Park *et al*., Phys. Plasmas **19**, 062904 (2012).
2. J. Park *et al*., Astrophys. J. **765**, 147 (2013).
3. D. H. Barnak *et al*., Rev. Sci. Instrum. **89**, 033501 (2018).
4. D. N. Maywar *et al*., J. Phys.: Conf. Ser. **112**, 032007 (2008).
5. S. P. Gary, *Theory of Space Plasma Microinstabilities*, Cambridge Atmospheric and Space Science Series (Cambridge University Press, Cambridge, 1993).
6. M. M. Marinak *et al*., Phys. Plasmas **8**, 2275 (2001).

Relativistically Transparent Magnetic Filaments: Scaling Laws, Initial Results, and Prospects for Strong-Field Quantum Electrodynamics Studies

H. G. Rinderknecht,[1] T. Wang,[2] A. Laso Garcia,[3] G. Bruhaug,[1] M. S. Wei,[1] H. J. Quevedo,[4] T. Ditmire,[4] J. Williams,[5] A. Haid,[5] D. Doria,[6] K. M. Spohr,[6] T. Toncian,[3] and A. Arefiev[2]

[1]Laboratory for Laser Energetics, University of Rochester
[2]University of California, San Diego
[3]Helmholtz-Zentrum Dresden-Rossendorf, Germany
[4]University of Texas, Austin
[5]General Atomics, San Diego
[6]ELI-NP & IFIN-HH, Bucharest-Magurele, Romania

Relativistic electron motion and volumetric laser–plasma interaction at supercritical densities create a novel phenomenon: the relativistically transparent magnetic filament. A sufficiently intense laser in an overdense plasma induces a relativistic current filament that moves axially with the laser field. This current generates a quasi-static azimuthal magnetic field with strength comparable to the laser field. Surrounding the filament with a higher-density channel wall optically guides the laser pulse, allowing intense laser–plasma interaction over many Rayleigh lengths. This system operates as a relativistic plasma rectifier for laser light that efficiently converts the laser's electric and magnetic fields into a direct filamentary current and associated magnetic field. Electrons oscillate within the confining azimuthal magnetic field, facilitating direct energy gain from the laser and acceleration to hundreds of MeV. At the same time, the electron deflections within the magnetic field cause them to emit photons. Simulations predict that the azimuthal field strength reaches the megatesla level and the effective acceleration gradient exceeds 10^5 MeV/cm in the multipetawatt regime. The extreme magnetic-field strength and electron energy boost the radiated photon energy and the radiative power such that the magnetic filaments become efficient radiators of MeV photons.

We derived analytical scaling laws for the radiative properties of the magnetic filament phenomenon in terms of four parameters: the normalized laser amplitude $a_0 = |e|\,E/m\omega c$, a relativistic transparency parameter $S_\alpha \equiv n_e/n_e\,a_0$ with electron density n_e and critical plasma density n_c, the normalized laser focal radius $R_\lambda = (R/\lambda)$, and the normalized laser pulse duration $\tau_\nu = c\tau/\lambda$. To derive these laws, we made the following assumptions: First, the electrons are represented by a thermal distribution, with the number of accelerated electrons $N_e = n_e \pi R^2 c\tau$. Second, the characteristic temperature of the electron distribution scales linearly with time and can be represented as $T(t) = C_T\,a_0\,mc^2\,(ct/\lambda)$ for a constant of acceleration C_T. Third, the azimuthal magnetic field is produced by a relativistic, uniform current density as $B(r) = B_0\,\pi(r/\lambda)S_\alpha$ for the laser's magnetic-field amplitude B_0. Fourth, the radiation power per electron is given by the synchrotron power spectrum and is evaluated using $B(r)$ at either the laser radius or a magnetic boundary $r_{mb} = \lambda f_i^{1/2} S_\alpha^{-1/2} \pi^{-1}$, which is a maximum radius that electrons can reach with a given initial momentum $\gamma_i \equiv f_i a_0$ for a constant f_i of order unity.[1] Fifth, the electrons radiate during a fraction of their orbit f_r. Lastly, the interaction ends by depletion of the laser pulse at a time $t_{cut} = f_t t_{max}$ for a constant factor f_t in the range (0, 1) and t_{max} represents the time at which the energy in the electron population equals the initial laser energy. These assumptions result in scaling laws for photon energy $\langle \varepsilon^* \rangle$, total radiated energy $E_{\gamma,tot}$, number of photons N_γ, and efficiency η_γ as shown in Table I.

The scaling laws were compared to the results of 3-D particle-in-cell (PIC) simulations, as shown in Fig. 1. The PIC simulations used laser amplitude $a_0 = 190$ (intensity 5×10^{22} W/cm^2), $S_\alpha = 0.105$ ($n_e = 20\,n_c$), $\tau = 35$ fs, and focal radius $R = 0.65$, 0.95, 1.35, 1.6, and 2.1 μm (Ref. 2). The acceleration constant C_T was inferred to have a value of approximately 0.08 from simulated

Table I: Scaling laws for relativistically transparent magnetic filaments.

Limit	$R < r_{mb}$	$R > r_{mb}$
$\langle \varepsilon_* \rangle / mc^2$	$\approx 1.4 \times 10^{-5} f_t a_0^2 R_\lambda \lambda_{\mu m}^{-1}$	$\approx 4.4 \times 10^{-7} f_i^{1/2} f_t^2 a_0^3 S_\alpha^{-3/2} \lambda_{\mu m}^{-1}$
$\frac{E_{\gamma,tot}}{mc^2}$	$\approx 7.7 \times 10^2 f_t^3 f_r C_T^{-1} a_0^5 R_\lambda^4 \tau_\nu$	$\approx 7.8 \times 10^1 f_i f_t^3 f_r C_T^{-1} a_0^5 S_\alpha^{-1} R_\lambda^2 \tau_\nu$
N_γ	$\approx 5.6 \times 10^8 f_t f_r C_T^{-1} a_0^2 S_\alpha R_\lambda^3 \tau_\nu \lambda_{\mu m}$	$\approx 1.8 \times 10^8 f_i^{1/2} f_t f_r C_T^{-1} a_0^2 S_\alpha^{1/2}$
η_γ	$\approx 2.9 \times 10^{-7} f_t^3 f_r C_T^{-1} a_0^3 R_\lambda^2 \lambda_{\mu m}^{-1}$	$\approx 2.9 \times 10^{-8} f_i f_t^3 f_r C_T^{-1} a_0^3 S_\alpha^{-1} \lambda_{\mu m}^{-1}$

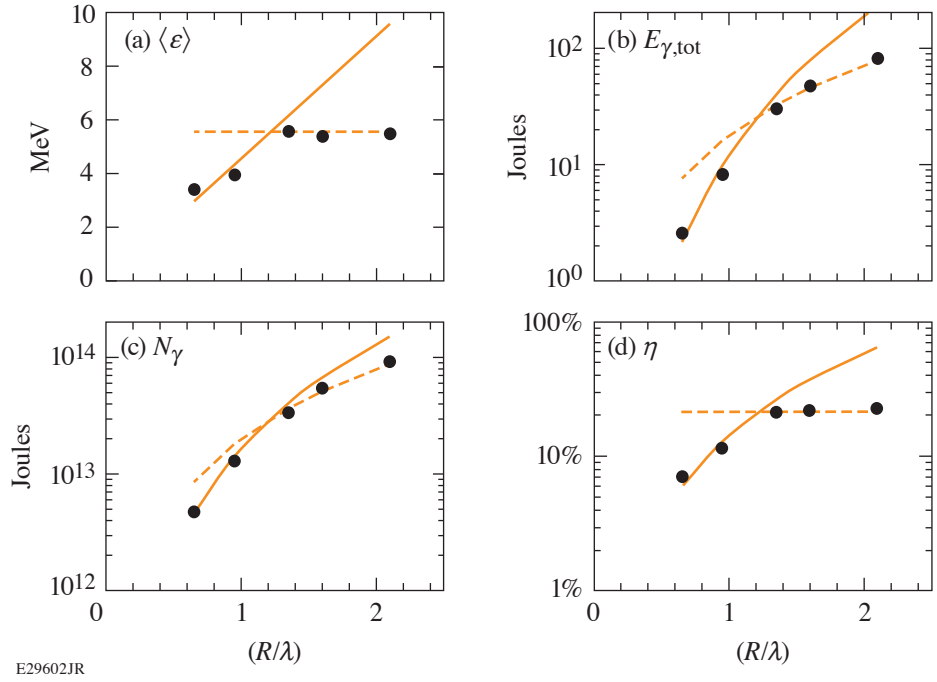

Figure 1
Comparison of derived scaling laws in the limit $R < r_{mb}$ (solid line) and $R > r_{mb}$ (dashed line) with 3-D PIC simulations in Ref. 2 (circles). (a) Characteristic photon energy, (b) total radiated energy, (c) total number of photons, and (d) radiation efficiency. Simulation results are for photons with energy above 1 MeV. Model coefficients are $f_i = 1.53$, $f_t = 0.31$, $f_r = 0.19$, and $C_T = 0.08$.

electron spectra; this value was used without loss of generality as the laws depend only on the composite constant (f_r/C_T). The scaling laws agree with the 3-D PIC simulations with reasonable values for the constants $f_i = 1.53$, $f_t = 0.31$, and $f_r = 19\%$.

Initial experiments were performed on the Texas Petawatt Laser to study this phenomenon. A peak intensity of 1.1×10^{21} W/cm^2 ($a_0 = 29.9$) was focused onto arrays of microchannels laser drilled in Kapton with a 6-μm inner diameter and filled with low-density CH foam with a density of 15 and 30 mg/cm^3 (5 and 10 n_c, respectively). Elevated electron temperatures were observed in two of eight shots with good laser–target alignment, in agreement with predictions from 3-D PIC simulations of laser–channel interaction, as shown in Fig. 2. This fraction is consistent with the likelihood of laser–channel interaction, given the

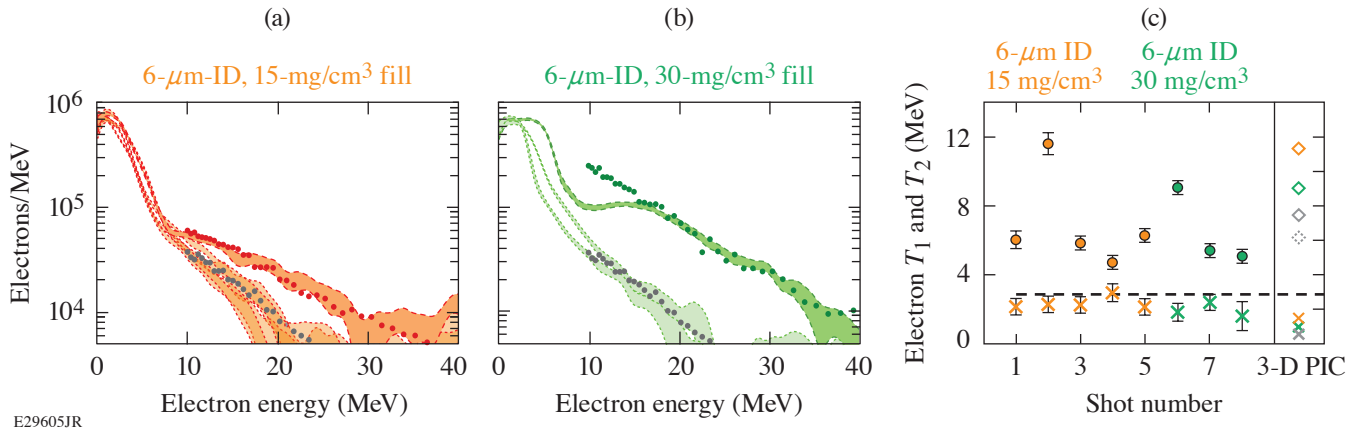

Figure 2
[(a),(b)] Electron spectra recorded on TPW experiments (curves) and from 3-D PIC simulations (circles). (c) Inferred electron temperatures on shots (circles) and from 3-D PIC simulations (diamonds). Channels with 5-n_c fill (orange), with 10-n_c fill (green), and planar 200-n_c target (gray).

pointing stability of 5-μm rms. We infer that the predicted magnetic filament phenomenon was observed in these experiments. The scaling laws will be used to design optimal targets for future experiments. At 10-PW laser facilities, efficiency approaching 50% is predicted for MeV photons.

This material is based upon work supported by the Department of Energy National Nuclear Security Administration under Award Number DE-NA0003856, the University of Rochester, and the New York State Energy Research and Development Authority.

1. Z. Gong *et al.*, Phys. Rev. E **102**, 013206 (2020).
2. T. Wang *et al.*, Phys. Rev. Applied **13**, 054024 (2020).

Ramp-Compressed Sodium at 480 GPa: A Dense Plasma Electride

D. N. Polsin

Laboratory for Laser Energetics, University of Rochester

The limiting high-pressure behavior of matter suggests that some materials transform into simple dense-packed structures with free-electron metallic behavior; examples include the ultradense solids of planetary cores and the hot plasmas of thermonuclear reactions and stellar interiors. This model breaks down at significant compressions where valence–valence and valence–core electron overlap are responsible for the chemical and electronic properties, bringing quantum behavior to the macroscale and giving rise to exotic phases such as high-temperature superconductors, quantum Hall insulators, and electrides. Sodium is the ideal material to explore such behavior due to its remarkable transformation at just 200 GPa from a free-electron simple metal to a structurally complex transparent electride,[1] where electrons are localized in interstitial positions due to the density-driven quantum mechanical constraints on the electronic wave functions.[2] Studies of high-temperature (>1000-K) electride behavior in the solid, liquid, and plasma phases have largely been limited to theoretical studies with no data on the kinetics of these phase transformations on nanosecond time scales.[3,4] Here we report on measurements of the structural and electronic properties of Na in an unexplored regime, where the nearest Na–Na distance approaches the 3*s* orbital radius. Lasers are used as high-pressure drivers to ramp compress Na up to 480 GPa and ~2000 K. X-ray diffraction measurements at these unprecedented pressures and temperatures reveal that the *hP4* electride phase is stable even in a dense plasma state and on nanosecond time scales. At intermediate pressures (242 to 292 GPa), new complex phases with diffraction peaks unaccounted for by the *hP4* structure are observed. The new phase is not transparent—in striking contrast to static compression studies—but a significant decrease in the conductivity is consistent with a transformation to a high-temperature electride phase. Interactions between core electrons occur in all materials at extreme densities and pressures; the formation and understanding of these novel quantum materials in their transient states are the first steps to a new generation of high-energy-density quantum matter.

Sodium's intriguing high-pressure behavior is evident upon inspection of its phase diagram shown in Fig. 1. Sodium transforms from simple cubic structures to at least seven complex, low-symmetry phases near the minimum of the melting curve (blue circles and blue curves) at 118 GPa and room temperature.[5,6] At 147 GPa, it transforms into an incommensurate host–guest structure—a complex structure consisting of two interpenetrating host and guest structures—as the melting temperature begins to increase.[7,8]

This series of high-pressure phase transformations is associated with remarkable transformations in Na's electronic properties with a transition from a mirrorlike metal at ambient pressure to a dark, nonreflecting *tI19* phase at 147 GPa to a transparent insulator at 200 GPa with a band gap of at least 1.3 eV (Refs. 1 and 9). Guided by first-principles structure searching results, the x-ray diffraction pattern from the transparent phase is a distorted double hexagonal close-packed (dhcp) *hP4* electride structure[1] that, together with the interstitial quasi-atoms form the binary Ni_2In structure, shown in Fig. 1 (structural model).

Simultaneous x-ray diffraction (XRD) and reflectivity measurements were performed on the OMEGA EP laser that ramp compressed Na to nearly 500 GPa (Ref. 10). At 409±15 GPa, the diffraction pattern has four peaks, consistent with the *hP4* phase reported in previous room-temperature static compression experiments by Ma *et al.*,[1] but at higher temperatures and under dynamic compression. We index the four lines as the *hP4* (010), (011), (012), and (110), giving lattice parameters $a = b = 2.75 \pm 0.03$ Å and $c/a = 1.35 \pm 0.02$. Compared to the ideal dhcp lattice, with $c/a = 3.27$ for hard spheres, the *hP4* structure is highly distorted and not close packed because the electride nature of this structure stabilizes a more open structure to accommodate the local-

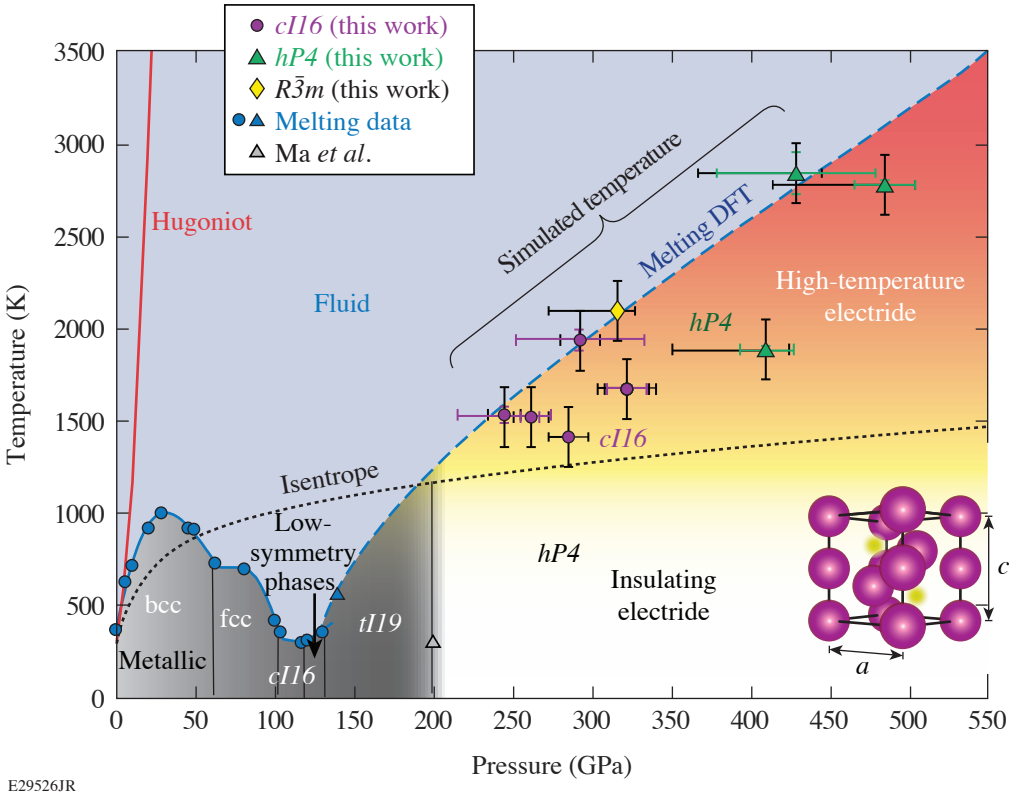

Figure 1

The high-pressure phase diagram of Na based on our laser-driven ramp compression data (purple circles, yellow diamond, and green triangles; black error bars represent systematic and random uncertainties; color "error" bars represent standard deviation in pressure and temperature states within the sample) and previous work from Refs. 1, 5, 6, 8, and 11. The data are compared to the theoretical principal Hugoniot and isentrope. The melting curve data from Refs. 6 and 8 are shown (blue circles and triangle) along with density-functional-theory (DFT) calculations[11] for the melting curve (blue dashed line) above 130 GPa in the *hP4* phase [structural model (bottom right): Na^+ ions (purple), localized electrons (yellow)]. Three different phases of Na, *cI16*, $R\bar{3}m$ and *hP4*, are observed. The temperatures are estimated from hydrodynamics simulations.

ized valence electron charge.[1] Compared to the static compression data (*c*/*a* = 1.46), we observe a decrease in the *c*/*a* ratio with increasing pressure that agrees well with the density functional theory predictions and implies a stronger electron localization.[1]

At pressures between 242 and 292 GPa, the XRD pattern is consistent with a complex *cI16* phase. This is isostructural with the *cI16* phase of sodium near the minimum of the melting curve at lower temperatures and pressures (108 GPa, room temperature)[12] and lithium (40 GPa, 180 K).[13] The *cI16* structure (space group: *I*43*d*, 220) is a body-centered-cubic (bcc) superstructure with 16 atoms on the 16c Wyckoff site. The diffraction pattern has five peaks with a clearly different symmetry than the *hP4* structure, which was observed at these pressures in room-temperature experiments.[1] In one experiment at 315±11 GPa (shot 26479), a diffraction pattern distinct from both *cI16* and *hP4* was observed. The diffraction pattern was compared to those from theoretically predicted structures and other structures observed in alkali metals including *oP8*, *oC16*, *tI4*, and *tI19*, but none were found to match the observed diffraction pattern. A Bravais lattice and space group search[14] suggest a rhombohedral structure (space group: $R\bar{3}m$, 166). This is the same structure observed in As, Sb, and Bi (Ref. 15).

Figure 2(c) shows the average Na reflectivity as a function of time. As seen in both the raw data and the average across all experiments, the Na reflectivity drops to about 23%±4% of its initial value. The temperature–pressure paths of the reflectivity measurements are shown in Fig. 2(d), where hydrocode simulations are used to estimate the temperatures. The reflectivity is tracked through the bcc phase into the stability region of the fluid phase, and at the highest pressures, in the *cI16* phase and approaching the *hP4* phase where it is dark and nonreflective. A threefold drop in electrical conductivity is expected in the low-coordinated

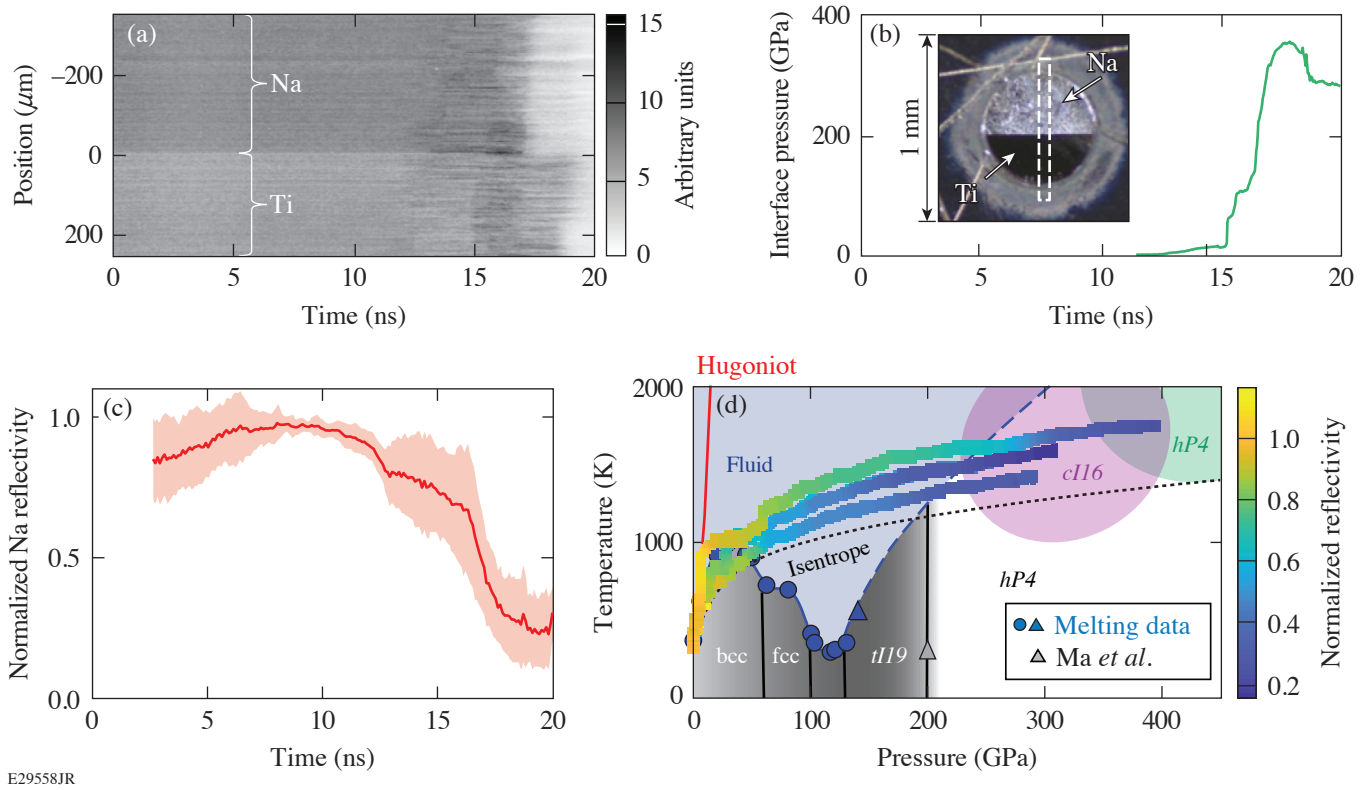

Figure 2

(a) A non-fringing VISAR (velocity interferometer system for any reflector) image for a Na target using a transparent MgO window and containing Ti coatings to detect changes in reflectivity (shot 27971). The non-fringing image is generated by blocking one arm of the VISAR interferometer, and shows no evidence of the pre-imposed striped reflectance pattern with a 150-μm period behind the Na layer. (b) (inset) A microscope image through the high-Z pinhole shows the Na layer (top) and the half-Ti overcoat (bottom) with the VISAR field of view overlaid (dashed box). The interface pressure of the shot shown in (a) shows that the drop in reflectivity is coincident with the increasing pressure. (c) Average (red curve) and standard deviation (red shaded region) of all Na reflectivity data normalized to the Ti reflectivity behind the transparent window. (d) The temperature–pressure phase diagram of Na with the simulated ramp-compression path (multicolor curves) for three reflectivity experiments.

liquid sodium between 40 and 80 GPa (Ref. 16). Similarly in liquid potassium, atomistic simulations predict a continuous transition from a free-electron metal to an electride liquid at pressures corresponding to the melting curve maximum and the onset of electride formation [10 to 20 GPa (K); 30 to 200 GPa (Na)] that manifests as a dip in the reflectivity similar to that observed here.[17] Reduced reflectance is consistently observed in host–guest structures in Na and K at lower pressure.[1,7,18]

Using laser-driven ramp compression, XRD measurements of sevenfold compressed Na are made in a regime where core overlap is thought to stabilize the formation of electride states. The observation of the *hP4* phase at 480 GPa and ~3000 K, which was previously observed to be transparent at 200 GPa and room temperature, implies that electride formation is possible on nanosecond time scales and at higher temperatures. At intermediate pressures, two additional unexpected phases of Na are observed. The reflectivity in both the liquid and solid stability regions is observed to continuously decrease where theory predicts a liquid–liquid phase transition to an electride fluid in alkali metals.[11,17] Interactions between core electrons occur in all materials at extreme densities and pressures, and these results give insight into the structural complexity and core-electron chemistry in Na—the most-striking example of a high-pressure electride.

This material is based upon work supported by the Department of Energy National Nuclear Security Administration under Award Number DE-NA0003856, the University of Rochester, and the New York State Energy Research and Development Authority.

1. Y. Ma *et al.*, Nature **458**, 182 (2009).
2. M.-S. Miao and R. Hoffmann, Account. Chem. Res. **47**, 1311 (2014).
3. X. Dong *et al.*, Nat. Chem. **9**, 440 (2017).
4. J. Dai *et al.*, Phys. Rev. Lett. **109**, 175701 (2012).
5. E. Gregoryanz *et al.*, Science **320**, 1054 (2008).
6. E. Gregoryanz *et al.*, Phys. Rev. Lett. **94**, 185502 (2005).
7. L. F. Lundegaard *et al.*, Phys. Rev. B **79**, 064105 (2009).
8. M. Marqués *et al.*, Phys. Rev. B **83**, 184106 (2011).
9. A. Lazicki *et al.*, Proc. Nat. Acad. Sci. **106**, 6525 (2009).
10. D. D. Meyerhofer *et al.*, J. Phys.: Conf. Ser. **244**, 032010 (2010).
11. R. Paul *et al.*, Phys. Rev. B **102**, 094103 (2020).
12. M. I. McMahon *et al.*, Proc. Nat. Acad. Sci. **104**, 17,297 (2007).
13. M. Hanfland *et al.*, Nature **408**, 174 (2000).
14. B. Toby and R. Dreele, J. Appl. Crystallogr. **46**, 544 (2013).
15. O. Degtyareva, M. I. McMahon, and R. J. Nelmes, High Pressure Res. **24**, 319 (2004).
16. J.-Y. Raty, E. Schwegler, and S. A. Bonev, Nature **449**, 448 (2007).
17. H. Zong *et al.*, Nat. Phys. **17**, 955 (2021).
18. K. Takemura and K. Syassen, Phys. Rev. B **28**, 1193(R) (1983).

On the Liquid–Liquid Phase Transition in Dense Hydrogen

V. V. Karasiev,[1] J. Hinz,[1] S. X. Hu,[1] and S. B. Trickey[2]

[1]Laboratory for Laser Energetics
[2]Quantum Theory Project, Department of Physics, University of Florida

Determining the liquid–liquid phase transition (LLPT) in high-pressure hydrogen is a longstanding challenge with notable variation in experimental and calculated results (see Refs. 1–5 and citations therein). Until recently, the computational consensus was for a first-order transition. Calculated values differed but, for example, our results on $700 \leq T \leq 3000$ K are a curve along $320 \geq P \geq 70$ GPa (Ref. 2). Driven by molecular H_2 dissociation, transition signatures include density jumps, qualitative and sharp changes in ionic pair correlation functions (PCF's), and abrupt dc conductivity and reflectivity changes. In distinct contrast, Cheng *et al.*[6] used molecular dynamics (MD) driven by a machine-learned potential (MLP) and found a continuous molecular-to-atomic liquid transformation that goes supercritical above $P \approx 350$ GPa, $T \approx 400$ K. They attributed the qualitative difference from MD-DFT (density functional theory) to (a) finite size effects that foster the formation of defective solids, with the common use of *NVT* dynamics tending to increase defect concentration relative to *NPT* ensemble results and (b) much shorter simulation times in the MD-DFT calculations than in the MD-MLP ones. Conceptually, the issue is whether a single MLP can correctly represent two chemically distinct regimes (molecular, atomic). An unambiguous test is to perform longer MD-DFT runs on significantly larger systems. If the MD-MLP represents the underlying theory (*ab initio* MD) faithfully and if the diagnosis based on MD-MLP is correct, results from the two simulation types should match. To test that, we have done much larger, longer MD-DFT calculations. The results are consistent with earlier MD-DFT calculations, thus qualitatively different from the MD-MLP results. Neither the large-system nor longer-run diagnosis from MD-MLP is sustained. Our *NPT* MD simulations were driven by DFT forces with Perdew–Burke–Ernzerhof (PBE) exchange correlation (XC).[7] (Reference 6 used PBE to train the MLP.) We used from 256 through 2048 atoms per cell. Brillouin zone sampling used the Baldereschi mean value point for the simple cubic crystal structure $\mathbf{k} = (1/4, 1/4, 1/4)$ (Ref. 8). *VASP*[9,10] was used for 1024 and 2048 atom systems, while the i–PI interface[11] with *Quantum Espresso*[12] was used for 256 and 512 atoms. Consistent results from the two confirm that the MD code and technical choices (thermostat, barostat, etc.) are inconsequential.

Our new large-system MD-DFT results agree with prior MD-DFT and coupled electron–ion Monte Carlo simulations:[2,3,13] there is a sharp molecular-to-atomic transition. Figure 1 shows the qualitatively different character versus the MD-MLP prediction. Figure 1(a) shows density profiles $\rho_H(T)$ along isobars. At 300 and 350 GPa, the large-scale MD-DFT $\rho_H(T)$ values jump ≈1% near $T = 650$ K. At 300 GPa, that is above the experimental melting temperature T_m (Ref. 14). In contrast, the 300-GPa MD-MLP isobar has a steep density increase near $T = 500$ K (in the stable solid phase),[6] but it passes smoothly through both the melt line and the LLPT. Except for a systematic offset, the MD-MLP $\rho_H(T)$ matches the MD-DFT $\rho_H(T)$ in the atomic fluid region.

The molar heat capacity from MD-DFT as a function of T is shown in Fig. 1(b). All the isobars exhibit divergent heat capacity character across the transition. Evidently finite-size effects on T_{LLPT} are small and do not modify that character. To check on the possibility that finite-size effects trapped our simulations in defective solid configurations, we calculated the mean-squared displacement (MSD) of the 512 atom systems as a function of time along the 150- and 200-GPa isobars for $1100 \leq T \leq 1400$ K and $900 \leq T \leq 1200$ K, respectively. The MSD (not shown here) grows near linearly with time, as is characteristic of a liquid but not a solid.

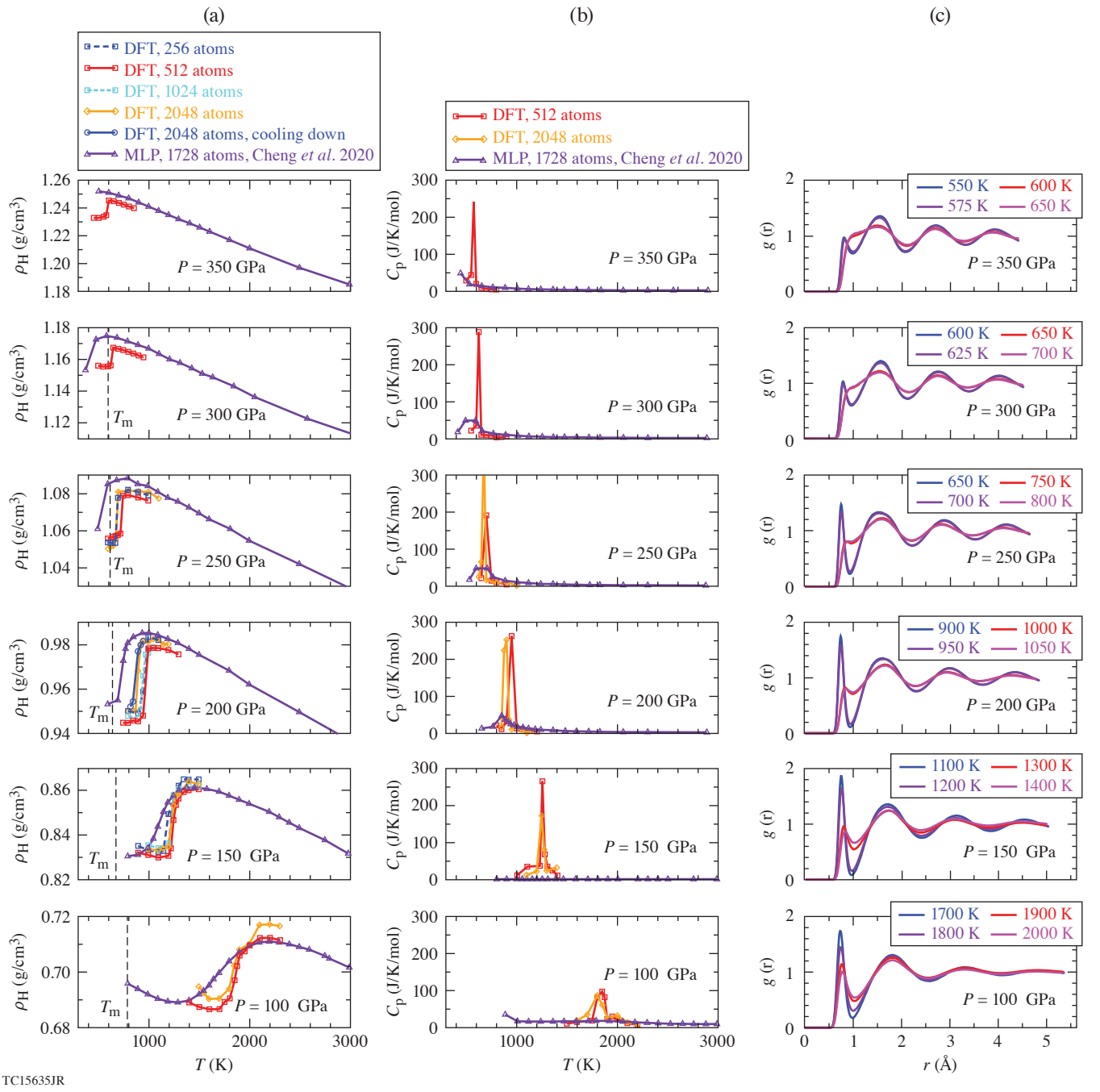

Figure 1
Comparison of MD results from the PBE XC–based MLP and *ab initio* MD-DFT (DFT) *NPT* simulations. (a) Hydrogen density as a function of T along six isobars. Experimental melting temperature T_m for each isobar is shown by a vertical dashed line.[14] (b) Molar heat capacity as a function of T along the isobars. (c) PCF for each isobar for two temperatures below the density jump and two temperatures above the density jump.

Figure 1(c) shows the PCF on each isobar at temperature pairs below and above the density jump. Above, the first PCF peak virtually disappears, confirmation of the density jump being in conjunction with the molecular dissociation.[2]

To test possible long simulation duration effects on T_{LLPT} or its character, we performed six sequential MD-DFT runs of roughly 1.8-ps duration each for a total of ≈10-ps duration and at 200 GPa with 512 and 2048 atoms. There were no meaningful differences in the results in either case. This outcome agrees with that of Geng *et al.*[15] who performed runs up to 6 ps and found no meaningful differences with respect to 1.5 ps (after equilibration). To investigate whether the nanosecond time scale might make the simulated transition smooth, we performed a set of 2048-atom MD-DFT *NPT* simulations beginning with the atomic fluid at 200 GPa. Starting at 950 K, we cooled the system in sequential runs to 899, 849, and 824 K with simulation duration around 8 ps for each temperature. If the nanosecond time scale were to yield a smooth transition, the hydrogen density during such a fast cooling curve would not drop sharply below the hypothetical smooth long-duration curve. But, as evident in the Fig. 1(a) density plot at 200 GPa, the cooling curve (thin blue curve, circles) is almost identical to the one from MD-DFT simulations when the molecular fluid T is increased gradually (sharp transition shown by the solid orange curve).

Figure 2 shows the LLPT curves associated with density jumps, heat capacity peaks, and PCF peak disappearance. For the new large-scale MD-DFT calculations, those three criteria give one curve shown in red with squares at data points. With virtually identical P,T values; small differences in the transition temperature (less than 100 K for $P \leq 150$ GPa) are caused by numerical errors in calculating the molar heat capacity using finite differences. Two MD-MLP curves emerge from the analysis, however, one for the location of molar heat capacity maxima, $C_P^{\max}$, and another for the maximum density, $\rho^{\max}$. Consistent with the foregoing discussion, there are striking differences. The MLP $C_P^{\max}$ curve lies well below the MD-DFT curve. The MLP $\rho^{\max}$ curve is flatter than the MD-DFT reference curve and lies close to it only at about $P = 70$ GPa, $T = 2800$ K and then again for P between about 170 and 300 GPa.

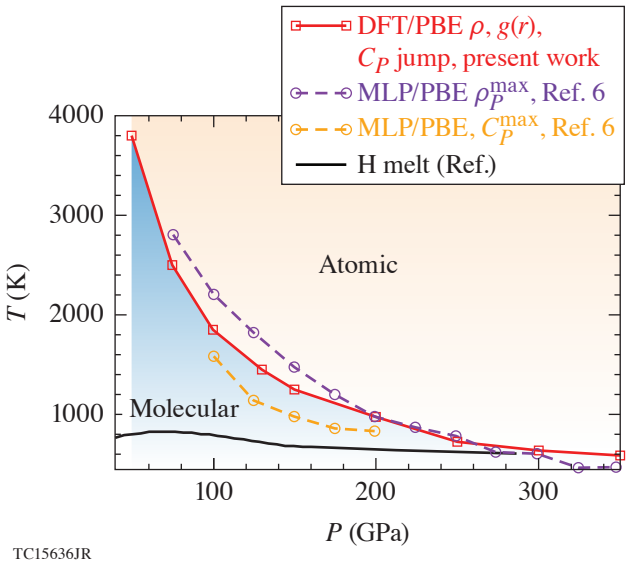

Figure 2
The LLPT boundary from the present large-scale MD-DFT (DFT/PBE) simulations compared to MLP (MLP/PBE) $C_P^{\max}$ and $\rho^{\max}$ curves.

Given that neither the finite-size nor simulation duration diagnosis advanced in Ref. 6 is sustained by direct-calculation of chemically distinct regimes (molecular, atomic) of the hydrogen, we conclude that the MD-MLP results for the LLPT do not reproduce the fundamental MD-DFT results as they should. Up to 2048 atoms and 10-ps simulation duration, our results are consistent with the earlier subcritical behavior predictions.

V. V. Karasiev, J. Hinz, and S. X. Hu were supported by the Department of Energy National Nuclear Security Administration Award Number DE-NA0003856 and U.S. National Science Foundation PHY Grant No. 1802964. S. B. Trickey was supported by Department of Energy Grant DE-SC0002139. This research used resources of the National Energy Research Scientific Computing Center, a DOE Office of Science User Facility supported by the Office of Science of the U.S. Department of Energy under Contract No. DE-AC02-05CH11231. Part of the computations were performed on the Laboratory for Laser Energetics HPC systems.

1. E. Gregoryanz *et al.*, Matter Radiat. Extremes **5**, 038101 (2020).
2. J. Hinz *et al.*, Phys. Rev. Research **2**, 032065(R) (2020).
3. G. Rillo *et al.*, Proc. Natl. Acad. Sci. **116**, 9770 (2019).
4. B. Lu *et al.*, Chin. Phys. Lett. **36**, 103102 (2019).
5. C. Pierleoni *et al.*, Proc. Natl. Acad. Sci. **113**, 4953 (2016).
6. B. Cheng *et al.*, Nature **585**, 217 (2020).
7. J. P. Perdew, K. Burke, and M. Ernzerhof, Phys. Rev. Lett. **77**, 3865 (1996); **78**, 1396(E) (1997).
8. A. Baldereschi, Phys. Rev. B **7**, 5212 (1973).
9. G. Kresse and J. Furthmüller, Phys. Rev. B **54**, 11,169 (1996).
10. G. Kresse and D. Joubert, Phys. Rev. B **59**, 1758 (1999).
11. V. Kapil *et al.*, Comput. Phys. Commun. **236**, 214 (2019).
12. P. Giannozzi *et al.*, J. Phys.: Condens. Matter **29**, 465901 (2017).
13. W. Lorenzen, B. Holst, and R. Redmer, Phys. Rev. B **82**, 195107 (2010).
14. C. S. Zha *et al.*, Phys. Rev. Lett. **119**, 075302 (2017).
15. H. Y. Geng *et al.*, Phys. Rev. B **100**, 134109 (2019).

Impact of Electrode Geometry on the Efficiency of Metal–Semiconductor–Metal AlGaN Ultraviolet Photodiodes

S. F. Nwabunwanne and W. R. Donaldson

Laboratory for Laser Energetics, University of Rochester

Fast aluminum-gallium-nitride ($Al_xGa_{1-x}N$)–based metal–semiconductor–metal (MSM) ultraviolet (UV) photodiodes (PD's) have been successfully designed, fabricated, and characterized using conventional photolithography techniques. Various electrode geometries were fabricated to investigate the influence of metal contact shapes on device performance indices with emphasis on the response speed and bias-voltage–independent efficiency. Peak response times from the best devices were evaluated with a bias-voltage–independent, external quantum efficiency of 1198% at 19.5 V and 70% at 60 V for *n*-doped and intrinsic devices, respectively. Based on the measured mobility, these devices should be capable of a response time as short as 1.31 ps.

$Al_xGa_{1-x}N$-based UV PD's have been the subject of active research due to their intriguing material properties. Sustained interest in $Al_xGa_{1-x}N$ photodetectors stems from their impressive characteristics such as a wide and tunable direct band gap, thermal resistivity, radiation sturdiness, and electrical robustness. The ability to easily select the detected wavelength by simply varying the aluminum content of $Al_xGa_{1-x}N$ is a significant advantage of these group III–V compounds. Also, $Al_xGa_{1-x}N$ photodetectors can be specifically designed to look at specific spectral windows.[1,2]

Intrinsic and Si-doped wafers obtained from KYMA Technologies were prepared by metal organic chemical-vapor deposition (MOCVD). A thin AlN layer serves to minimize the lattice constant mismatch between intrinsic/*n*-doped AlGaN thin films and the sapphire substrate. Si-doped wafers have a carrier density of 1×10^{18} cm^{-3}, while the intrinsic wafers have a carrier density of 1×10^{17} cm^{-3}. The Hall-effect measurements of Si-doped $Al_{0.1}Ga_{0.9}N$ thin films using the van der Pauw[3] geometry configuration resulted in a carrier mobility of 127 cm^{2}V^{-1}s^{-1}, a carrier density of 2×10^{18} cm^{-3}, and a resistivity of 0.0243 Ωcm. Similarly, for Si-doped $Al_{0.2}Ga_{0.8}N$ thin film, the carrier mobility was measured as 10.4 cm^{2}V^{-1}s^{-1}, the carrier density as 1×10^{18} cm^{-3}, and resistivity as 0.5656 Ωcm. We investigated the defect densities of the wafers using x-ray rocking-curve measurements, which yielded 1.4398×10^6 cm^{-2} and 1.9288×10^6 cm^{-2} dislocation densities for intrinsic $Al_{0.1}Ga_{0.9}N$ and $Al_{0.2}Ga_{0.8}N$ thin films, respectively. For *n*-doped wafers, dislocation densities were 1.0201×10^6 cm^{-2} and 1.4702×10^6 cm^{-2} for $Al_{0.1}Ga_{0.9}N$ and $Al_{0.3}Ga_{0.7}N$, respectively. These numbers are among the lowest reported dislocation densities in AlGaN thin films; typically dislocation densities are of the order of 10^7 to 10^8 cm^{-2} (Refs. 2 and 4).

Two different electrode geometries were fabricated on the Pt and Au devices. There are a total of five interdigitated fingers for each device configuration, which consists of 1×5-μm-wide electrodes that are spaced at 2-μm and 3-μm intervals. The electrodes on our previous devices covered 50% (Ref. 1) of the active area but these devices' electrodes cover about 30% of the active area. This implies ~20%-more incident UV light will be absorbed by the PD, resulting in improved sensitivity. An antireflection (AR) layer consisting of 44 nm of SiO_2 was designed for near-zero reflectivity at 262 nm, contributing ~20% improvement in the external quantum efficiency (EQE) of the PD's.

The light source was a 262-nm *Q*-switched Crystalaser with 10-ns pulse duration and 4.5 nJ of energy, externally clocked at 2.5 kHz. The beam diameter of the laser at the PD was 138 μm. Approximately 0.05 nJ per pulse reached the active area of the device. A Si-biased PD was employed as a reference detector to account for variation in the pulse energy. A half-wave plate combined with the UV polarizer was employed to control the amount of UV energy reaching both diodes during the reference

diode calibration. A 12.5-GHz Tektronix oscilloscope served as the primary measurement tool for the MSM AlGaN PD's, which introduced a bandwidth constraint on our ability to measure the intrinsic impulse response of these devices.

With the electrode's geometry varied to facilitate absorption of 20% more of the incident photons as well as a strong electric field of 1×10^7 V/m at 20-V bias voltage, which is 40% greater than the electric field in the previous devices, we observed for the first time with these PD's, a bias-voltage–independent EQE of 1198% at 19.5 V and 70% at 60 V for the best-performing *n*-doped and intrinsic devices, respectively. As evidenced by the long tail in response, the Pt device must be in photoconductive mode, causing a multiplication of carriers that accounts for the superhigh EQE. While we desire efficient devices, the photoconductive gains of some of these devices are unsuitable for ultrafast laser pulse characterization due to their long tails. The EQE of the AlGaN devices, which is the ratio of the number of photogenerated carriers to the number of incident photons, was calculated using

$$QE(\eta) = \frac{I_{\text{ph}}/e}{P/h\nu}, \tag{1}$$

where I_{ph} is the photocurrent (A) obtained by averaging the diode's voltage response measured over time and multiple acquisitions and dividing by 50-Ω oscilloscope's impedance; e is the charge; P denotes the optical power (W) of the incident light; h is Planck's constant; and ν is the frequency (Hz) of the input light. The voltage response curves were acquired ten times at each bias voltage and then integrated over 1.5-ns time interval. The efficiency of a PD is shown in Fig. 1. This represents a significant improvement over previous devices. A plausible contribution to the improvement in the EQE is the elevated electric field that drove the photogenerated carriers to saturation velocity, thereby preventing their recombination before they could be removed at the contacts. We estimate that the elevated electric field contributed about 30% to the boost in the EQE. Furthermore, the low number of defects in the $Al_xGa_{1-x}N$ thin films translated to a reduced number of trap sites that impede the free flow of carriers when photoexcited. This improved the mobility of the carriers, leading to a pronounced 30% increase in the EQE. Finally, the Schottky contacts formed with Pt and Au have been reported to reduce UV detection since they cast opaque shadows on the semiconductor, thereby reducing the efficiency of UV absorption.[5–7] We reduce this impact of Pt and Au electrodes by making them thinner and fewer in number. Also, Schottky contacts block current from –5 V to 5 V, which is less than –8 V to 8 V in the previous devices, thereby leading to a rise in the photocurrent and contributing ~20% to the jump in the EQE. Finally, it is evident that some photoconductive gain mechanisms could have added to the photogenerated current accounting for about 10% elevation in the EQE for intrinsic devices and adding >50% in *n*-doped devices.

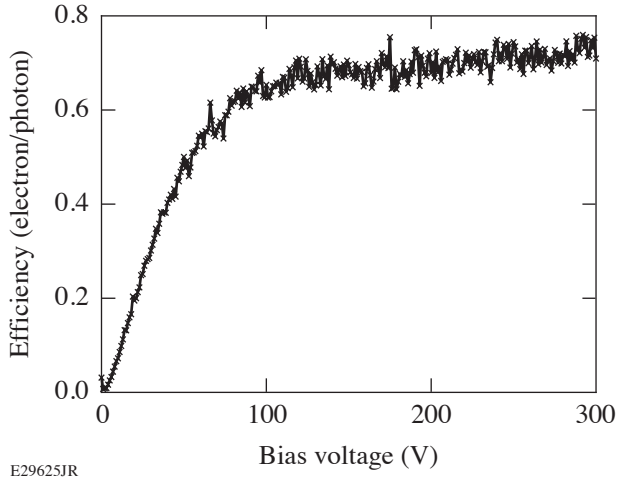

Figure 1
External quantum efficiency of AlGaN PD as a function of bias voltage with saturation beginning at 75 V.

This material is based upon work supported by the Department of Energy National Nuclear Security Administration under Award Number DE-NA0003856, the University of Rochester, and the New York State Energy Research and Development Authority.

1. Y. Zhao and W. R. Donaldson, IEEE J. Quantum Electron. **56**, 4000607 (2020).
2. Y. Zhao and W. R. Donaldson, IEEE Trans. Electron Devices **65**, 4441 (2018).
3. D. M. Boerger, J. J. Kramer, and L. D. Partain, J. Appl. Phys. **52**, 269 (1981).
4. R. Gaska *et al.*, Appl. Phys. Lett. **72**, 707 (1998).
5. S. Wang *et al.*, IEEE Photon. Technol. Lett. **33**, 213 (2021).
6. P. C. Chang *et al.*, J. Alloys Compd. **504**, S429 (2010).
7. F. Bouzid, L. Dehimi, and F. Pezzimenti, J. Electron. Mater. **46**, 6563 (2017).

Impact of Boundary Sharpness on Temporal Reflection in Dispersive Media

J. Zhang,[1] W. R. Donaldson,[2] and G. P. Agrawal[1,2]

[1]The Institute of Optics, University of Rochester
[2]Laboratory for Laser Energetics, University of Rochester

In this summary, we investigate the impact of the finite rise time of a temporal boundary inside a dispersive medium used for temporal reflection and refraction of optical pulses. We develop a matrix approach in the frequency domain for analyzing such temporal boundaries and use it to show that the frequency range over which reflection can occur is reduced as the rise time increases. We also show that total internal reflection can occur even for shallow boundaries. This feature suggests that temporal waveguides can be realized through cross-phase modulation, even when pump pulses have relatively long rise and fall times. In past studies, the moving temporal boundary was assumed to be infinitely sharp such that the refractive index changes instantaneously at the boundary location. In practice, any temporal boundary will have a finite rise time. One expects the results obtained for a sharp boundary to remain valid as long as the rise time is much shorter than other time scales of interest (such as the width of the pulse being reflected at the boundary). It is not known, however, how the results obtained for a sharp boundary need to be modified when the rise time of the temporal boundary is non-negligible.

We assume that a temporal boundary, moving at the speed V_B, has been created inside the dispersive medium using a suitable technique (e.g., cross-phase modulation with a pump pulse) so that the refractive index of the medium differs by a small amount Δn on the two sides of the boundary. In most previous studies on temporal reflection, $s(t)$ is taken to be a step function of the form $h(t–T_B)$, assuming an infinitely sharp boundary located at $t = T_B$. In this work, we consider temporal boundaries with a finite rise time T_r; in particular, $s(t)$ was considered to be a super-Gaussian of order m, $e^{-[(t-T_B)/T_0]^{2m}}$, where $T_r \sim T_0/m$.

For a sharp boundary with $T_r = 0$, it is known that a pulse splits into two parts after it arrives at the boundary, which can be identified as the reflected and transmitted parts.[1] Their spectra are shifted from the spectrum of the incident pulse in such a way that the reflected part never crosses the boundary. We extend this approach to temporal boundaries of arbitrary shapes by making a reasonable approximation. We divide the boundary region into N segments, each of finite duration such that $s(t)$ can be treated as a constant inside the segment. In other words, we replace the actual shape of the boundary with a staircase. This can be done for a boundary of any shape if we make N large enough that $s(t)$ does not vary much inside each segment. Consider one spectral component of the pulse before the first segment with the frequency $\omega = \omega_0 + \delta_0$. It propagates as a plane wave $A_0 e^{i(Kz-\delta_0 t)}$. As this plane wave traverses the boundary region, its frequency changes from one segment to the next, but K remains the same because of momentum conservation at any temporal boundary.[1] At the same time, a reflected wave is produced with a shifted frequency. As a result, two plane waves exist in the nth segment, where $s(t) = s_n$ is a constant.

Our approach is similar to that used for calculating the reflectivity of a stack of multiple dielectric layers.[2] We use the transfer and propagation matrices to cross all segments, starting from the far end of the last segment. The resulting matrix of the entire temporal boundary is the product of $2N + 1$ matrices. In terms of the four elements of this matrix, the incident, reflected, and transmitted waves are related as

$$\begin{pmatrix} A_{in} \\ A_R \end{pmatrix} = \begin{pmatrix} M_{11} & M_{12} \\ M_{21} & M_{22} \end{pmatrix} \begin{pmatrix} A_T \\ O \end{pmatrix}.$$

The reflectivity and transmissivity of the temporal boundary are given by $R = |M_{21}/M_{11}|^2$ and $T = |1/M_{11}|^2$, where the matrix elements can be computed using the group velocity, the group velocity dispersion, and the frequency shift across the boundary. One interesting feature of an infinitely sharp temporal boundary is that the analog of total internal reflection (TIR) can occur, i.e., it is possible to have the situation where the faster-propagating probe pulse never overtakes the slower-moving pump because the frequency of the probe pulse changes. We can normalize the parameter $(\omega_0/c)\,\Delta n$ to the minimum value for TIR to occur. Physically, this normalized parameter B represents the value of the index change relative to the value required for TIR to occur.

As seen in Fig. 1, TIR occurs for Δf values below 0.3 THz. The reason it ceases to occur for larger values of Δf is related to a larger speed mismatch between the wave relative to the moving boundary. As Δf increases beyond 0.3 THz, change in the propagation constant continues to increase, which decreases the reflectivity further. The rate of decrease depends on the boundary's rise time, and it becomes more rapid as T_r increases (or m decreases). For a Gaussian-shaped boundary with $m = 1$, the reflectivity becomes nearly a step function of Δf. In practical terms, for such boundaries, a narrowband signal is either totally reflected or fully transmitted, depending on its frequency. We considered two cases with $B = 0.95$ and $B = 1.05$, where $B = 1$ is required for TIR to occur. In the first case ($B = 0.95$), 96% of the pulse energy crosses the boundary. For $B = 1.05$, all the energy is reflected because the index change across the boundary is larger by 10% and exceeds the TIR threshold of $B = 1$. These results show that a relatively small change in the refractive index can produce large changes in the transmitted energy of a probe pulse when pump pulses are used to create a moving temporal boundary using the Kerr nonlinearity of an optical fiber.

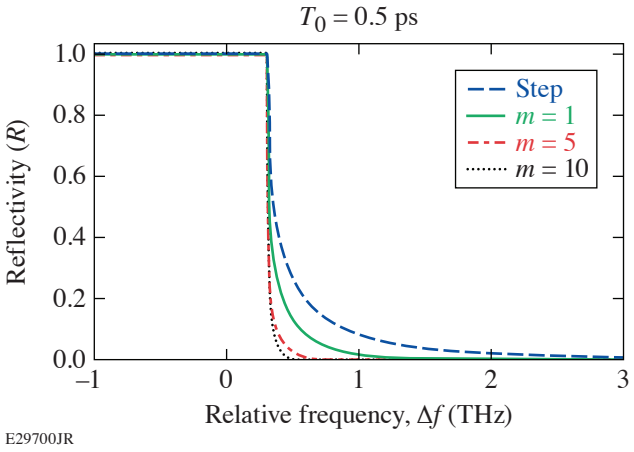

Figure 1
Dependence of the reflectivity spectrum on the rise time of a temporal boundary ($T_0 = 0.5$ ps) is shown using three values of m. The dashed curve shows, for comparison, the case of a step-function boundary.

This material is based upon work supported by the National Science Foundation (ECCS-1933328).

1. B. W. Plansinis, W. R. Donaldson, and G. P. Agrawal, Phys. Rev. Lett. **115**, 183901 (2015).
2. S. J. Orfandis, *Electromagnetic Waves and Antennas* (2016) [Online], Chap. 6. Available: https://www.ece.rutgers.edu/~orfanidi/ewa/.

Time-Domain Fabry–Perot Resonators Formed Inside a Dispersive Medium

J. Zhang,[1] W. R. Donaldson,[2] and G. P. Agrawal[1,2]

[1]The Institute of Optics, University of Rochester
[2]Laboratory for Laser Energetics, University of Rochester

In this summary, we show that the temporal analog of a Fabry–Perot resonator (FPR) can be realized by using two moving temporal boundaries inside a dispersive medium, such as an optical fiber.[1–3] In practice, such boundaries are created by using a pump–probe configuration in which one or more short pump pulses are launched together with a probe pulse. Each pump pulse increases the refractive index of the single mode of the fiber through the nonlinear Kerr effect, but this increase occurs only over the duration of the pump pulse. The temporal FPR can be probed by an optical pulse that is injected into the fiber after the pump pulse is injected. The frequency of the probe pulse must be such that it propagates faster than the pump pulse. Physically, when the probe pulse crosses the pump pulse (the temporal slab), a part of the probe pulse changes its frequency such that it speeds up and travels ahead of the pump pulse, while part of the probe changes frequency so that it appears to move more slowly than the pump pulse. Inside this slab, the index change is small, 3×10^{-7}, and can be realized in practice using a short, intense 1-ps pump pulse. To calculate the transmissive properties of time-domain FPR's, we develop a transfer-matrix method similar to that used for analyzing the reflectivity of a spatial structure containing multiple thin films. We show that this method can be used for calculating the transfer matrix of pump pulses of any shape. As a simple example, we first consider a temporal slab formed by using a single pump pulse with sharp leading and trailing edges (rectangular shape pulse) and acting as a simple FPR. We found that such an FPR has several transmission peaks corresponding to resonances similar to spatial FPR's. If the frequency of the probe pulse is at the peak of the first resonance, more than 90% of the pulse energy is transmitted through the slab. Reflective losses (about 7%) occur due to the finite distance it takes for the probe pulse to cross the slab. Indeed, we see two reflected pulses that correspond to reflections at the two interfaces of the slab. If the probe pulse is centered on the first minimum of the temporal FPR, the reflected pulse contains most of the input energy. The bandwidth (or Q factor) and contrast of these peaks, however, decrease rapidly with increasing frequency. In contrast with spatial FPR's, for which mirror reflectivity remains constant over a wide bandwidth, temporal reflection is very sensitive to the frequency of incident light.

We propose an improved design for time-domain FPR's by using two temporally separated pump pulses such that each pump pulse acts as a reflective element of the FPR. We apply our transfer-matrix method to this design for pulses of arbitrary shapes and obtain an expression for the transmissivity of such FPR's that appears identical to the corresponding result for space-domain FPR's. To illustrate the performance of the proposed FPR, we consider a practical configuration: The pump pulses' wavelength is in the anomalous dispersion region of the optical fiber while the probe pulse is in the normal dispersion region. Two pump pulses propagate as two optical solitons and their center is delayed by T_c (Ref. 4). A high-index region forms over the width of each pulse because of a Kerr-induced increase in the refractive index of the fiber's mode. Choosing the pump pulses to have a secant-squared temporal shape with a width of 90 fs (FWHM) and a separation of 1.4 ps with an intensity such that $\Delta n = 3 \times 10^{-7}$, we calculated the transmission characteristics for the two cases of the input spectrum center at the first maximum of the zeroth-order peak, and input spectrum at the first minimum below the zeroth order peak. These results are shown in Fig. 1.

We also show that temporal FPR's formed in the anomalous group-velocity dispersion region of optical fibers by using two short solitons to form multiple sharp transmission peaks with relatively high Q factors. We verified the results of the transfer-matrix method by directly solving the pulse-2 propagation equation with the split-step Fourier method. We showed that a probe pulse can

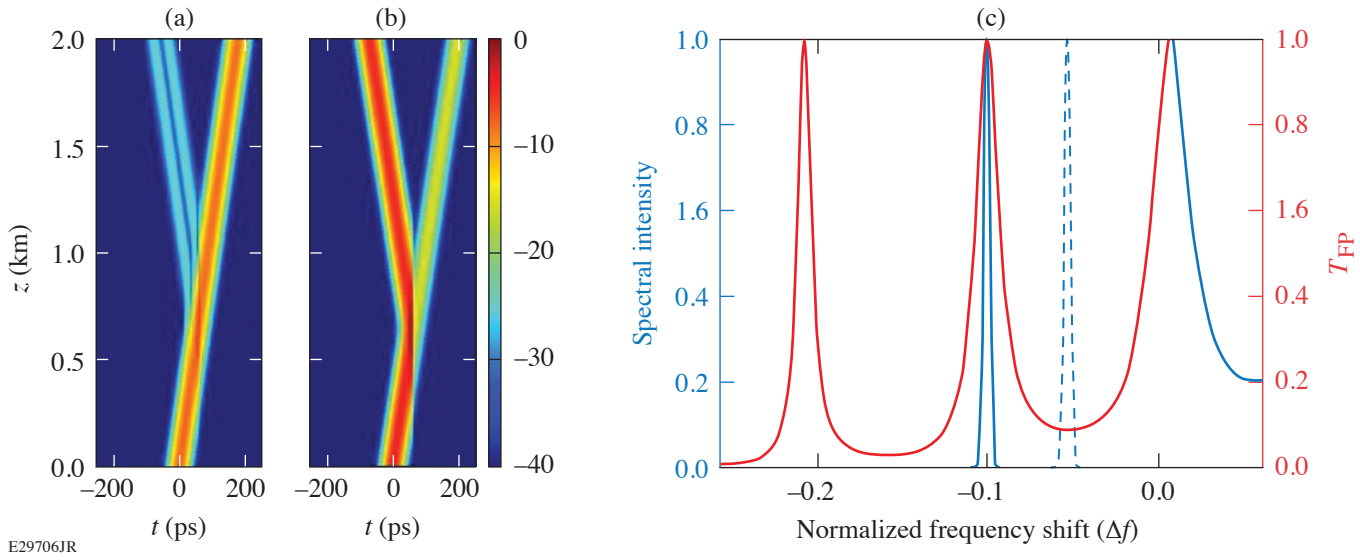

Figure 1
Temporal evolution of a 20-ps Gaussian pulse when its spectrum is centered at (a) a transmission peak and (b) a transmission valley. (c) Location of pulse spectra within the transmission curve (red) of the FPR. The solid blue curve is the incident spectrum in (a) and the dashed line is the incident spectrum in (b); spectral intensity is plotted. Both blue curves plot the spectral intensity.

be fully transmitted through such an FPR when its spectrum overlaps with that of a transmission peak of the FPR. If the spectral bandwidth is larger than the transmission peak width, the temporal FPR acts as an optical filter, analogous to spatial FPR's.

This material is based upon work supported by the National Science Foundation (ECCS-1933328).

1. J. T. Mendonça and P. K. Shukla, Phys. Scr. **65**, 160 (2002).
2. B. W. Plansinis, W. R. Donaldson, and G. P. Agrawal, Phys. Rev. Lett. **115**, 183901 (2015).
3. J. Zhang, W. R. Donaldson, and G. P. Agrawal, J. Opt. Soc. Am. B **38**, 997 (2021).
4. G. P. Agrawal, *Nonlinear Fiber Optics*, 6th ed. (Academic Press, Boston, 2019).

MTW-OPAL: A Technology Development Platform for Ultra-Intense All-OPCPA Systems

J. Bromage, S.-W. Bahk, I. A. Begishev, S. Bucht, C. Dorrer, C. Feng, B. N. Hoffman, C. Jeon, C. Mileham, J. B. Oliver, R. G. Roides, M. J. Shoup III, M. Spilatro, B. Webb, and J. D. Zuegel

Laboratory for Laser Energetics, University of Rochester

Ultra-intense laser systems are being developed by several institutions to use the full potential of deuterated potassium dihydrogen phosphate (DKDP) for high-energy optical parametric chirped-pulse amplification (OPCPA).[1–4] Noncollinear optical parametric amplifiers (NOPA's) using DKDP can support broadband gain for supporting pulses as short as 10 fs. Large-aperture DKDP crystals (>400 mm) make it possible to use Nd:glass lasers as kilojoule pump sources.[5] Although OPCPA is now routinely used as a broadband front-end technology for many hybrid systems, scaling OPCPA to energies >100 J is still an active area of laser research and development. This summary reports on the MTW-OPAL Laser System, a mid-scale optical parametric amplifier line pumped by the Multi-Terawatt laser, as a platform for the laser technology development with a long-term goal of building EP-OPAL, a femtosecond-kilojoule system within the Omega Laser Facility.[6]

The MTW-OPAL Laser System is shown schematically in Figs. 1 and 2, and described in more detail in Ref. 7. The ultra-broadband front end produces stretched pulses using white-light continuum generation and a series of three NOPA's using beta

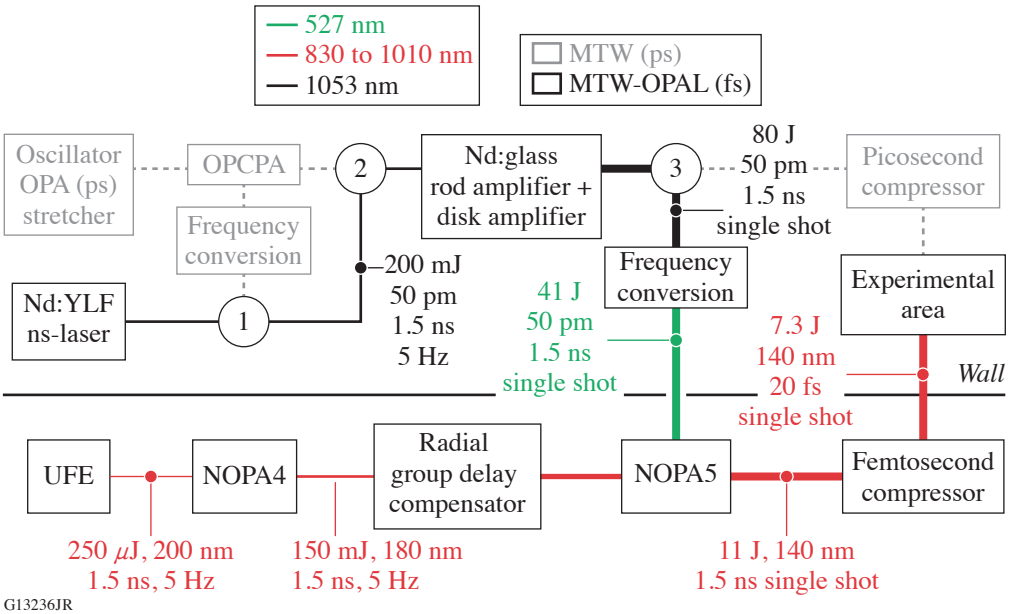

Figure 1
Schematic of the MTW-OPAL Laser System. UFE: ultra-broadband front end.

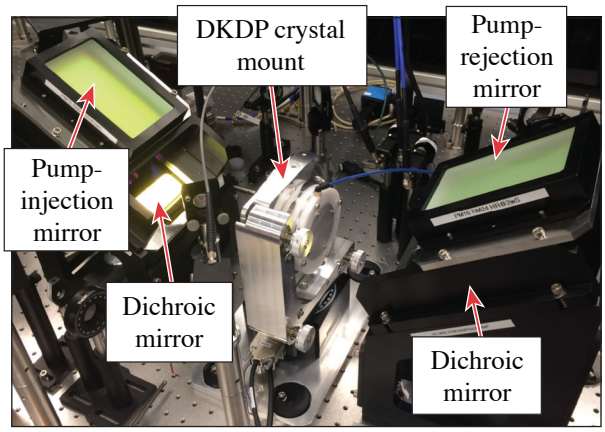

Figure 2
NOPA5 amplifier showing surrounding optics.

barium borate (BBO) crystals that are pumped with picosecond pulses for maximum temporal contrast. The pulse is stretched to 1.5 ns and matched to the pump pulse for the two NOPA4 stages (also BBO crystals) and the pump for the final NOPA5 stage (DKDP); the NOPA5 pump pulse is produced by the MTW laser configured in a narrowband mode. Radial group-delay compensation is used to minimize temporal broadening from refractive telescopes that image each amplifier stage to the next. A femtosecond compressor with a suite of laser diagnostics is used to compress the pulse to <20 fs before transport in vacuum to the experimental area.

Demonstrating large-aperture OPCPA is a primary goal of the MTW-OPAL project. NOPA5 uses $63 \times 63 \times 52\text{-mm}^3$ 70% deuterated DKDP crystals to amplify 45-mm-sq beams with gains of ~100, producing 11-J broadband pulses with up to 40% pump-to-signal transfer efficiency.[8] Another primary goal is demonstrating a scalable four-grating compressor, transport optics, and diagnostics suitable for EP-OPAL. An all-reflective achromatic telescope has been developed for relay imaging NOPA5 to the final grating. Hybrid coatings (metal and multilayer dielectric) suitable for 200-nm bandwidth are being evaluated for use in the vacuum compressor chamber for both *s*- and *p*-polarized beams.

Figure 3 shows a summary of the primary results from the "First-Light" Campaign in March 2020 along with the subsequent campaigns to ramp the energy through the compressor to achieve 0.35 PW. These campaigns show that the laser design is fundamentally sound, and optimization continues as we prepare for "First Focus" campaigns later this year.

This material is based upon work supported by the Department of Energy National Nuclear Security Administration under Award Number DE-NA0003856, the University of Rochester, and the New York State Energy Research and Development Authority.

1. I. N. Ross *et al.*, Opt. Commun. **144**, 125 (1997).
2. V. V. Lozhkarev *et al.*, Opt. Express **14**, 446 (2006).
3. C. N. Danson *et al.*, High Power Laser Sci. Eng. **7**, e54 (2019).
4. V. V. Lozhkarev *et al.*, Laser Phys. **15**, 1319 (2005).
5. J. B. Hu *et al.*, Appl. Opt. **60**, 3842 (2021).
6. J. H. Kelly *et al.*, J. Phys. IV France **133**, 75 (2006).
7. J. Bromage *et al.*, High Power Laser Sci. Eng. **7**, e4 (2019)
8. I. A. Begishev, *et al.*, Proc. SPIE **11666**, 1166607 (2021).

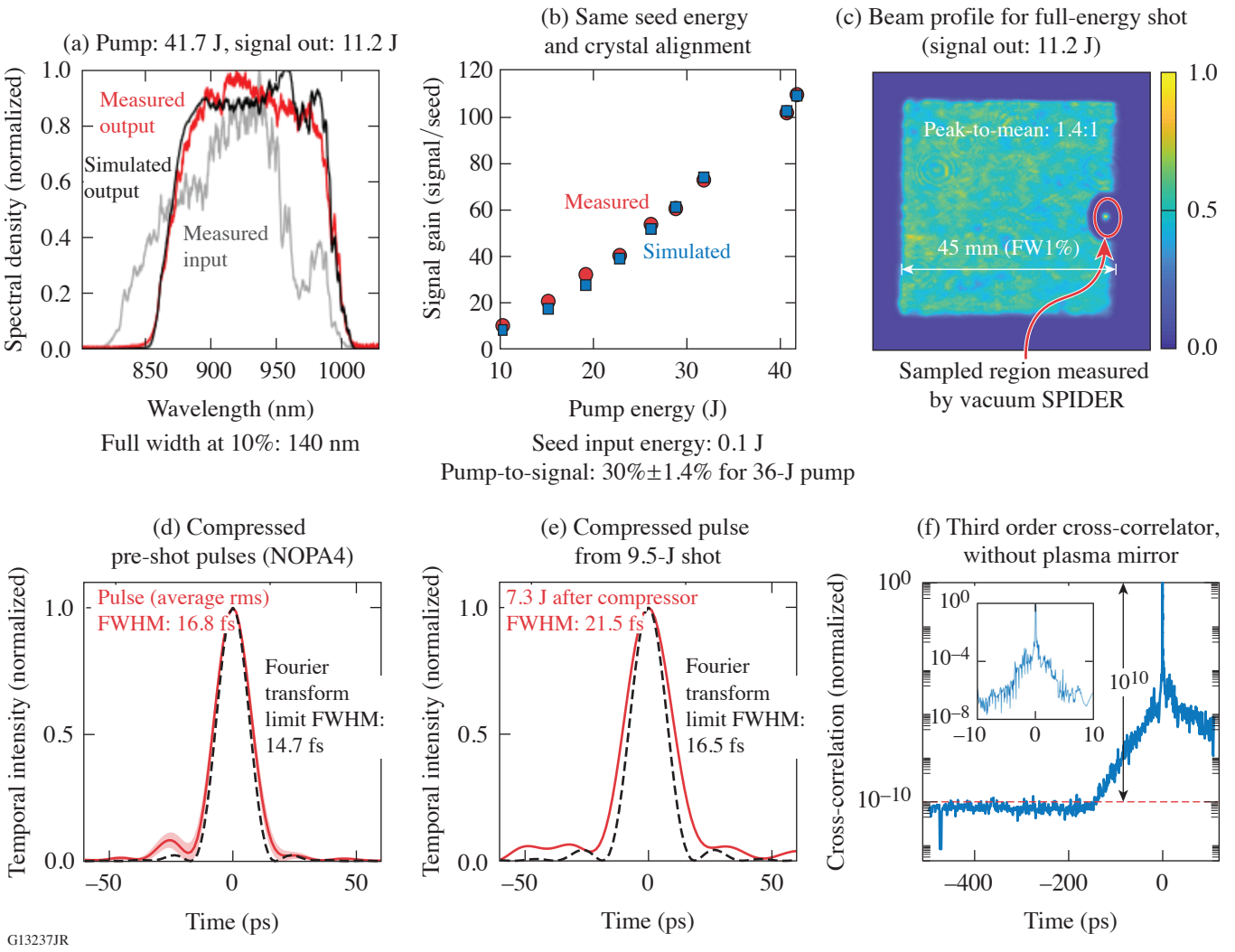

Figure 3

(a) NOPA5 spectral measurements for a full-energy shot (input, output, and simulated). (b) Signal gain measured after NOPA5, with a maximum signal energy of 11.2 J. (c) Full-energy NOPA5 output beam. (d) SPIDER measurement statistics (50 shots) and Fourier transform limit for compression without pumping NOPA5. (e) Vacuum SPIDER measurement of spatially sampled beam with the full-energy output from NOPA5. (f) Temporal contrast measurements of compressed NOPA5 seed pulses.

Alignment Tolerance Analysis for Divided-Pulse Nonlinear Compression

G. W. Jenkins,[1,2] C. Feng,[1] and J. Bromage[1,2]

[1]Laboratory for Laser Energetics, University of Rochester
[2]Institute of Optics, University of Rochester

Recent work has pushed self-phase modulation (SPM)-based spectral broadening to higher pulse energies and peak powers in both hollow-core fiber (HCF)[1] and multipass cells (MPC's).[2] While these demonstrations have shown that spectral broadening using gas-based SPM can handle very high pulse energies, they also show that the process is limited by gas ionization. They must therefore employ large-core fibers or large focal spots in the MPC to avoid gas ionization.

This work is focused on a more-scalable method to improve the energy limits of SPM-based pulse compression: divided-pulse nonlinear compression (DPNLC) (illustrated in Fig. 1). In DPNLC, a high-energy pulse is divided into multiple low-energy pulses that are spectrally broadened, recombined back into a high-energy pulse, and then compressed to a short duration.[3] The low-energy pulses have peak intensity below the gas ionization intensity threshold. As demonstrated in our previous work, DPNLC has the advantage of preserving the amount of spectral broadening, whereas the large-core fibers and large MPC modes reduce the amount of broadening obtained.[4]

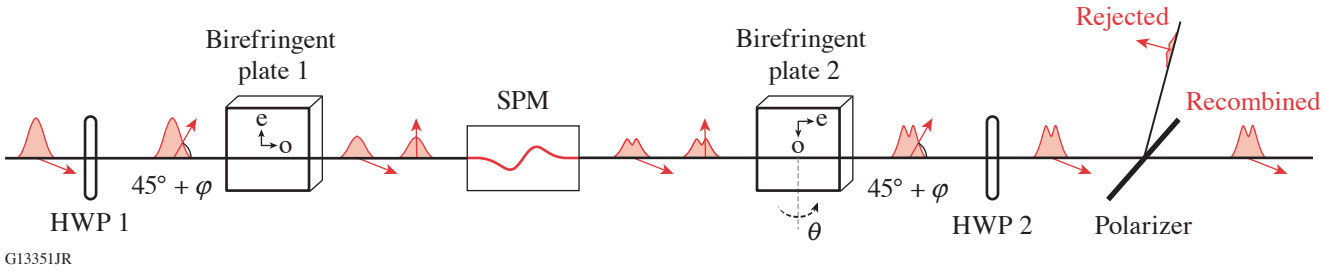

Figure 1
Apparatus for divided-pulse nonlinear compression analyzed in this summary. Birefringent plates with extraordinary axis "e" and ordinary axis "o" are used to divide one pulse into two low-energy, orthogonally polarized pulses. Red arrows indicate the pulse's polarization, and the distorted pulse shape after the SPM stage indicates an arbitrary reshaping by nonlinear processes in the SPM stage. The angles φ and θ represent angular errors in polarization and crystal AOI, respectively.

The alignment of the birefringent plates must be quite precise to divide and recombine the pulses with high efficiency. Previous authors have analyzed the precise alignment tolerances with computationally expensive numeric solutions of the nonlinear Schrödinger equation.[5,6] We have developed an analytic model that describes the output pulse from a DPNLC system that we expect to be a faster, more-flexible tool for tolerancing such systems. The most-sensitive alignment errors are errors φ in the incoming pulse polarization angle (equivalent to an error of φ in the birefringent plate axes) and errors θ in birefringent plate 2's angle of incidence (AOI) [which is modeled as a retardance $\Delta\phi(\theta)$]. We developed an analytic expression for the recombination efficiency of two-pulse DPNLC after accumulating Φ_{NL} nonlinear phase, which is shown in Eq. (1). The infinite sum can be simplified, as in Eq. (2), to quickly prescribe angular tolerances by using the $n = 0$ and the $n = 1$ terms and a small angle approximation for the retardance.

$$\eta = \frac{1}{2}\left\{1 + \sin^2(2\varphi) + \cos^2(2\varphi)\cos\left[\Delta\phi(\theta)\right]\sum_{n=0}^{\infty}\frac{(-1)^n\left[2\Phi_{\mathrm{NL}}\sin(2\varphi)\right]^{2n}}{(2n)!\sqrt{2n+1}} - \cos^2(2\varphi)\sin\left[\Delta\phi(\theta)\right]\right.$$

$$\left.\times\sum_{n=0}^{\infty}\frac{(-1)^n\left[2\Phi_{\mathrm{NL}}\sin(2\varphi)\right]^{2n+1}}{(2n+1)!\sqrt{2n+2}}\right\}. \tag{1}$$

$$\eta_{\mathrm{small}} = 1 - \frac{\cos^2(2\varphi)}{2}\left[\frac{2\Phi_{\mathrm{NL}}{}^2\sin^2(2\varphi)}{\sqrt{3}} + \frac{2\Phi_{\mathrm{NL}}\Delta\phi(\theta)\sin(2\varphi)}{\sqrt{2}} + \frac{\Delta\phi(\theta)^2}{2}\right]. \tag{2}$$

We have experimentally verified the validity of the model by measuring the recombination efficiency across angular errors with excellent agreement, as shown in Fig. 2. The figure plots the results of recombining our homebuilt 1.2-ps, 10-mJ pulses at a wavelength of 1030 nm after the accumulation of nonlinear phase in an HCF and division and recombination using 12-mm-thick, *x*-cut calcite plates. We should also note that a correction for amplified spontaneous emission (ASE) and pre-/postpulses is included in the plots in Fig. 2 because the ASE does not acquire significant nonlinear phase in the HCF and therefore has a different recombination efficiency.

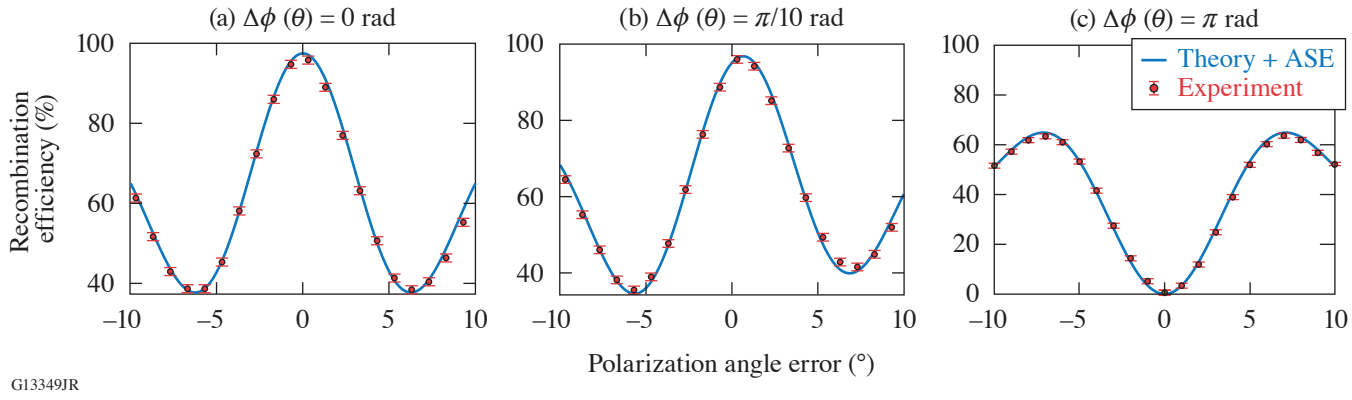

Figure 2
Experimental confirmation of angular tolerances model. The recombination efficiency is measured with errors in both the incoming polarization angle and AOI on plate 2 and is found to agree well with Eq. (1).

A useful consequence of the recombination efficiency expression is that the AOI can be used to compensate for polarization errors. The polarization angle tolerance becomes quite tight for large nonlinearity. For the 8.4-rad nonlinearity demonstrated in our lab and prescribing the angular tolerance to maintain >95% recombination efficiency, AOI compensation can loosen our angular tolerance from 1.0° to 2.8°, a tolerance that is easy to meet by hand.

This material is based upon work supported by the Department of Energy National Nuclear Security Administration under Award Number DE-NA0003856, the University of Rochester, and the New York State Energy Research and Development Authority.

1. G. Fan *et al.*, Opt. Lett. **46**, 896 (2021).
2. M. Kaumanns *et al.*, Opt. Lett. **46**, 929 (2021).
3. H. Jacqmin *et al.*, J. Opt. Soc. Am. B **32**, 1901 (2015).
4. G. W. Jenkins, C. Feng, and J. Bromage, Opt. Express **28**, 31,943 (2020).
5. F. Guichard *et al.*, IEEE J. Sel. Top. Quantum Electron. **20**, 619 (2014).
6. M. Kienel *et al.*, Opt. Express **21**, 29,031 (2013).

Eddy Killing from Global Satellite Observations

S. Rai,[1] M. Hecht,[2] M. Maltrud,[2] and H. Aluie[1,3]

[1]Department of Mechanical Engineering, University of Rochester
[2]Los Alamos National Laboratory
[3]Laboratory for Laser Energetics, University of Rochester

While wind is the primary driver of the oceanic general circulation, we find that it kills the ocean's most-energetic motions—its mesoscale eddies—at an average rate of 50 GW. We used satellite observations and a recent method to disentangle multiscale processes in spherical systems, including in an inertial confinement fusion implosion.[1] To our knowledge, a length-scale analysis of air–sea energy transfer on the entire globe had not been previously undertaken. In fact, we show that the temporal mean-eddy decomposition (i.e., Reynolds averaging) commonly used in oceanography fails to unravel eddy killing. Our results present the first evidence that eddy killing is a major seasonal sink for the oceanic eddies, peaking in winter. We find that eddy killing removes a substantial fraction (up to 90%) of the wind power input in western boundary currents such as the Gulf Stream and Kuroshio. This process, often overlooked in analyses and models, is a major dissipation pathway for mesoscales—the ocean's most-energetic scales.

At the surface of the ocean, wind deposits kinetic energy at the rate of $\tau \cdot u_o$, where τ is the wind stress at the surface of the ocean and u_o is the surface ocean velocity.[2] The power deposited in eddies, smaller than the size of l, is captured by Eq. (1). The overline represents the coarse-graining operation at length-scale l.

$$EP_l^{\mathrm{Cg}} = \overline{\tau \cdot u_o} - \overline{\tau} \cdot \overline{u_o}. \tag{1}$$

Equation (1) is analogous to the frequently used wind power input from Reynolds decomposition[3] as given in Eq. (2). The angled brackets represent temporal averaging and the primes represent deviation from temporal averaging.

$$EP^{\mathrm{Rey}} = \langle \tau \cdot u \rangle - \langle \tau \rangle \cdot \langle u_o \rangle = \langle \tau' \cdot u'_0 \rangle. \tag{2}$$

Studies using Reynolds decomposition, for example in Ref. 4, find that global power inputs to the eddies as measured from Eq. (2) are positive. Our work shows that eddy killing is an inherently spatial process and requires a spatial scale analysis to unravel it [Eq. (1)]. We find that wind power input is negative for length scales smaller than 260 km, implying eddy killing at those scales [see Fig. 1(b)]. Eddy killing is especially pronounced in Western Boundary Currents (WBC's) (e.g., the Gulf Stream and Kuroshio) and the Antarctic Circumpolar Current (ACC), while the remainder of the ocean has negligible eddy killing [see Fig. 1(a)]. Figure 1(c) reproduces the temporal analysis of previous studies and highlights the stark contrast with a spatial analysis, where we see a dominance of positive wind power input into the ocean, falsely suggesting a lack of eddy killing. This is contrasted by a dominance of negative values in Fig. 1(a).

This research was funded by U.S. NASA grant 80NSSC18K0772 and a grant from LANL's Center for Space and Earth Science. H. Aluie was also supported by U.S. Department of Energy grants DE-SC0014318, DE-SC0020229, and DE-SC0019329; NSF grant PHY-2020249; and U.S. Department of Energy National Nuclear Security Administration under Awards DE-NA0003856 and DE-NA0003914. Computing time was provided by NERSC under contract no. DE-AC02-05CH11231 and NASA's HEC Program through NCCS at Goddard Space Flight Center.

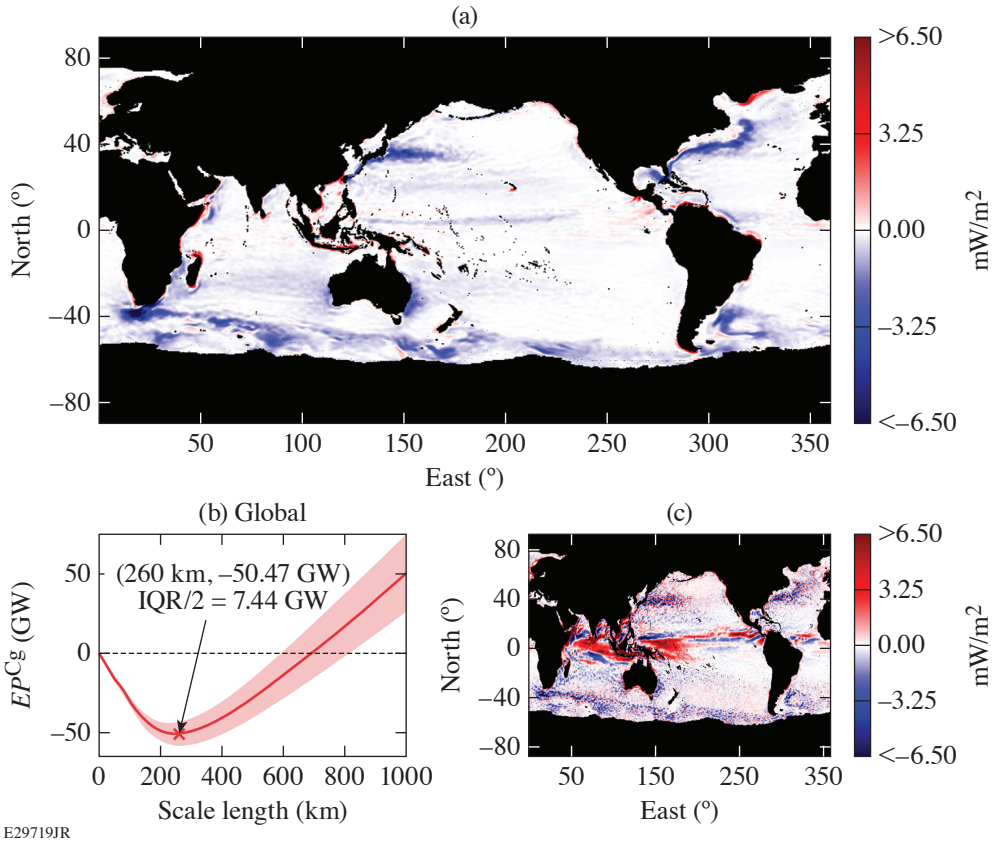

Figure 1

Direct measurement of eddy killing by coarse-graining satellite observations. (a) Wind power input (in mW/m^2) to the flow at scales <260 km using our measure EP^{Cg} in Eq. (1). We are able to clearly detect eddy killing (negative values) throughout the global ocean, especially in WBC's and the ACC. Areas in black include land and ocean regions with seasonal or permanent ice coverage. (b) Performing a scan over an entire range of length scales to unravel scales at which eddy killing operates globally, in addition to its magnitude. This is a key advantage of coarse graining. At any scale l, the plot shows wind power input to all scales smaller than l. By attaining a minimum at l = 260 km, it implies that eddies only at scales smaller than 260 km (but not larger) are losing energy to the wind, on average. The envelope shows interquartile range (IQR) (25th to 75th percentiles, Q1 to Q3) of temporal variation about the weekly climatology (as calculated from the seven years of data) of EP^{Cg}_l, and IQR/2 = (Q3 to Q1)/2. For reference, IQR/2 = 95.63 GW for the global $\tau \cdot u_o$ without any decomposition. (c) Reproducing eddy killing using the traditional Reynolds (or temporal) decomposition, EP^{Rey}, as in prior studies. It shows a stark contrast to our measure EP^{Cg}, with sporadic values of mixed sign without a clear indication of eddy killing. The two decompositions differ starkly in the tropics but agree near some land boundaries, where we expect winds to drive small-scale currents.

1. H. Aluie, GEM-International Journal on Geomathematics **10**, 9 (2019).
2. C. Xu, X. Zhai, and X.-D. Shang, Geophys. Res. Lett. **43**, 12,174 (2016).
3. L. Renault, J. C. McWilliams, and S. Masson, Sci. Rep. **7**, 17747 (2017).
4. C. W. Hughes and C. Wilson, J. Geophys. Res. Oceans **113** (2008).

The 12th Omega Laser Facility Users Group Workshop

J. A. Frenje,[1] S. Ali,[2] E. Merritt,[3] K. Falk,[4] S. Finnegan,[3] M. Gatu Johnson,[1] M. P. Valdivia,[5] L. Willingale,[6] and J. P. Knauer[7]

[1]Massachusetts Institute of Technology
[2]Lawrence Livermore National Laboratory
[3]Los Alamos National Laboratory
[4]Helmholtz-Zentrum Dresden-Rossendorf
[5]Johns Hopkins University
[6]University of Michigan
[7]Laboratory for Laser Energetics, University of Rochester

The 12th Omega Laser Facility Users Group (OLUG) Workshop was held virtually 27–30 April 2021. Over 200 researchers from 40 institutions in the U.S., China, France, Germany, Italy, Japan, Russia, and the UK registered for the meeting. This all-time attendance record for the OLUG Workshop was due to the absence of the on-site space limitations at LLE. The main goal of every OLUG Workshop is to facilitate a continuing dialog among OMEGA users; between the Users and LLE management; and between the Users and the broader scientific community. A major part of OLUG's responsibility is to also enhance the Omega Facility and its capabilities by defining a set of Findings and Recommendations (F&R's) each year. In addition, the workshop offers opportunities for students and young researchers to present their research in an interactive, yet informal, setting. This OLUG Workshop program included talks, posters, students and postdoc sessions, and a discussion of F&R's. In total, OLUG collectively submitted 29 F&R's to LLE management. The 13th OLUG Workshop will be held at LLE on 27–29 April 2022.

Introduction

The impact of the Omega Laser Facility on the fields of high-energy-density physics and inertial confinement fusion (ICF) is substantial in terms of both breadth and depth. Omega offers tremendous opportunities for programmatic and basic-science research through NNSA's National Laser User Facility (NLUF) and Laboratory Basic Science (LBS) programs. These programs play central roles in providing researchers with unique opportunities to conduct science in the areas of laboratory astrophysics, hydrodynamics and atomic physics, hydrodynamic instabilities and radiation hydrodynamics, materials physics and behavior of the equation-of-state under extreme conditions, relativistic laser–plasma interactions and magnetized plasmas, advanced/alternative inertial fusion concepts, nuclear physics, atomic physics and spectroscopy, and advanced diagnostics capabilities. Additionally, these programs play an important role in the student and postdoc training. The annual OLUG Workshop brings users together from all over the world, facilitating a vibrant dialog among them about their experiences running experiments through the NLUF and LBS Programs at the Omega Laser Facility. It also facilities a dialog between users and the LLE management focused on enhancing the Omega Facility and its capabilities, resulting in a set of well-defined F&R's each year, thus encouraging collaborations that could be undertaken.

The Workshop Program

The OLUG Program included the following invited science talks: "JASRI Experimental Platforms Using High-Power Optical Lasers at X-Ray Free Electron" (Toshinori Yabuuchi), "Overview of 2020 Royal Society Meeting to Update the EU/UK Roadmap for Inertial Fusion Energy" (Peter Norreys), "Findings from the Brightest Light Initiative Workshop" (Roger Falcone), "NNSA Internal 2020 Review of the Different ICF Approaches and Where We Are on the Road to Ignition" (Sean Regan), "Where's the Fusion? Overcoming Unexpected Challenges and the Road to Solutions for Ignition and Beyond" (Sean Finnegan), "Exploring Stellar Nucleosynthesis and Basic Nuclear Science Using High-Energy-Density Plasmas at OMEGA and the NIF" (Maria Gatu

U2752JR

Figure 1
A photo (computer screen shot) of some of the 2021 OLUG Workshop participants.

Johnson), and "Microphysics of Ultra-Dense Solids Common to Giant Planet Interiors and Macrophysics of Hot Plasmas Typical of Stellar Interiors" (Gilbert Collins). In addition, Ann Satsangi, Kramer Akli, and Slava Lukin presented National Nuclear Security Administration's, Office of Fusion Energy Sciences', and the National Science Foundation's perspectives on the role of the Omega Facility and Users in their programs. Other highlights included the talk "Commissioned MTW-OPAL Laser and Proposed 2 × 25 PW EP-OPAL Laser" by Jake Bromage (LLE); the facility talk "Omega Facility Update and Progress on OLUG Recommendations" by Sam Morse (LLE); and an update on NLUF/LBS/LaserNetUS activities by Mingsheng Wei (LLE). A student/postdoc panel discussion was led by Suzanne Ali (LLNL). A discussion of OLUG's Findings and Recommendations with LLE management was led by Liz Merritt (LANL) and Mario Manuel (GA). A roundtable discussion on "Careers in HED Science" was led by Suzanne Ali (LLNL). Student, postdoc, scientist, and facility posters totaling 50 poster presentations were organized in three poster sessions. Out of these posters, 37 of them were presented by graduate students, postdocs, and undergraduate students.

Nominations and Election

An election was held in 2020 but due to the COVID-19 pandemic, there was no election in 2021. A nominating committee was formed in November 2019 to request January nominations for the February 2020 election of four new OLUG Executive Committee (ExCom) members. Johan Frenje (Chair, MIT), Will Fox (PPPL), and Paul Keiter (LANL) formed the election committee. From a four-candidate ballot, Maria-Pia Valdivia (Johns Hopkins University) and Louise Willingale (University of Michigan) were elected as University representatives to replace Mark Koepke (West Virginia University) and Petros Tzeferacos (formerly University of Chicago); Alison Saunders (LLNL) was elected as national lab representative to replace Mario Manuel (GA); and Katerina Falk (HZDR, Dresden Rossendorf, Germany) was elected as the non-U.S. representative to replace Alexis Casner (CEA, France). For the May 2021–April 2022 period, the OLUG ExCom members are (a) four from U.S. university/small business: Johan Frenje (MIT, Chair), Maria-Pia Valdivia (Johns Hopkins, Vice Chair) Maria Gatu Johnson (MIT), and Louise Willingale (University of Michigan); (b) three from national laboratory/major business: Liz Merritt (LANL), Sean Finnegan (LANL), and Alison Saunders (LLNL); (c) one non-U.S. researcher: Katerina Falk (HZDR, Dresden Rossendorf, Germany); (d) one from the Junior Researcher list: Suzanne Ali (LLNL); and (e) LLE, ex-officio: Jim Knauer. The OLUG ExCom thanks Mark Koepke, Petros Tzeferacos, Mario Manuel, and Alexis Casner for their service and excellent work making OLUG such a vibrant community.

Summary of Findings and Recommendations

An important outcome of the annual workshop is the list of F&R's that OLUG submits to the LLE management. The 2021 F&R's are summarized below, categorized as Documentation (#1–#5), Calibration (#6–#9), Diagnostics (#10–#22), Target Capability (#23), Laser Systems (#24–#28), and Codes (#29). An update on the implementation of these F&R's will be presented by the LLE management at the OLUG satellite meeting on 9 November 2021 at the APS–DPP conference in Pittsburgh.

1. Ensure that users have access to detailed and up-to-date documentation on diagnostics.
2. Improve navigation on the diagnostic usage page (add links to the shot days for easier navigation to RID's with diagnostic setups).
3. Make OMEGA EP UV optics transmission measurements readily available to Users.
4. Improve Dante maintenance and documentation.
5. Make calibration data readily available on the PI portal.
6. Characterize gas-jet nozzles.
7. Characterize standard proton source on OMEGA EP.
8. Calibrate CPS1, CPS2, and MagSPEC with a Ra-221 source.
9. Bragg crystal inventory and characterization for streaked x-ray spectrometer.
10. Add a timing fiducial to Dante.
11. Fix SIM streak camera A (SSCA) UV timing fiducial.
12. Add an active shock breakout diagnostic (ASBO)/streak optical pyrometer on OMEGA EP TIM-14.
13. Add an optical Thomson scattering (OTS) diagnostic to OMEGA EP.
14. Provide more streak camera options for time-resolved x-ray spectroscopy.
15. Upgrade detector-finger holders for CPS1 and CPS2.
16. Time-resolved x-ray history measurements in high-neutron-yield environments.
17. Add the capability to infer directional flow vector on D_2-gas-filled or low-DT-yield implosions.
18. Add a third VISAR leg on ASBO on OMEGA EP and/or OMEGA.
19. Add photocathode options for PJX2 and PJX3.
20. Improve accuracy of SSCA data acquisition time.
21. Provide a new sector-magnet electron–positron–proton spectrometer for use in a wide-range of HEDS experiments on OMEGA/OMEGA EP.
22. Implement quick-look for CR-39–based proton radiography.
23. Add planar cryo on OMEGA EP.
24. Increase UV power on OMEGA EP.
25. OMEGA: Any beam, any delay (or at least a third leg).
26. Add opposing OMEGA EP beams.
27. Add smaller distributed phase plates on OMEGA EP.
28. Add smoothing by spectral dispersion on OMEGA EP.
29. Shared VisRad license.

This OLUG Workshop was made possible in part by the Laboratory for Laser Energetics at the University of Rochester for the use and availability of critical resources and support. In addition, OLUG thanks the LLE management for their exceptional responsiveness to our F&R's.

FY21 Q3 Laser Facility Report

J. Puth, M. Labuzeta, D. Canning, and R. T. Janezic

Laboratory for Laser Energetics, University of Rochester

During the third quarter of FY21, the Omega Facility conducted 296 target shots on OMEGA and 225 target shots on OMEGA EP for a total of 521 target shots (see Tables I and II). OMEGA averaged 10.0 target shots per operating day, averaging 87.2% Availability and 94.3% Experimental Effectiveness. OMEGA EP averaged 8.4 target shots per operating day, averaging 94.1% Availability and 92.6% Experimental Effectiveness.

Table I: OMEGA Laser System target shot summary for Q3 FY21.

Program	Laboratory	Planned Number of Target Shots	Actual Number of Target Shots
ICF	LLE	99	83
	LLNL	11	7
ICF Subtotal		110	90
HED	LLE	44	42
	LANL	11	13
	LLNL	38.5	46
	SNL	22	21
HED Subtotal		115.5	122
LBS	LLE	5.5	6
	LLNL	5.5	5
LBS Subtotal		11	11
AIBS		22	24
APL		11	10
CMAP		11	12
NLUF		22	21
Calibration	LLE	0	6
Grand Total		302.5	296

AIBS: Academic and Industrial Basic Science
APL: Applied Physics Labs (Johns Hopkins University)
CMAP: Center for Matter at Atomic Pressures
LBS: Laboratory Basic Science
NLUF: National Laser Users Facility

Table II: OMEGA EP Laser System target shot summary for Q3 FY21.

Program	Laboratory	Planned Number of Target Shots	Actual Number of Target Shots
ICF	LLE	28	24
	LLNL	21	21
ICF Subtotal		49	45
HED	LLE	35	50
	LANL	7	8
	LLNL	21	23
HED Subtotal		63	81
LBS	LLNL	14	14
LBS Subtotal		14	14
AIBS		7	9
CMAP		14	25
LaserNetUS		14	17
NLUF		7	10
Calibration	LLE	0	24
Grand Total		168	225

The OMEGA stage-F alignment sensor package upgrade project was completed on all 60 beams. This project provides higher resolution of alignment and spatial profile information for the alignment beam. With this system now in place, automated alignment algorithms are being developed for improved consistency. Additionally, the stage-C alignment sensor packages were augmented with appropriate filtration to take on shot measurements, improving system characterization.

The OMEGA de-ionized water-cooling system for the amplifiers has been augmented with a degassing system to reduce the oxidization of components and reduce the resulting contamination in the coolant flow. This is anticipated to reduce the amount of maintenance required on the amplifiers and may increase the transmission of flash-lamp light to the amplifier disks.

Publications and Conference Presentations

Publications

P. J. Adrian, J. Frenje, B. Aguirre, B. Bachmann, A. Birkel, M. Gatu Johnson, N. V. Kabadi, B. Lahmann, C. K. Li, O. M. Mannion, W. Martin, Z. L. Mohamed, S. P. Regan, H. G. Rinderknecht, B. Scheiner, M. J. Schmitt, F. H. Séguin, R. C. Shah, H. Sio, C. Sorce, G. D. Sutcliffe, and R. D. Petrasso, "An X-Ray Penumbral Imager for Measurements of Electron–Temperature Profiles in Inertial Confinement Fusion Implosions at OMEGA," Rev. Sci. Instrum. **92**, 043548 (2021).

C. D. Arrowsmith, N. Shukla, N. Charitonidis, R. Boni, H. Chen, T. Davenne, A. Dyson, D. H. Froula, J. T. Gudmundsson, B. T. Huffman, Y. Kadi, B. Reville, S. Richardson, S. Sarkar, J. L. Shaw, L. O. Silva, P. Simon, R. M. G. M Trines, R. Bingham, and G. Gregori, "Generating Ultradense Pair Beams Using 400 GeV/*c* Protons," Phys. Rev. Res. **3**, 023103 (2021).

S. Brygoo, P. Loubeyre, M. Millot, J. R. Rygg, P. M. Celliers, J. H. Eggert, R. Jeanloz, and G. W. Collins, "Evidence of Hydrogen–Helium Immiscibility at Jupiter-Interior Conditions," Nature **593**, 517 (2021).

C. Dorrer, M. Spilatro, S. Herman, T. Borger, and E. M. Hill, "Broadband Sum-Frequency Generation of Spectrally Incoherent Pulses," Opt. Express **29**, 16,135 (2021).

D. H. Edgell, A. M. Hansen, J. Katz, D. Turnbull, and D. H. Froula, "Unabsorbed Light Beamlets for Diagnosing Coronal Density Profiles and Absorption Nonuniformity in Direct-Drive Implosions on OMEGA," Rev. Sci. Instrum. **92**, 043525 (2021).

C. Goyon, M. R. Edwards, T. Chapman, L. Divol, N. Lemos, G. J. Williams, D. A. Mariscal, D. Turnbull, A. M. Hansen, and P. Michel, "Slow and Fast Light in Plasma Using Optical Wave Mixing," Phys. Rev. Lett. **126**, 205001 (2021).

D. Haberberger, A. Davies, J. L. Shaw, R. K. Follett, J. P. Palastro, and D. H. Froula, "Hot Raman Amplification," Phys. Plasmas **28**, 062311 (2021).

S. K. Han, R. F. Smith, D. Kim, J. K. Wicks, J. R. Rygg, A. Lazicki, J. H. Eggert, and T. S. Duffy, "Polymorphism of Gold Under Laser-Based Ramp Compression to 690 GPa," Phys. Rev. B **103**, 184109 (2021).

K. P. Hilleke, T. Ogitsu, S. Zhang, and E. Zurek, "Structural Motifs and Bonding in Two Families of Boron Structures Predicted at Megabar Pressures," Phys. Rev. Mater. **5**, 053605 (2021).

V. V. Ivanov, A. V. Maximov, R. Betti, L. S. Leal, J. D. Moody, K. J. Swanson, and N. A. Huerta, "Generation of Strong Magnetic Fields for Magnetized Plasma Experiments at the 1-MA Pulsed Power Machine," Matter Radiat. Extremes **6**, 046901 (2021).

T. M. Johnson, A. Birkel, H. E. Ramirez, G. D. Sutcliffe, P. J. Adrian, V. Yu. Glebov, H. Sio, M. Gatu Johnson, J. A. Frenje, R. D. Petrasso, and C. K. Li, "Yield Degradation Due to Laser Drive Asymmetry in D^3He Backlit Proton Radiography Experiments at OMEGA," Rev. Sci. Instrum. **92**, 043551 (2021).

R. G. Kraus, F. Coppari, D. E. Fratanduono, R. F. Smith, A. Lazicki, C. Wehrenberg, J. H. Eggert, J. R. Rygg, and G. W. Collins, "Melting of Tantalum at Multimegabar Pressures on the Nanosecond Timescale," Phys. Rev. Lett. **126**, 255701 (2021).

A. Kryjevski, T. Luu, and V. Karasiev, "Electronic Structure of Semiconductor Nanoparticles from Stochastic Evaluation of Imaginary-Time Path Integral," Phys. Rev. Res. **3**, 023173 (2021).

O. L. Landen, J. D. Lindl, S. W. Haan, D. T. Casey, P. M. Celliers, D. N. Fittinghoff, N. Gharibyan, V. N. Goncharov, G. P. Grim, E. P. Hartouni, O. A. Hurricane, B. J. MacGowan, S. A. MacLaren, K. D. Meaney, M. Millot, J. L. Milovich, P. K. Patel, H. S. Robey, P. T. Springer, P. L. Volegov, and M. J. Edwards, "Fuel Convergence Sensitivity in Indirect Drive Implosions," Phys. Plasmas **28**, 042705 (2021).

O. M. Mannion, I. V. Igumenshchev, K. S. Anderson, R. Betti, E. M. Campbell, D. Cao, C. J. Forrest, M. Gatu Johnson, V. Yu. Glebov, V. N. Goncharov, V. Gopalaswamy, S. T. Ivancic, D. W.

Jacobs-Perkins, A. Kalb, J. P. Knauer, J. Kwiatkowski, A. Lees, F. J. Marshall, M. Michalko, Z. L. Mohamed, D. Patel, H. G. Rinderknecht, R. C. Shah, C. Stoeckl, W. Theobald, K. M. Woo, and S. P. Regan, "Mitigation of Mode-One Asymmetry in Laser-Direct-Drive Inertial Confinement Fusion Implosions," Phys. Plasmas **28**, 042701 (2021) (invited).

A. L. Milder, J. Katz, R. Boni, J. P. Palastro, M. Sherlock, W. Rozmus, and D. H. Froula, "Measurements of Non-Maxwellian Electron Distribution Functions and Their Effect on Laser Heating," Phys. Rev. Lett, **127**, 015001 (2021).

Z. L. Mohamed, O. M. Mannion, J. P. Knauer, C. J. Forrest, V. Yu. Glebov, C. Stoeckl, and M. H. Romanofsky, "Application of an Energy-Dependent Instrument Response Function to Analysis of nTOF Data from Cryogenic DT Experiments," Rev. Sci. Instrum. **92**, 043546 (2021).

D. B. Schaeffer, W. Fox, M. J. Rosenberg, H.-S. Park, G. Fiksel, and D. Kalantar, "Measurements of Electron Temperature in High-Energy-Density Plasmas Using Gated X-Ray Pinhole Imaging," Rev. Sci. Instrum. **92**, 043524 (2021).

J. L. Shaw, M. A. Romo-Gonzalez, N. Lemos, P. M. King, G. Bruhaug, K. G. Miller, C. Dorrer, B. Kruschwitz, L. Waxer, G. J. Williams, M. V. Ambat, M. M. McKie, M. D. Sinclair, W. B. Mori, C. Joshi, H. Chen, J. P. Palastro, F. Albert, and D. H. Froula, "Microcoulomb (0.7±0.4/0.2 μC) Laser Plasma Accelerator on OMEGA EP," Sci. Rep. **11**, 7498 (2021).

G. Sutcliffe, P. Adrian, J. Pearcy, T. Johnson, N. Kabadi, S. Haque, C. Parker, B. Lahmann, J. Frenje, M. Gatu-Johnson, H. Sio, F. Séguin, B. Pollock, J. Moody, V. Glebov, R. Janezic, M. Koch, R. Petrasso, and C. Li, "A New Tri-Particle Backlighter for High-Energy-Density Plasmas," Rev. Sci. Instrum. **92**, 063524 (2021) (invited).

M. P. Valdivia, D. Stutman, C. Stoeckl, W. Theobald, G. W. Collins IV, V. Bouffetier, M. Vescovi, C. Mileham, I. A. Begishev, S. R. Klein, R. Melean, S. Muller, J. Zou, F. Veloso, A. Casner, F. N. Beg, and S. P. Regan, "Talbot-Lau X-Ray Deflectometer: Refraction-Based HEDP Imaging Diagnostic," Rev. Sci. Instrum. **92**, 065110 (2021).

W. Y. Wang and R. S. Craxton, "Pentagonal Prism Spherical Hohlraums for OMEGA," Phys. Plasmas **28**, 062703 (2021).

H. Wen, R. K. Follett, A. V. Maximov, D. H. Froula, F. S. Tsung, and J. P. Palastro, "Suppressing the Enhancement of Stimulated Raman Scattering in Inhomogeneous Plasmas by Tuning the Modulation Frequency of a Broadband Laser," Phys. Plasmas **28**, 042109 (2021).

K. M. Woo and R. Betti, "Impact of Areal-Density Asymmetries on the Loss of Confinement and Ignition Threshold in Inertial Confinement Fusion Capsules," Phys. Plasmas **28**, 054503 (2021).

S. Zhang, J. Li, C. M. Krauland, F. N. Beg, S. Muller, W. Theobald, J. Palastro, T. Filkins, D. Turnbull, D. Haberberger, C. Ren, R. Betti, C. Stoeckl, E. M. Campbell, J. Trela, D. Batani, R. H. H. Scott, and M. S. Wei, "Pump-Depletion Dynamics and Saturation of Stimulated Brillouin Scattering in Shock Ignition Relevant Experiments," Phys. Rev. E **103**, 063208 (2021).

Forthcoming Publications

X. Bian, J. K. Shang, E. G. Blackman, G. W. Collins, and H. Aluie, "Scaling of Turbulent Viscosity and Resistivity: Extracting a Scale-Dependent Turbulent Magnetic Prandtl Number," to be published in Astrophysical Journal Letters.

A. R. Christopherson, R. Betti, C. J. Forrest, J. Howard, W. Theobald, J. A. Delettrez, M. J. Rosenberg, A. A. Solodov, C. Stoeckl, D. Patel, V. Gopalaswamy, D. Cao, J. L. Peebles, D. H. Edgell, W. Seka, R. Epstein, M. S. Wei, M. Gatu Johnson, R. Simpson, S. P. Regan, and E. M. Campbell, "Direct Measurements of DT Fuel Preheat from Hot Electrons in Direct-Drive Inertial Confinement Fusion," to be published in Physical Review Letters.

L. E. Hansen, D. E. Fratanduono, S. Zhang, D. G. Hicks, T. Suer, Z. K. Sprowal, M. F. Huff, X. Gong, B. J. Henderson, D. N. Polsin, M. Zaghoo, S. X. Hu, J. R. Rygg, and G. W. Collins, "Melting of Magnesium Oxide up to Two Terapascals Using Double-Shock Compression," to be published in Physical Review B.

N. V. Kabadi, R. Simpson, P. J. Adrian, A. Bose, J. A. Frenje, M. Gatu Johnson, B. Lahmann, C. K. Li, C. E. Parker, F. H. Séguin, G. D. Sutcliffe, R. D. Petrasso, S. Atzeni, J. Eriksson, C. Forrest, S. Fess, V. Yu. Glebov, R. Janezic, O. M. Mannion, H. G. Rinderknecht, M. J. Rosenberg, C. Stoeckl, G. Kagan, M. Hoppe, R. Luo, M. Schoff, C. Shuldberg, H. W. Sio,

J. Sanchez, L. Berzak Hopkins, D. Schlossberg, K. Hahn, and C. Yeamans, "Thermal Decoupling of Deuterium and Tritium During the Inertial Confinement Fusion Shock-Convergence Phase," to be published in Physical Review E.

B. J. MacGowan, O. J. Landen, D. T. Casey, C. V. Young, D. A. Callahan, E. P. Hartouni, R. Hatarik, M. Hohenberger, T. Ma, D. Mariscal, A. Moore, R. Nora, H. G. Rinderknecht, D. Schlossberg, and B. M. Van Wonterghem, "Trending Low Mode Asymmetries in NIF Capsule Drive Using a Simple View-factor Metric," to be published in High Energy Density Physics.

J. L. Peebles, G. Fiksel, M. R. Edwards, J. von der Linden, L. Willingale, D. Mastrosimone, and H. Chen, "Magnetically Collimated Relativistic Charge-Neutral Electron-Positron Beams from High-Power Lasers," to be published in Physics of Plasmas.

A. Pineau, B. Chimier, S. X. Hu, and G. Duchateau, "Improved Modeling of the Solid-to-Plasma Transition of Polystyrene Ablator for Laser Direct-Drive Inertial Confinement Fusion Hydrocodes," to be published in Physical Review E.

S. Rai, M. Hecht, M. Maltrud, and H. Aluie, "Scale of Oceanic Eddy-Killing by Wind from Global Satellite Observations," to be published in Science Advances.

R. Sobolewski, "Optical Detectors and Sensors," to be published in the Handbook of Superconducting Materials.

Conference Presentations

J. L. Peebles, J. R. Davies, D. H. Barnak, M. J. Bonino, G. Brent, T. Cracium, and R. Betti, "Laser-Drive Coils, How Well Do They Work?" presented at the HEDS Seminar, virtual, 1 April 2021.

E. M. Campbell, "LLE: Today and Tomorrow," presented at the Institute of Optics Colloquium, virtual, 5 April 2021.

J. L. Shaw, G. Bruhaug, M. Freeman, F. Merrill, V. Geppert-Kleinrath, C. Wilde, and D. H. Froula, "Electron Radiography Based on Electron Beams from Self-Modulated Laser Wake-field Acceleration," presented at LANSCE Futures Spring 2021 Workshop Series, virtual, 6 April 2021.

The following presentations were made at the 4th International Symposium on High Power Laser Science and Engineering, virtual, 11–16 April 2021:

J. Bromage, S.-W. Bahk, M. Bedzyk, I. A. Begishev, S. Bucht, C. Dorrer, C. Feng, C. Jeon, C. Mileham, R. G. Roides, K. Shaughnessy, M. J. Shoup III, M. Spilatro, B. Webb, D. Weiner, and J. D. Zuegel, "MTW-OPAL: A Technology Development Platform for Ultra-Intense OPCPA Systems."

E. M. Campbell, "A Vision of the Future for High-Power Laser Research and Its Applications."

E. M. Campbell, "Laser Fusion: Present Status and the Path to Fusion Energy," presented at Cornell Energy Seminar, Cornell, NY, 15 April 2021.

S. P. Regan, "JASON Briefing," presented at JASON, virtual, 15 April 2021.

A. K. Schwemmlein, C. Stoeckl, W. T. Shmayda, C. J. Forrest, J. P. Knauer, S. P. Regan, and W. U. Schröder, "Generating a TNSA Trition Beam on OMEGA," presented at the APS April Meeting, virtual, 17–20 April 2021.

J. P. Palastro, D. H. Froula, M. Ambat, E. M. Campbell, R. K. Follett, P. Franke, V. N. Goncharov, D. Ramsey, J. L. Shaw, T. T. Simpson, D. Turnbull, K. Weichman, H. Wen, S. Jolly, F. Quéré, C. Benedetti, E. Esarey, C. Geddes, C. Schroeder, R. Bingham, S. Stoller, N. Vafaei-Najafabadi, G. Gregori, B. Malaca, A. Helm, J. Vieira, A. Di Piazza, A. Howard, A. Arefiev, T. M. Antonsen, Jr., and Z. Li, "Laser–Plasma Interactions Driven

by Spatiotemporally Structured Light Pulses," presented at the Bothe Colloquium, virtual, 21 April 2021.

The following presentations were made at the Omega Laser Facility Users Group 2021 Workshop, virtual, 27–30 April 2021:

J. Bromage, S.-W. Bahk, M. Bedzyk, I. A. Begishev, S. Bucht, C. Dorrer, C. Feng, B. N. Hoffman, C. Jeon, C. Mileham, J. B. Oliver, R. G. Roides, E. M. Schiesser, K. Shaughnessy, M. J. Shoup III, M. Spilatro, B. Webb, D. Weiner, J. D. Zuegel, D. H. Froula, J. L. Shaw, P. M. Nilson, H. G. Rinderknecht, L. J. Waxer, J. C. Puth, and E. M. Hill, "Commissioned MTW-OPAL Laser and Proposed 2 × 25 PW EP-OPAL Laser."

G. W. Collins, "Extreme Matters: Pressure to Explore New Worlds and Exotic Solids."

E. C. Hansen, A. C. Reyes, M. B. P. Adams, J. Carroll-Nellenback, J. R. Davies, K. Weide, D. Q. Lamb, and P. Tzeferacos, "Implicit Anisotropic Magnetic Resistivity in the *FLASH* Code."

P. V. Heuer, D. Stanczak, E. T. Everson, N. A. Murphy, and J. R. Davies, "Open Source High-Energy-Density–Physics Diagnostic Tools in PlasmaPy."

T. R. Joshi, R. C. Shah, W. Theobald, I. V. Igumenshchev, D. Cao, and S. P. Regan, "Observations of the Modulations Associated with the 60-Beam Overlap in X-Ray Self-Emission Images of Directly Driven Implosions."

Y. Lu, H. Li, K. Flippo, K. Kelso, A. Liao, S. Li, E. Liang, and P. Tzeferacos, "Monte Carlo Simulations for Proton Radiography in High-Energy-Density Plasma Experiments."

S. F. B. Morse, "Omega Facility OLUG 2021 Update: Progress on Recommendations and Items of General Interest."

S. P. Regan, "2020 Review of Inertial Confinement Fusion Approaches: The Research Path to Ignition."

A. Reyes and P. Tzeferacos, "High-Order Implicit-Explicit ADER-RK Methods for Hyperbollic Systems with Stiff Source Terms in the *FLASH* Code."

P. Tzeferacos, A. Reyes, E. C. Hansen, Y. Lu, D. Michta, M. P. A. Adams, C. J. Armstrong, K. Moczulski, and D. Q. Lamb, "The *FLASH* Code for Computational High-Energy-Density Physics-Recent Additions and Improvements."

M. S. Wei, "Omega Basic Science User Programs Update."

E. M. Campbell, "Laser Fusion: Present Status and the Path to Fusion Energy," presented at Cornell University, virtual, 5 May 2021.

P. Tzeferacos, "Extended MHD with *FLASH*: A Numerical Toolset for Magnetized Plasma Experiments," presented at the Center for Matter Under Extreme Conditions Seminar, virtual, 5 May 2021.

The following presentations were made at CLEO 2021, virtual, 9–14 May 2021:

S.-W. Bahk, I. A. Begishev, B. Webb, C. Jeon, R. G. Roides, C. Feng, M. Spilatro, R. Cuffney, C. Dorrer, C. Mileham, S. Bucht, and J. Bromage, "Effect of Pump Beam on the Amplified Signal Wavefront in DKDP Optical Parametric Amplification."

J. Bromage, S.-W. Bahk, M. Bedzyk, I. A. Begishev, S. Bucht, C. Dorrer, C. Feng, B. N. Hoffman, C. Jeon, C. Mileham, J. B. Oliver, R. G. Roides, E. M. Schiesser, K. Shaughnessy, M. J. Shoup III, M. Spilatro, B. Webb, D. Weiner, and J. D. Zuegel, "MTW-OPAL: A Technology Development Platform for Ultra-Intense All-OPCPA Systems."

C. Dorrer, I. A. Begishev, S.-W. Bahk, and J. Bromage, "Spatially Resolved Characterization of Partially Deuterated KDP Crystals for Parametric Amplification."

C. Dorrer, M. Spilatro, T. Borger, S. Herman, and E. M. Hill, "Broadband Sum-Frequency Generation in a Novel Angularly Dispersed Noncollinear Geometry."

C. Feng, C. Dorrer, C. Jeon, R. Roides, B. Webb, and J. Bromage, "Analysis of Pump-to-Signal Noise Transfer in Multi-Stage Optical Parametric Chirped-Pulse Amplification."

The following presentations were made at the ARPA-E Summit, virtual, 24–27 May 2021:

J. R. Davies, C. J. Forrest, V. Yu. Glebov, J. P. Knauer, and H. McClow, "The LLE Diagnostic Resource Team for Innovative Fusion Concepts."

P. Tzeferacos, R. Betti, J. R. Davies, F. Garcia-Rubio, E. C. Hansen, D. Michta, C. Ren, A. C. Reyes, W. Scullin, A. B. Sefkow, J. G. Shaw, H. Wen, and K. M. Woo, "A Simulation Source for Innovative Fusion Concepts in the BETHE Program."

P. Tzeferacos, A. Reyes, E. C. Hansen, Y. Lu, D. Michta, M. P. A. Adams, C. J. Armstrong, K. Moczulski, and D. Q. Lamb, "*FLASH*: A Simulation Code for HEDP and Innovative Fusion Concepts."

H. G. Rinderknecht, M. S. Wei, G. Bruhaug, K. Weichmann, J. P. Palastro, J. D. Zuegel, A. Arefiev, T. Wang, T. Toncian, A. Laso Garcia, D. Doria, K. Spohr, H. J. Quevedo, T. Ditmire, J. Williams, A. Haid, and D. Stutman, "Relativistically Transparent Magnetic Filaments as a Gamma-Ray Source for All-Optical Nuclear Photonics," presented at Nuclear Photonics 2021, virtual, 7–9 June 2021.

W. T. Shmayda, "Fundamentals of Tritium Handling," presented at TRANSAT Second Tritium School, virtual, 14–16 June 2021.

P. Heuer, "Charged-Particle Radiography with PlasmaPy," presented at the Summer Undergraduate Laboratory Internship Summer School, virtual, 14–25 June 2021.

E. M. Campbell, "Laboratory for Laser Energetics (LLE): Supporting OES Strategic Goals," presented at the OES Executive Meeting, virtual, 15–16 June 2021.

J. Bromage, S.-W. Bahk, M. Bedzyk, I. A. Begishev, S. Bucht, C. Dorrer, C. Feng, B. N. Hoffman, C. Jeon, C. Mileham, J. B. Oliver, R. G. Roides, E. M. Schiesser, K. Shaughnessy, M. J. Shoup III, M. Spilatro, B. Webb, D. Weiner, and J. D. Zuegel, "MTW-OPAL—A Technology Development Platform for Ultra-Intense OPCPA Systems," presented at EQEC, virtual, 20–24 June 2021.

The following presentations were made at the 47th European Physical Society Conference on Plasma Physics, virtual, 21–25 June 2021:

P. Franke, J. P. Palastro, D. Turnbull, D. Ramsey, T. T. Simpson, J. L. Shaw, M. V. Ambat, J. Katz, I. A. Begishev, R. Boni, J. Bromage, K. Daub, J. B. Oliver, C. Dorrer, D. H. Froula, S. Jolly, F. Quéré, C. Benedetti, E. Esarey, C. Geddes, C. Schroeder, R. Bingham, S. Stoller, N. Vafaei-Najafabadi, G. Gregori, B. Malaca, A. Helm, J. Vieira, A. Di Piazza, A. Howard, A. Arefiev, T. M. Antonsen, Jr., and Z. Li, "Spatiotemporal Control of Laser Pulses for Broadband Extreme Ultraviolet Generation."

A. M. Hansen, K. L. Nguyen, D. Turnbull, R. K. Follett, R. Huff, J. Katz, D. Mastrosimone, A. L. Milder, J. P. Palastro, D. H. Froula, B. Albright, and L. Yin, "Cross-Beam Energy Transfer Saturation."

E. M. Campbell, "Laboratory for Laser Energetics (LLE): Today and Tomorrow," presented at the Pulsed-Power Sciences Center, virtual, 23 June 2021.

P. Heuer, "Charged-Particle Radiography with PlasmaPy," presented at Plasma Hack Week, virtual, 28 June–2 July 2021.


1850
MELIORA
UNIVERSITY of
ROCHESTER